MAGNETIC THERMAL HYSTERESIS IN DY, GD AND GD/DY/GD NANOLAYERS

AND EXPERIMENTAL DETERMINATION OF THERMODYNAMIC

PROPERTIES OF THIN FILM SYSTEMS

by

AJANI LUISTER WALDEN ROSS

Presented to the Faculty of the Graduate School of

The University of Texas at Arlington in Partial Fulfillment

of the Requirements

for the Degree of

DOCTOR OF PHILOSOPHY

THE UNIVERSITY OF TEXAS AT ARLINGTON

December 2012

ACKNOWLEDGMENTS

As with most endeavors in life no one can claim a great accomplishment without the help and support of others. Because of this I would like to express my extreme gratitude and thanks to all who have had some help in all of my successes that have lead up to this work. First I would like to thank all of the physics office staff, who helped me in the planning of my graduate career and who in a large part are responsible for the ease of its completion. Next I would like to thank my research advisor Dr. Ali Koymen, whose guidance and support made this research project a success above and beyond what I originally expected. Lastly and with the most extreme pride I would like to thank all the members of my family. Without their support I would have never had put in the time or the effort into reaching this stage in my academic career. And to my parents and sister a simple thank you would not express the gratitude I have for the time and money spent in helping me achieve this goal I dedicate this to you as a small step in repayment.

ABSTRACT

MAGNETIC THERMAL HYSTERESIS IN DY, GD AND GD/DY/GD NANOLAYERS

AND EXPERIMENTAL DETERMINATION OF THERMODYNAMIC

PROPERTIES OF THIN FILM SYSTEMS

Ajani L. W. Ross, PhD.

The University of Texas at Arlington, 2012

Supervising Professor: Ali R. Koymen

Magnetic thermal hysteresis (MTH) is observed when the temperature dependent magnetic properties of a material are reliant on the starting point of the measurement. MTH was observed in thin film Dy samples at low values of constant external magnetic field strengths using a Superconducting Quantum Interference Device (SQUID magnetometer). The temperature is changed from 20K to 300K back to 20K under a constant field. In these temperature sweeps differences in magnetic moment were observed near the low end of the temperature range starting around 150K. However, when starting at the high end of the temperature scale and making the same measurements this separation is not

observed. The large difference in moment at low temperature can also be controlled by the magnitude of the external field strength. In the Dy films the existence of Alternate Helicity (AH-state) a shifting of the easy magnetization axis and a Helical (H-state) are the primary causes for the existence of the observed MTH [9]. In Gd helical magnetization states do not exist but to a small extent the Gd films also show thermal hysteresis, over a smaller temperature range. Measurements of three layer systems which consist of a Dy film between two Gd films showed noticeable differences in the forward and return paths of the moment vs. temperature M(T) graphs consistent with the effects seen in the individual films. The effects of the individual films are easily distinguished in the three layer system. This cumulative effect can be controlled by modifying the layer thickness and therefore changing the shape and size of the observed magnetic thermal hysteresis. In addition to this a series of measurements was done to find a simplified means for calculating otherwise difficult thermodynamic properties of a system such heat capacity and entropy. A dataset consisting of multiple field hysteresis M(H) loops was made and by using the well known Maxwell relationships, for a magnetic system, the necessary calculations are done to find these otherwise intricate functions.

TABLE OF CONTENTS

LIST OF ILLUSTRATIONS

CHAPTER 1

INTRODUCTION

Magnetism of materials

Magnetic properties of materials are dependent on the properties of individual atoms or on their collective response to the presence of an external magnetic field (H) [52, 59, 62]. The ordering of electrons (electronic configuration) in the atomic orbitals of the atoms determines this magnetic behavior [52]. The observed magnetic behavior, as a function of temperature or magnetic field, can be classified as either: Paramagnetic, Diamagnetic, Ferromagnetic, Anti-ferromagnetic, or Ferrimagnetic.

Magnetic Susceptibility

For a linear material the magnetization ($\vec{M} = \chi_m \vec{H}$); χ_m is the magnetic susceptibility and is independent of the external magnetic field [81]. For magnetic materials it represents the responsiveness of the material to an applied external magnetic field. In Paramagnetic materials $\chi_m > 0$ in Diamagnetic materials $\chi_m < 0$. Similarly in these types of materials the susceptibility is

roughly constant over a range of magnetic field values. However in Ferromagnetic materials the magnetic behavior is usually much more complex and χ_m is not simply a constant of proportionality but a function of the applied field ($\chi_m = \chi_m(H)$). The treatment of the magnetic susceptibility for Ferromagnetic substances is available in Appendix D.

Paramagnetism

"Para" meaning with or along, paramagnetic materials have an overall net angular momentum due to unpaired electrons; this results in small positive values of the magnetic susceptibility (χ_m). This positive susceptibility leads to an increasing linear relationship of M or (B) with respect to a positive applied field. With a positive value of the susceptibility the magnetic moments of the material follow the direction of the external field (Fig 1.1).
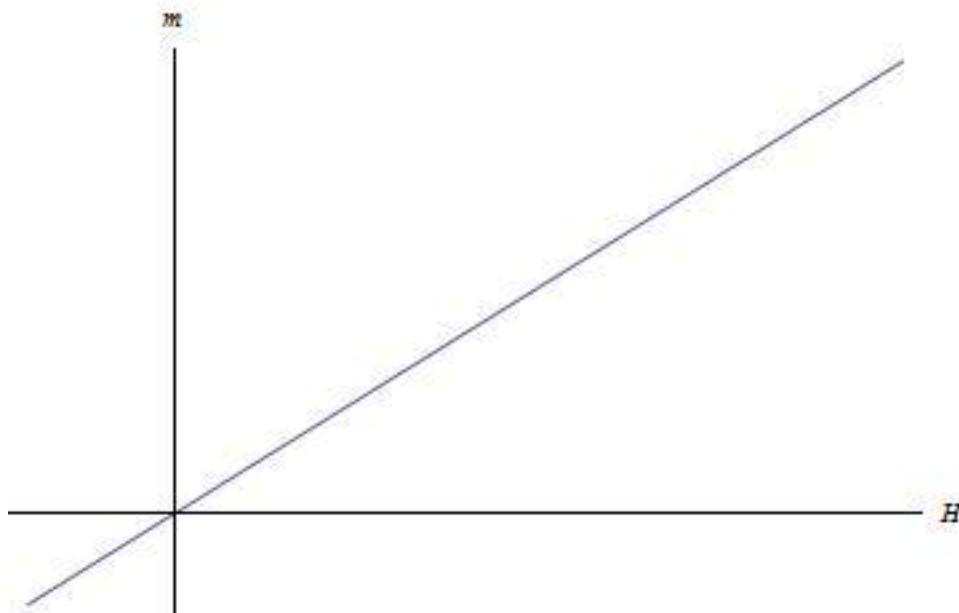
Fig. 1.1 Magnetic moment response for a Paramagnet in an increasing external field H.
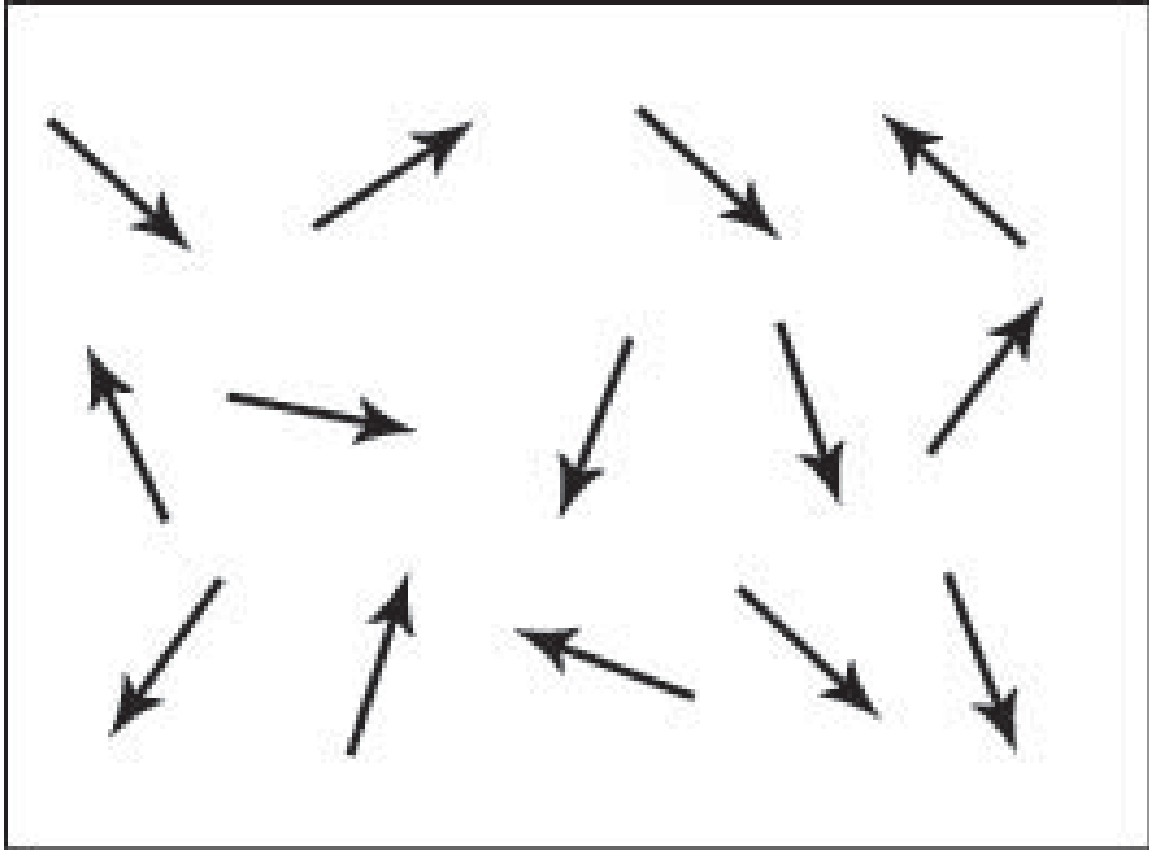
Fig. 1.2 Random arrangements of magnetic spins in the absence of a
magnetic field H resulting in a net moment of zero.

The external magnetic field induces a magnetization which aligns parallel with the

applied external magnetic field that causes it. The behavior of this type of magnetic system is

attributed (observed) for atoms in which have a net magnet moment due to the unpaired electrons

from partially filled orbitals (sub shells). Therefore the alignment of these atomic moments with

the external field results in a net positive magnetization. However, when the field is removed the magnetization falls to zero because there is no cooperative interaction between the magnetic moments (Fig 1.2) [53, 81].

Magnetic moments in an applied field

In the simplest model of a magnetic system one can imagine a single electron in the presence of an external magnetic field $\vec{B}\ or\ \vec{H}$ ($\vec{H} = \frac{\vec{B}}{\mu_0}\ in\ vacuum$). An electron in this field has an energy (E_m) given by

$$E_m = g\mu_B B m_s$$

where, $g \approx 2$, is the "g-factor", μ_B is the Bohr-magneton and m_s is the component of the spin quantum number 's = 1/2' for a single electron. With this we can calculate the statistical behavior of a collection of N number of electrons in a magnetic field [55, 57].

If the electrons are not free but bound to an atom (nucleus) then in addition to their spin angular momentum they also posses angular momentum $\vec{L}$. This comes from the electrons motion about the nucleus of the atom.

$$\hbar\vec{L} = \sum_i \vec{r}_i \times \vec{p}_i$$

The magnetic moment of an atom in this case is associated with its total angular momentum vector $\vec{J}$; in units of $\hbar$.

$$\vec{J} = \vec{L} + \vec{S}$$

In a classical sense of electronic spins there is no quantization of the magnetic energy values i.e. the magnetic energy spectrum is continuous in the classical sense. This therefore means that the spins of the particles are not constrained to half integer values but can have any value between spin up and spin down where the spin direction is in relation to the magnetic field. The energy, of a single particle, can thus be written as a continuous function with respect to the angle theta.

$$E_m = -\mu B Cos\theta$$

where μ is the magnetic moment of the particle.

The average moment along the magnetic field $\vec{B}$ would be found by evaluating:

$$\langle \mu_z \rangle = \frac{\int_0^\pi \mu\, Cos\theta\, e^{\frac{\mu B Cos\theta}{k_B T}}\, Sin\theta\, d\theta}{\int_0^\pi e^{\frac{\mu B Cos\theta}{k_B T}}\, Sin\theta\, d\theta}$$

The solution gives:

$$\langle \mu_z \rangle = \mu \left[Coth(x) - \frac{1}{x} \right] \equiv \mu L(x)$$

$$x = \frac{\mu B}{k_B T}$$

The function L(x) is defined as the Langevin function after its founder Paul Langevin. As it is well known many of the ideas of magnetism cannot be described by classical means but as we will see later the previous derivation is a special case of the quantum mechanical derivations of magnetism and is in good agreement with experiment.

If we look at the same system only from the standpoint of Quantum Mechanics, a single particle has discrete "quantized" values for its energy. The particle in this field can only have one of two states spin up or spin down. This in turn creates a quantized energy spectrum:

$$E_m = \mu B \text{ or } E_m = -\mu B$$

The average moment of this system should be (using Boltzmann statistics)

$$\langle \mu_z \rangle = \frac{\mu\, e^{\frac{\mu B}{k_B T}} - \mu\, e^{\frac{-\mu B}{k_B T}}}{e^{\frac{\mu B}{k_B T}} + e^{\frac{-\mu B}{k_B T}}}$$

$$\langle \mu_z \rangle = \mu Tanh\left(\frac{\mu B}{k_B T}\right)$$

This represents the solution of the average magnetic moment of a single (spin ½) particle in the presence of a magnetic field. If we assume no interaction between these spins, then for a collection of N like particles we should expect that the net moment or magnetization can be found.

$$M = n\langle \mu_z \rangle = n\mu Tanh\left(\frac{\mu B}{k_B T}\right) = M_s Tanh\left(\frac{\mu B}{k_B T}\right)$$

The saturation magnetization 'M$_s$' is the largest attainable value for the magnetization of the sample where n is the number of spins per volume V.

(n = N/V)

The above equation can be graphed directly as a function of $\left(\dfrac{\mu B}{k_B T}\right)$ to show how this magnetic system would look in the presence of a changing magnetic field. This is essentially a simplified representation for some of the systems that will be discussed in later chapters. Other useful information can be gathered from this derivation such as the susceptibility and the moment vs. temperature expression. A plot of both the 'classical' and 'quantum mechanical' solutions to the above analysis show similar results (Fig. 1.3).
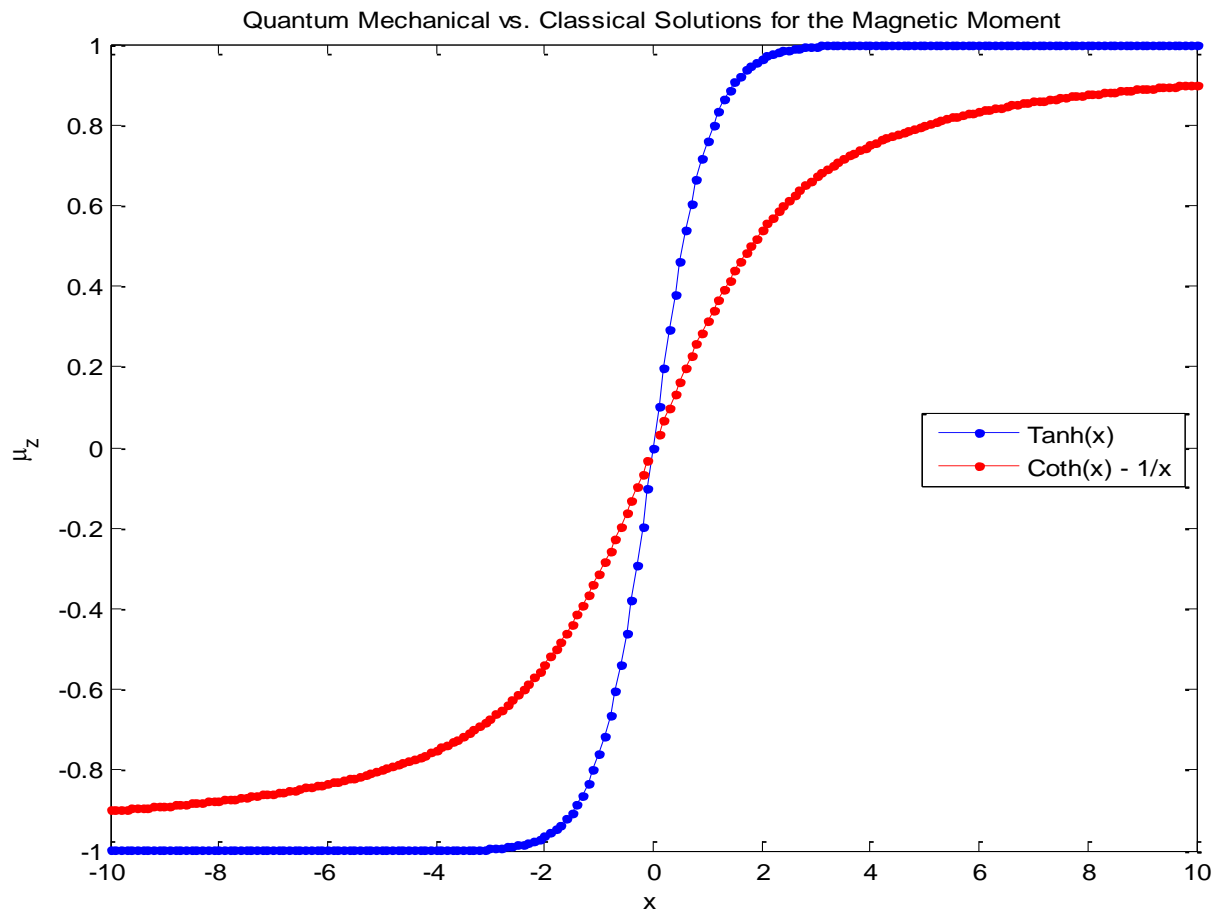
Fig. 1.3 Comparison of the Classical solution L(x) and the Quantum Mechanical
solution Tanh(x) for a system of N non-interacting spins s = 1/2.

Diamagnetism

    Diamagnetism is a property of all materials although the effect is usually very weak [84,

85]. In diamagnetic materials the magnetic susceptibility is negative resulting in an overall

reduction in the induction field (B) due to the moments of these atoms aligning anti-parallel to

the field (Fig 1.4).
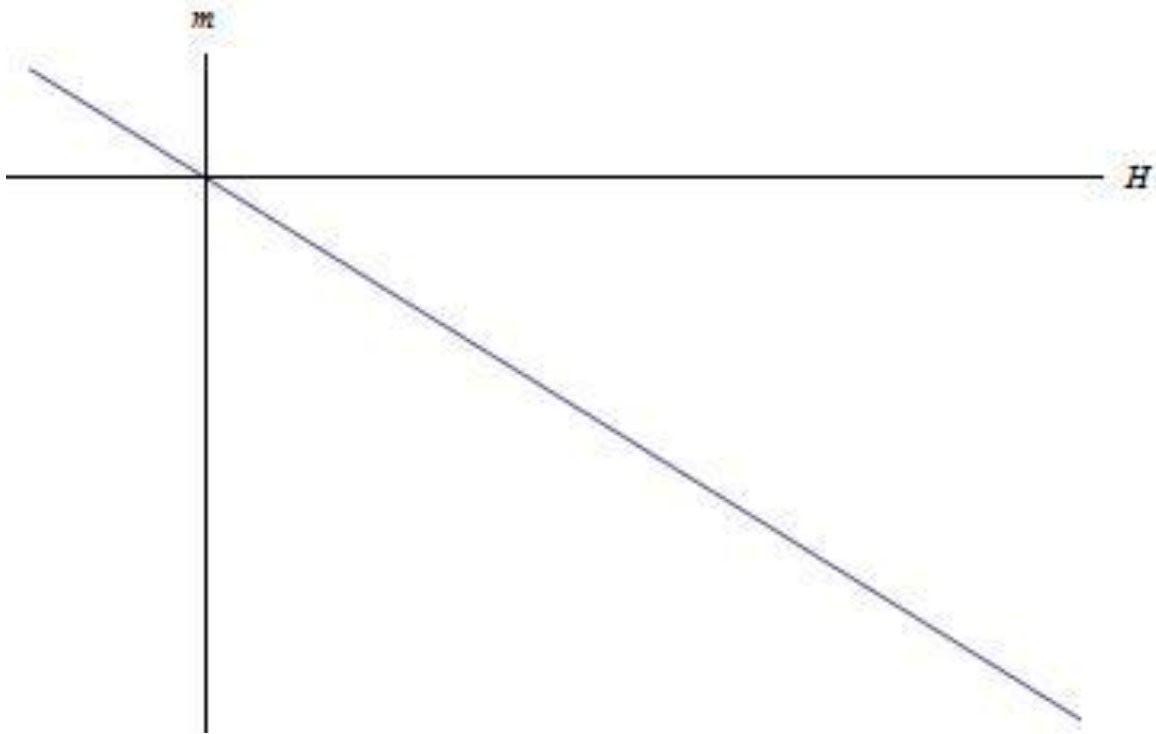
Fig. 1.4 Magnetic moment response for a Diamagnet in an increasing external field H.

Magnetic Domains

In Ferromagnetic and Ferrimagnetic materials it is evident that a non-zero magnetization is present when the external field is reduced to zero from a larger (saturation) field. The explanation of this effect is done on a small scale. With the existence of domains, defects and other processes constitute those changes that cause the necessary paradigm shifts from which this spontaneous magnetization arises[81, 86].

Magnetic domains consist of small regions in a material in which the magnetic moments all lie in a parallel direction giving a uniform magnetization in the respective region. The separations of each of the subsequent regions of uniformity in field are called the domain walls. However, with no external field applied the net sum of all magnetic domains is effectively zero giving no effect to the overall magnetization of the sample.

In a demagnetized Ferro/Ferrimagnet, from the conceptual picture of domains, we would observe the vector sum of all domains to be zero (Fig. 1.5a). As the strength of the external field is increased from zero to the saturation value those domains with magnetization in the direction will increase in size, due to the wall motion (Fig. 1.5b, c). As the field is increased further this increase in size of the favored domains will continue until saturation. At this point the direction of the total magnetization of the sample is parallel to the external field direction, and the sample is saturated (Fig 1.5d). Returning to zero from the saturation field the process is essentially reversed. However, due to anisotropic properties of some materials there is an inherent irreversibility and the path in reverse is not traversed along the same path. This irreversibility is the determining factor in the coercivity and remnant magnetization features seen in the field hysteresis graph.
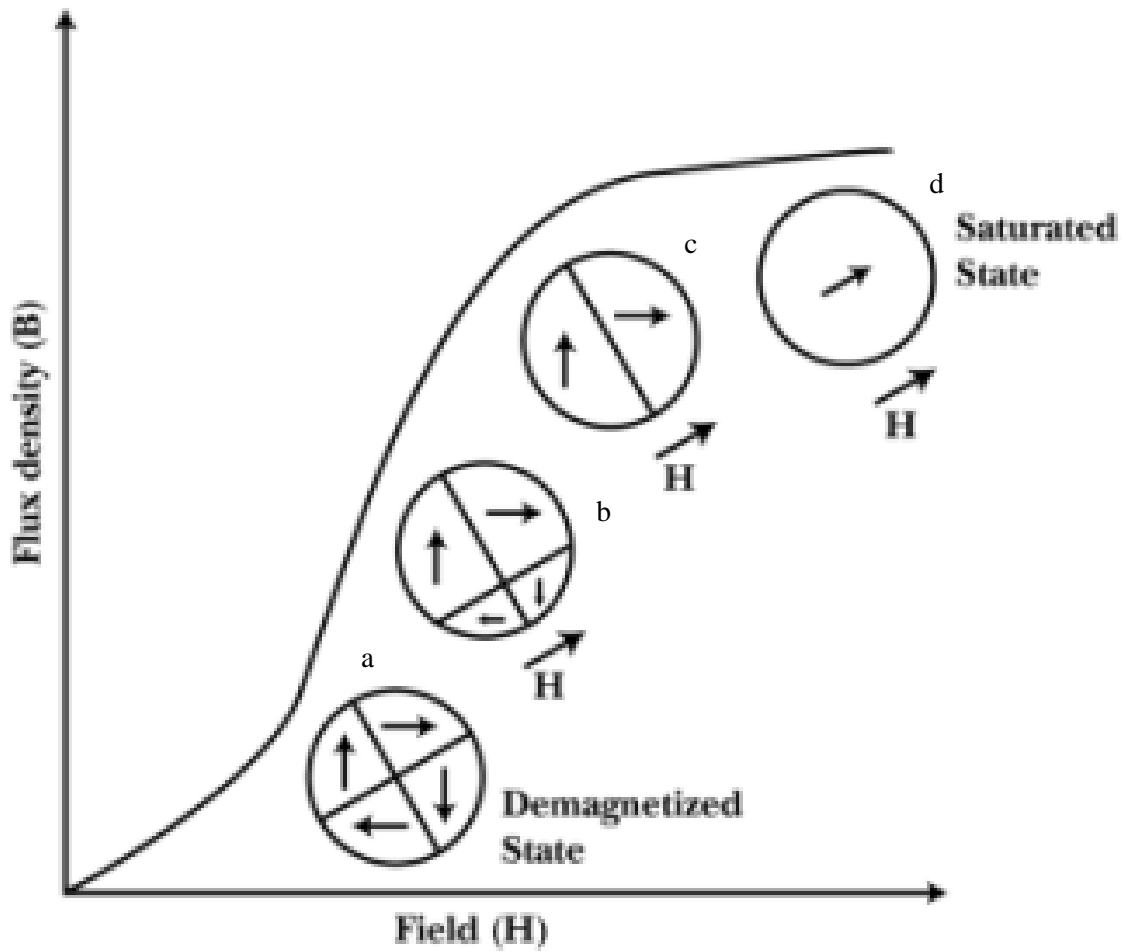
Fig. 1.5 Domain wall representation of magnetizing a Ferromagnet from a demagnetized state. The strength of the external field causes the size of these domains to increase (rotating the moments towards the field direction until saturation).

Ferromagnetism

In some materials (usually metals) the configuration of the electronic order leads to a spontaneous ordering of the magnetic spins below a specific temperature. This spontaneous ordering allows for a net magnetization even in the absence of an external magnetic field (Fig. 1.6). In Ferromagnetic materials this spontaneous ordering is contained in small regions (magnetic domains) [81, 84-86]. Each domain has its own net magnetization in one particular direction. The magnetization of each domain is a cumulative effect from the spins of the particles in that particular domain.
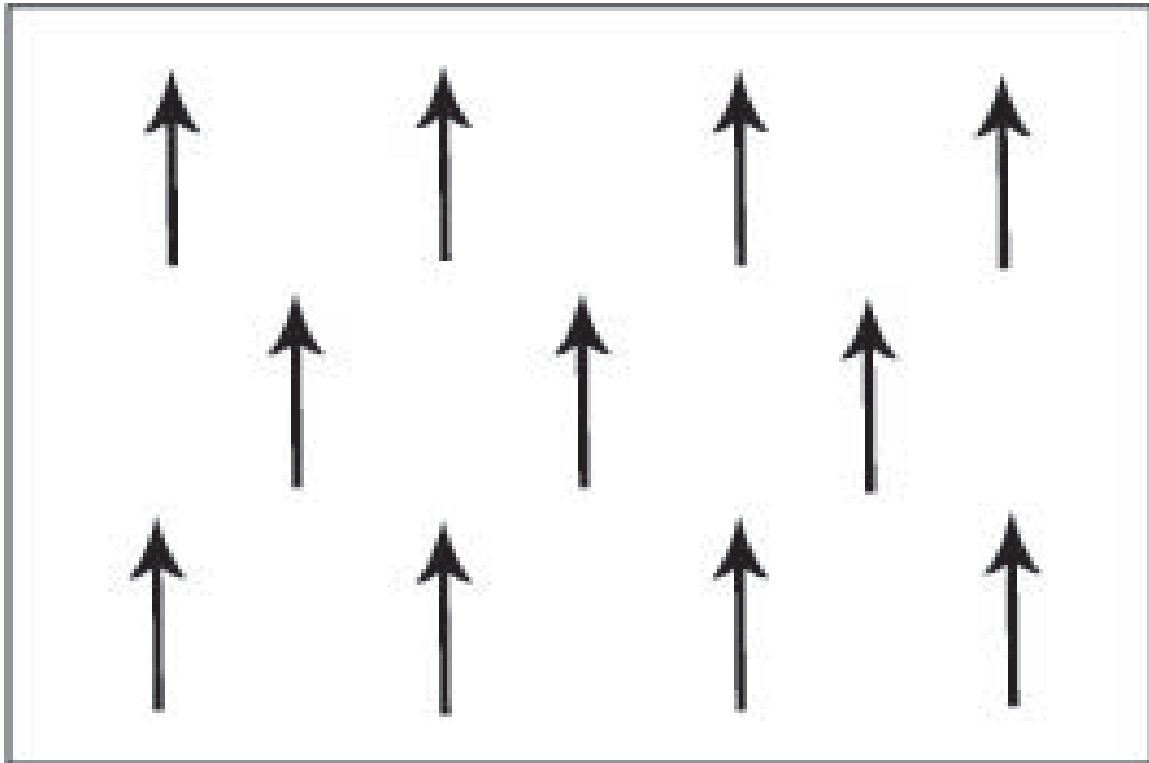
Fig. 1.6 Ordering of the magnetic moments for a saturated Ferromagnet. This arrangement remains even after H = 0 resulting in the remnant magnetic moment characteristic of Ferromagnetic materials.

A Ferromagnet in an external magnetic field; the Hamiltonian of the system can be described by [55]:

$$\widehat{H} = -\sum_{ij} J_{ij}\, \vec{S}_i \cdot \vec{S}_j + g\mu_B \sum_{j} \vec{S}_j \cdot \vec{B}$$

The first term represents the interaction of nearest neighbor spin – spin coupling where J is the exchange interaction between this coupling term, S is the spin operator of the respective

particle. The second term represents each particles interaction with the magnetic field B where g and μ_B have been described previously.

Solving this Hamiltonian at various temperatures, magnetic fields and magnetic systems (J_{ij}, S) gives properties of the system such as the magnetization as a function of temperature or external field; M(T) and M(H) measurements. Different methods are available to solve a Hamiltonian like this to try and approximate experimental measurements [53]. The main method for solving this type of problem is done by computer simulation methods or calculations [24, 53] (Appendix). However, other well known functions that currently exist can be used, with good agreement, to model Ferromagnetic systems. One such function, that is a general case of the paramagnetic system discussed above, can be modified to reproduce accurate representations of Ferromagnetic systems; this function is known as the Brillouin function [82].

$$B_J(x) = \frac{2J+1}{2J} Coth\left(\frac{2J+1}{2J}x\right) - \frac{1}{2J} Coth\left(\frac{x}{2J}\right)$$

where:

$$x = \frac{g\mu_B J B}{k_B T}$$

In later chapters we will see how this function can be modified to closely model Ferromagnetic behavior. However, this solution is derived for a system in which the only consideration was the interaction of a particle, with a particular value of the vector$\vec{J}$, with the external magnetic field (Appendix). It does not contain information regarding exchange energies, spin-spin coupling (1st

term in Hamiltonian) or spin-orbit coupling. Nevertheless for "nice" Ferromagnetic systems the modified Brillouin function is in good agreement.

AntiFerromagnetism

Antiferromagnetic materials exhibit special behavior in an applied magnetic field depending upon the temperature. At very low temperatures, the solid exhibits no response to the external field, because of the antiparallel ordering of the atomic layers is rigidly maintained (Figure). At higher temperatures, some atoms break free of the orderly arrangement and align with the external field. This alignment and the weak magnetism it produces in the solid reach their peak at the Néel temperature. Above this temperature, thermal agitation progressively prevents alignment of the atoms with the magnetic field, so that the weak magnetism produced in the solid by the alignment of its atoms continuously decreases as temperature is increased (Fig 1.7) [55, 59, 62].
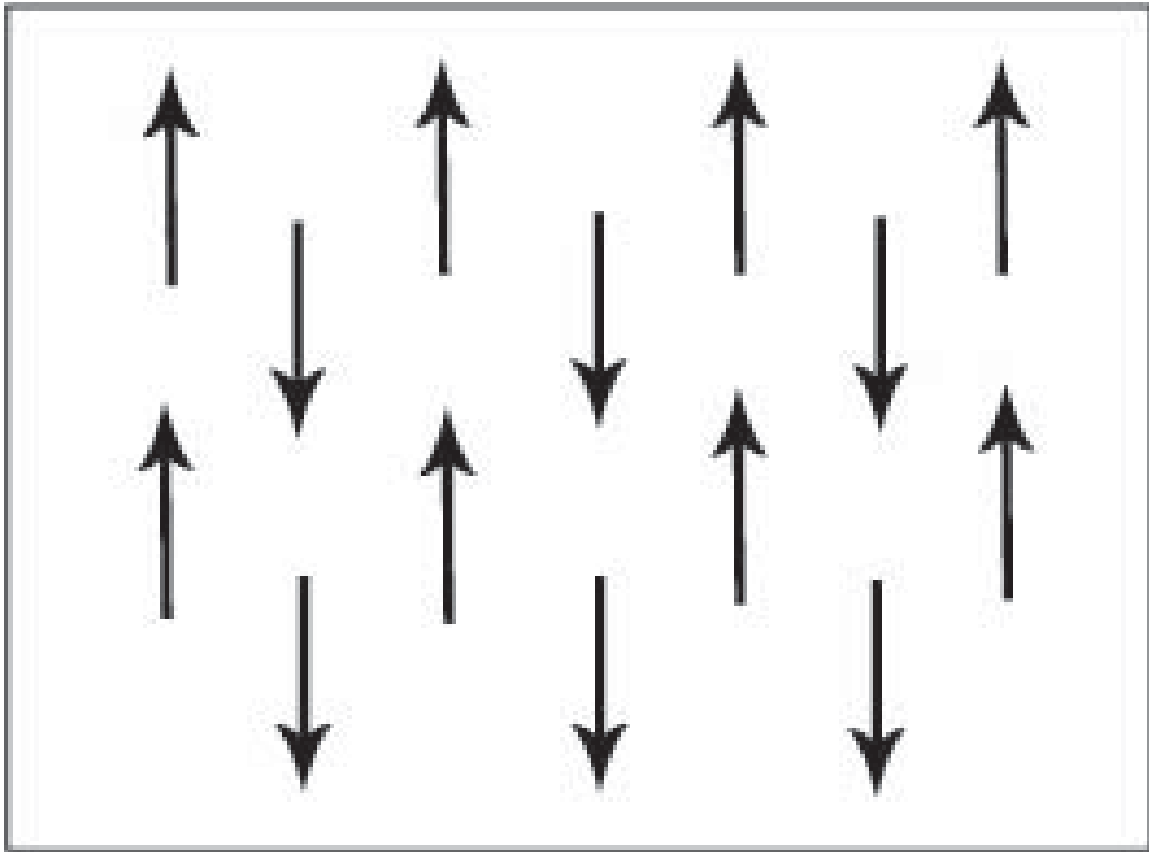
Fig. 1.7 Antiparallel spin arrangement in a AntiFerromagnet

Helical Magnetism

    In some Rare Earth (RE) elements the crystal structure is such that the atomic layers contain the magnetic properties of the material (Fig. 1.8) Dysprosium is an example of this.
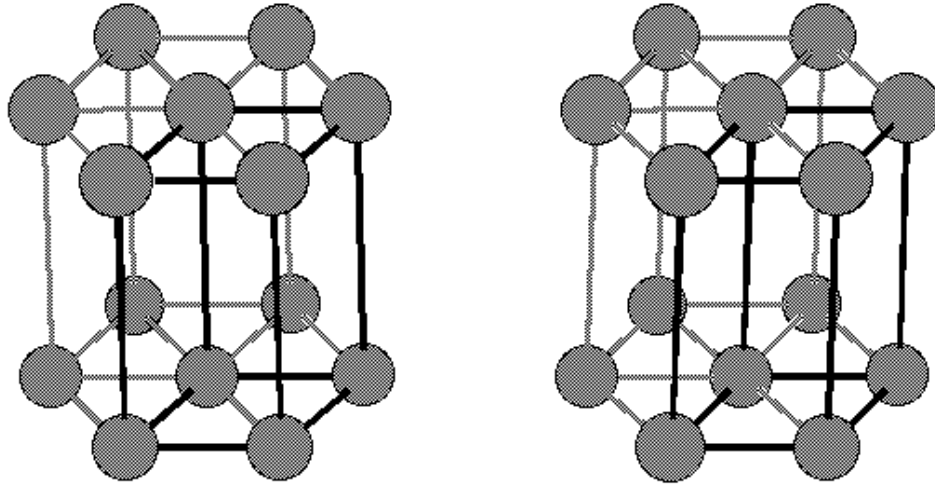
Fig. 1.8 Example structure of a hexagonal arrangement of atoms.

In the layers the atoms align in a Ferromagnetic order (at low temperature). However, between the layers the alignment of the magnetic moments can be described by nearest – neighbor interactions and next nearest - neighbor interactions and so on. Taking the angle between the magnetic moments in these layers as θ we can describe the energy of the system as [54, 62]:

$$E = -2NS^2(J_1 Cos\theta + J_2 Cos2\theta)$$

This energy depends on the number of atoms (N) in each plane and the exchange constants J_1 and J_2. More exchange interactions can be considered but the magnetic interaction between the layers decreases rapidly and further terms are not needed. Minimizing the energy relationship yields the angular dependence of these exchange constants and gives the angular regions where the Helical structure occurs.

$$(J_1 + 4J_2\text{Cos}\theta)\text{Sin}\theta = 0$$

This equation is satisfied for $\Theta = 0$ or π which implies that the layers are arranged in a Ferromagnetic order ($\Theta = 0$) or AntiFerromagnetism ($\Theta = \pi$). The third solution occurs for:

$$\text{Cos}\theta = -\frac{J_1}{4J_2}$$

This solution corresponds to the Helical order known as Helimagnetism (Fig. 1.9) we will investigate this type of magnetism for some of the samples used in these experiments.
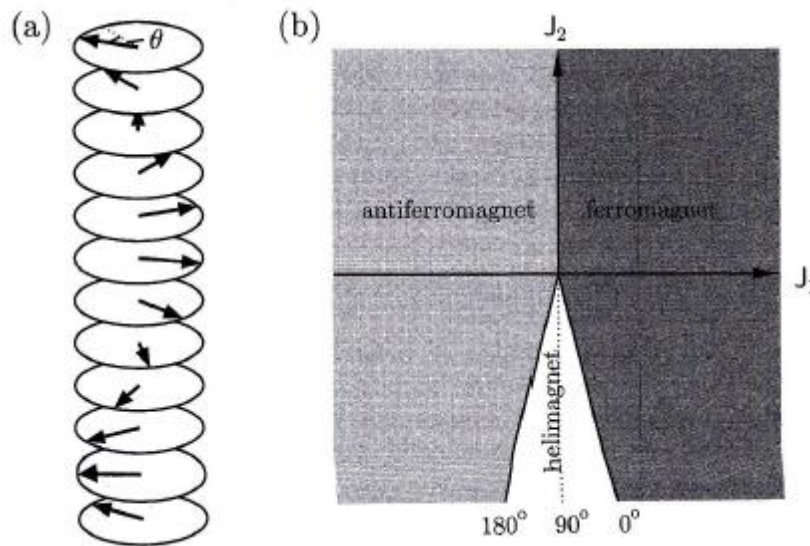
Fig. 1.9 Helical ordering of magnetic spins per layer for a heli-magnetic system. a) Each circle represents an atomic layer. b.) Relationship between J_1 and J_2 which leads to different observed types of magnetism [62]

Superconductivity

In certain materials when cooled, below a certain sufficiently low temperature, the electrical resistivity of the material drops quickly to zero. At this temperature the material undergoes a phase transition to a superconducting state, this temperature is known as the critical temperature T_c.

When a superconductive material is placed in a region of magnetic field and cooled through T_c the magnetic flux through the material suddenly drops to zero, this is known as the Meissner Effect (Fig. 1.10) [56].
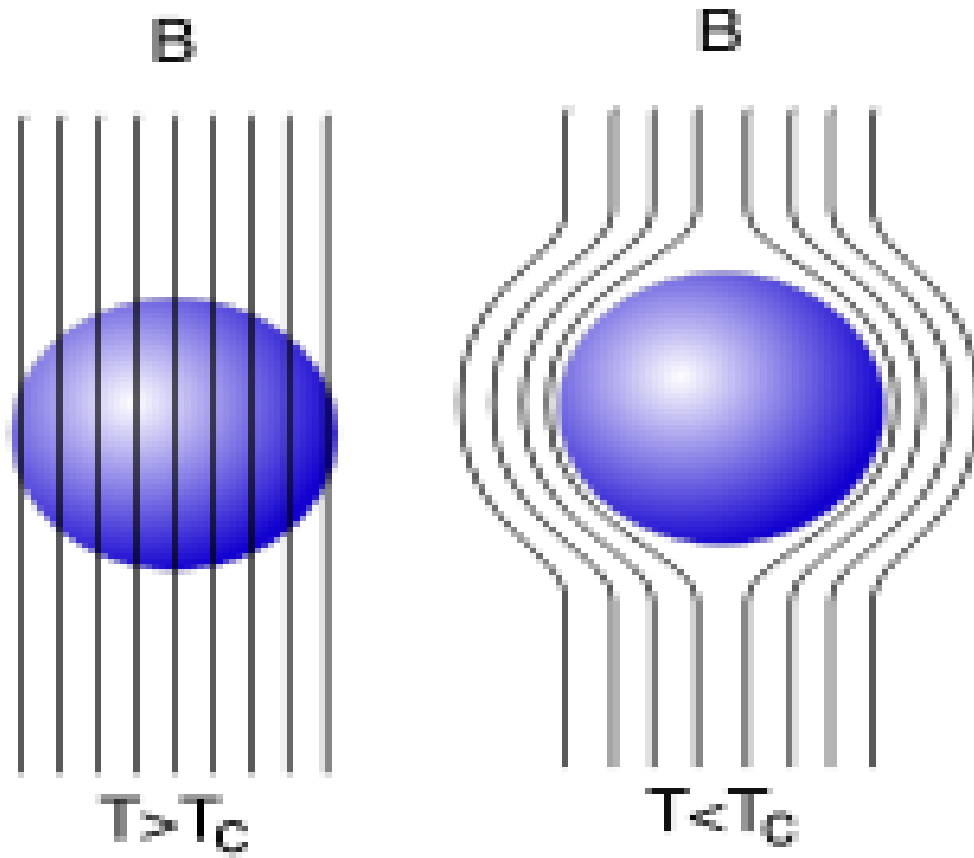
Fig. 1.10 Magnetic field lines pass through the material for T above
transition temperature ($B_{in} \neq 0$) and below this temperature ($B_{in} = 0$)

Field Hysteresis

In ferromagnetic materials an interesting phenomena known as hysteresis is observed. When the material is magnetized by a high external field, the sample will become saturated and the "saturation" moment is observed. If the external field is then reduced the observation is that the magnetic moment does not reduce to zero when the external field is zero, like in the cases of diamagnetic and paramagnetic materials. Instead we see that there is still a non-zero moment when the external field is zero this is known as the remnant moment. If the field value is reduced continually the material will be saturated with the moments lined in the opposite direction. From this point increasing the field back toward positive values of the H field will create the features seen in the field hysteresis loop (Fig. 1.11).
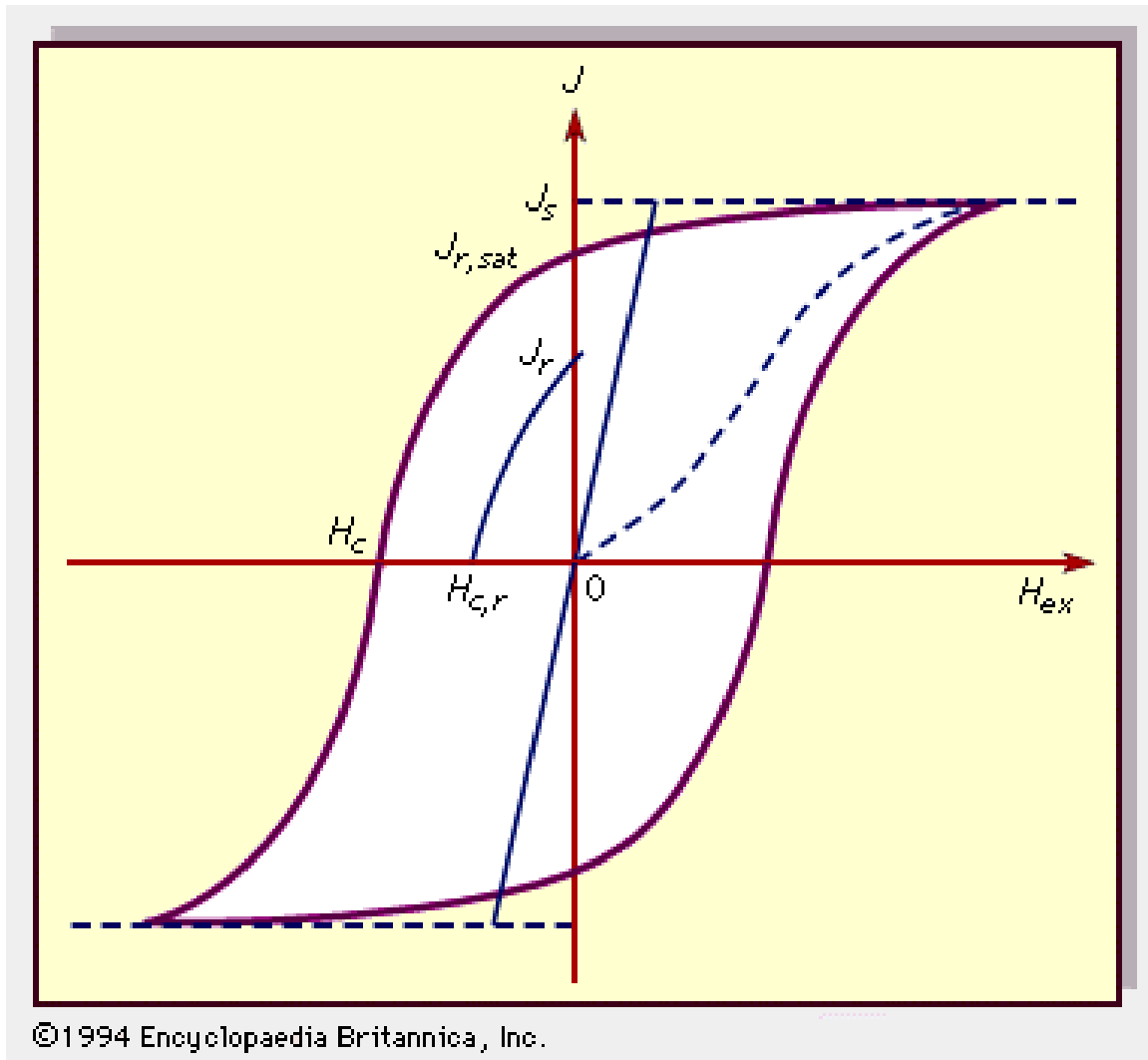
Fig. 1.11 Field hysteresis curve plot with various important points referenced. (J) magnetic moment (H_{ex}) external field strength (J_s) saturation moment ($J_{r, sat}$) remnant moment (H_c) coercive force field[87]

Magnetic Anisotropy

The process of going from completely disordered to an ordered state is heavily dependent on the orientation of the material in comparison to external field direction. Classified in three directions as hard, easy, and medium axis; these directions classify the ease or difficulty in magnetizing a material in a given orientation (Fig. 1.12). For all magnetic materials there is a preferred (energetically favorably) direction in which the moments of these materials will align. Magnetically isotropic materials have no preferential direction in which to be magnetized. Magnetically anisotropic materials however, have favored directions; an easy axis. These easy axes are directions of spontaneous magnetization and are responsible for materials magnetic properties. Various types of magnetic anisotropy are related to crystal type and symmetry.

1. Magnetocrystalline anisotropy – the energy in a ferro/ferrimagnetic crystal that is necessary to change the magnetic moment, in a single unit cell, from the easy axis to the hard axis [52-54]. The differences in the direction of the easy and hard axis arises from the interaction of the magnetic moment of the individual atoms with the crystal lattice, this is the spin orbit coupling.

2. Stress Anisotropy (Magnetostriction) – When an external field is applied to a ferromagnetic material the dimensions of the domain walls change causing a change in the dimensions of the overall material. Therefore depending on the direction in which this field is applied will vary the outcome of the change the material [81].

If such materials show evidence of no domains or a very low number of domains higher energy may be necessary to rotate the magnetic moments, resulting in a large coercivity in the field hysteresis plot. Those materials with a large number of domains are more easily influenced by the external field through the movement of the domain walls; these materials will show a smaller coercivity in the field hysteresis curve. These are known as hard and soft magnetic materials respectively.
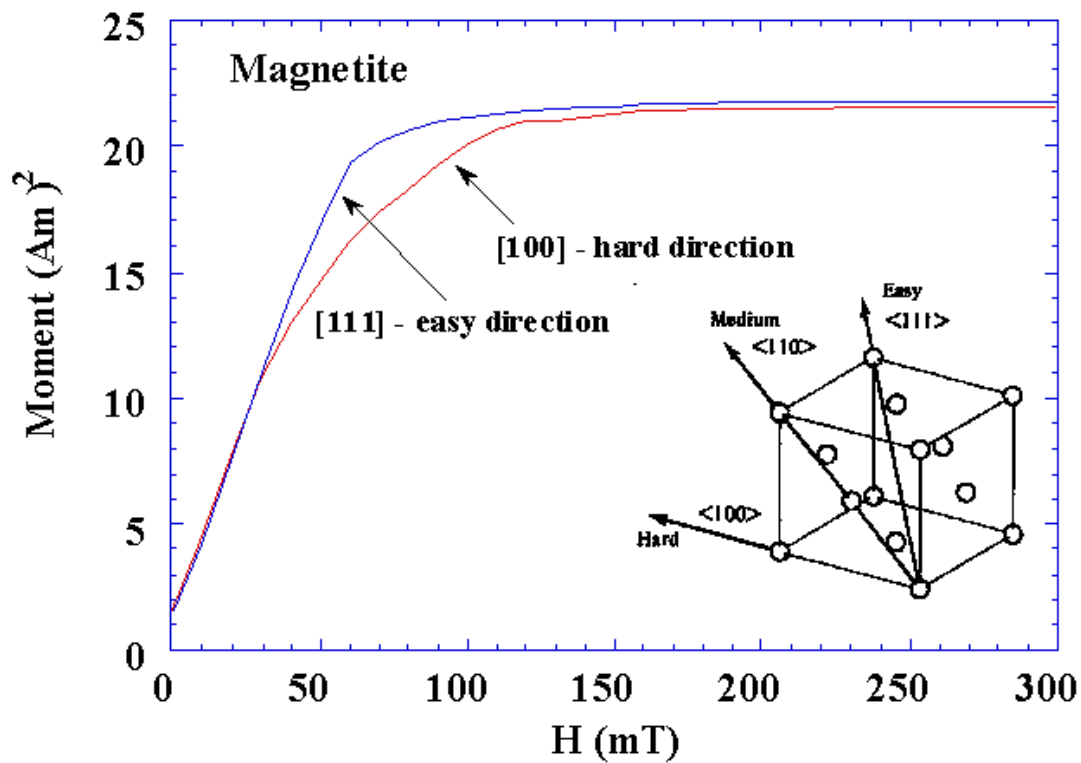
Fig. 1.12 Initial magnetization curve for magnetite showing the difference
in magnetization along the hard and easy axis.

CHAPTER 2

SAMPLE PREPARATIONS AND GROWTH

In order to prove or disprove the existence of AH and H states in pure Dy metal we grow

various thin film samples on substrates of glass. In this section I present the method of

magnetron sputtering and the conditions of the sample preparation chamber used to make these

thin film samples.

Magnetron Sputtering

In magnetron sputtering a control gun which is outfitted with a metal target is used in an

environment kept at constant pressure with an ideal gas. This ideal gas is used to assist in the

formation of the plasma that aids in the transportation of the pure metal from target to substrate.

The method of magnetron sputtering consists of a DC power source gun outfitted with

magnets oriented in a circular ring pattern. These magnets are positioned such that the outer ring

consists of magnets situated such that their poles are aligned i.e. all north or south. The central

magnet's polarity is opposite of those it is enclosed by. With this arrangement the magnetic field

observed is semi-toroidal in shape (Fig. 2.1).
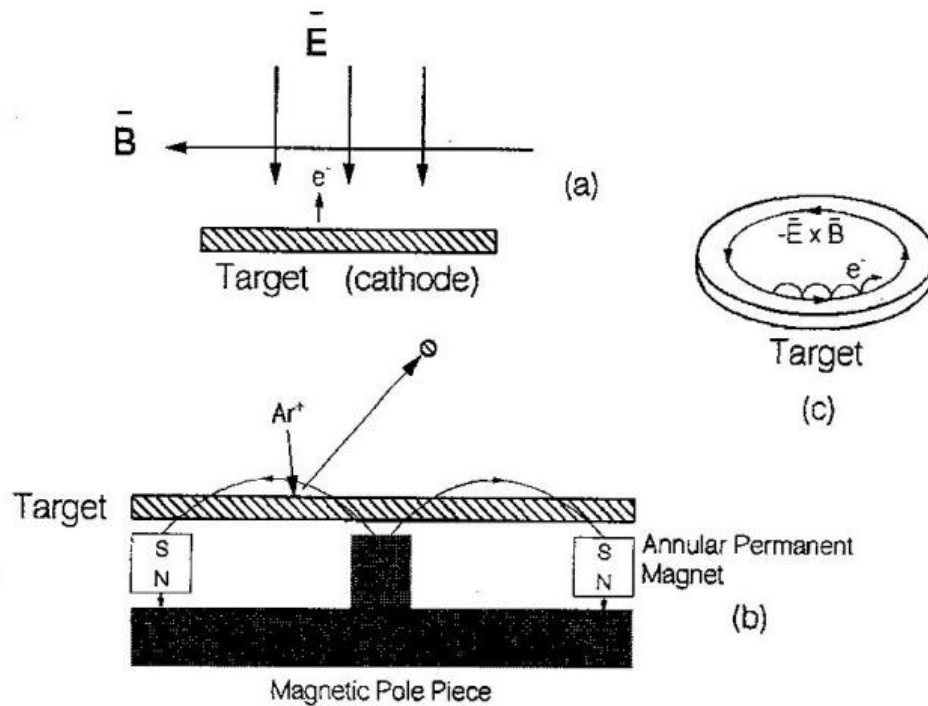
Fig. 2.1 Basic diagram of the magnetron sputtering process [61]

The magnetic field (B field) coupled with the created electric field (E field) from the power source of the guns creates a $\vec{E} \times \vec{B}$ force field. The energy stored in this field is enough to cause valance electrons to circle in the path of this force [61]. With the addition of the presence of the Ar gas these excited electrons can collide with these Ar atoms ionizing them and creating plasma. This plasma of Ar^+ atoms is accelerated toward the metal target and collides. This collision ejects the metal from the target and the potential difference of the power source moves the metal ions toward the substrate.

The sample preparation chamber is operated at an argon pressure of 3mtorr and the power settings of the control guns are managed by the power regulators. This constant gas pressure is maintained by a butterfly valve connected between the turbo pump and the main sputtering chamber. With the gas pressure held constant we can vary the sputtering rate by adjusting the power settings of the gun controller. Sputtering rates are kept low in order to maintain a fairly uniform growth pattern.

Magnetic Materials

As stated previously the magnetic response of various materials is related to their electronic configuration. The interactions between neighboring atoms and the energetic connections of these atoms with the external field determine their magnetic behavior. A list of some of the standard magnetic configurations is shown below (Fig. 2.2).
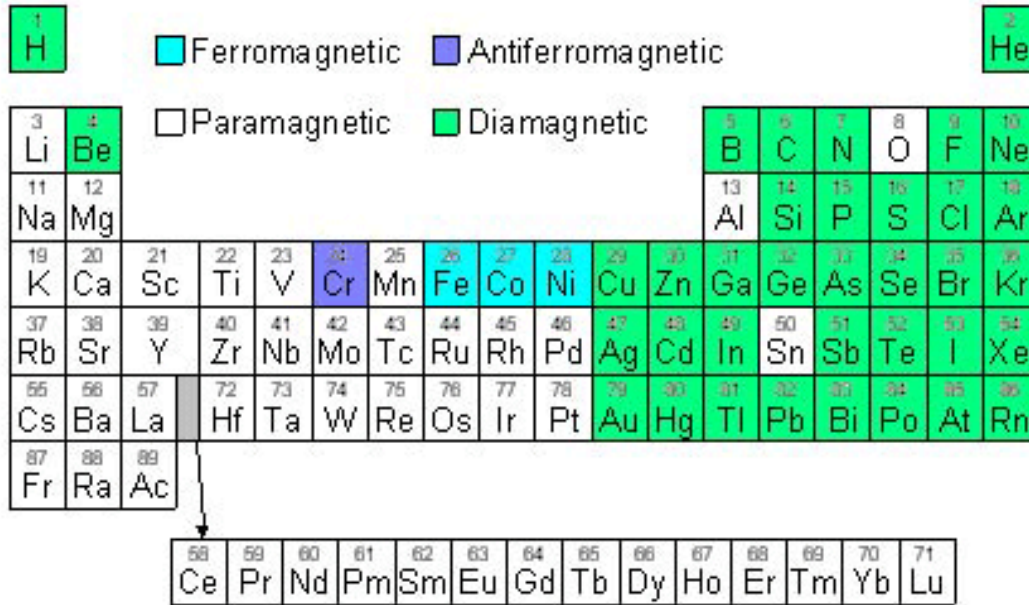
Fig. 2.2 Periodic table representing room temperature magnetic configurations of the elements.

Dysprosium meaning "hard to get at" is a Lanthanide rare earth element atomic number 66, it is dull silver in color. Due to its nature of being easily oxidized Dysprosium is rarely found in nature as a free element it is most commonly found as an element in other materials. Dysprosium has 7 naturally occurring isotopes of these the most stable and therefore most common is Dy-164. Dysprosium has a high thermal neutron absorption cross-section, making it a prime candidate for alloys in control rods for nuclear reactors. Dysprosium exhibits multiple states of magnetic behavior. The existence of these states is attributed to the inherent magnetic anisotropy of Dy and the spin orbit coupling of the neighboring atoms in Dy metal [].

$$\text{Dy: } 1s^2 \, 2s^2p^6 \, 3s^2p^6d^{10} \, 4s^2p^6d^{10}f^{10} \, 5s^2p^6 \, 6s^2$$
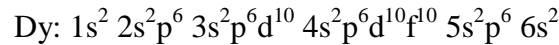
Gadolinium is also a period 6 rare earth element, atomic number 64. It is a silvery-white, malleable and ductile metal. Gadolinium like Dysprosium is not found in nature as a free element. Gadolinium was first detected by methods of spectroscopy in 1880. Gadolinium and Dysprosium are very similar in their electronic configurations and therefore have similar physical properties.

$$\text{Gd: } 1s^2 \, 2s^2p^6 \, 3s^2p^6d^{10} \, 4s^2p^6d^{10}f^7 \, 5s^2p^6d^1 \, 6s^2$$
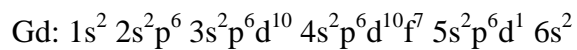
Both metals have hexagonal closed packed crystal structures and nearly equal unit cell dimensions. However, due to the differences in the configurations of their 4f and 5d sub shells the existence of some magnetic states are not seen in both materials. These subtle differences may also account for the large differences in the Curie temperatures. Gadolinium below its curie temperature (~295K "bulk") behaves as a Ferromagnet. Dysprosium on the other hand behaves as a Ferromagnet below its Curie temperature (~85K). However, between this and ~179K (Neel Temperature) Dy exhibits a type of AntiFerromagnetic behavior known as Helimagnetism. Above ~179K Dy behaves as a paramagnet giving it multiple regions of interesting magnetic properties [36].

Both Dy and Gd are high Z rare earth metals and therefore the thin film samples are easily oxidized, thus in the sputtering process buffer and cap layers of Ag metal are used to reduce the rate of oxidation of these metals. Silver has a face centered cubic (FCC) crystal

structure. Though Ag is useful as a protective coating the difference in the crystal structure of Ag vs Gd or Dy can cause dislocations in the stacking of the magnetic materials. These types of features present in the extra peaks seen in the X-Ray measurements in subsequent chapters.

The samples are grown on high quality pieces of quartz glass with dimensions approximately .5 x .2 x 2.5cm^3 (.5 x .2 x 1cm^3 after cutting). The method for preparing the glass for the sputtering chamber is outlined here.

1.) Glass substrate is cleaned in soap solution with mechanical brush.

2.) Wash with deionized water.

3.) Dry with high purity Nitrogen gas.

4.) Secure glass onto substrate holder.

It is important to make sure that the substrate is completely dry before putting into deposition chamber, as excess water molecules can have a negative effect on system pressure.

Sputtering Chamber

Samples are created in a "home" designed sputtering chamber. The chamber is an ultra high vacuum (UHV) chamber with a base pressure on the order 10^{-9}torr. It contains three separate AJA sputtering guns each with their own power supplies and water lines. Each gun is equipped with a shutter screen which stops the stream of ionized metal from reaching the substrate material. These shutters are opened and closed through pressure valves controlled by a flow of nitrogen gas. Nitrogen gas is also used in bringing the main chamber to atmospheric

pressure when the targets of the guns need to be replaced or swapped for a different material. Centered above the substrate rack is an INFICON quartz crystal thickness monitor used to monitor the amount of deposited material in each sample preparation. The thickness monitor is calibrated using a stylus profilimeter. Substrates are introduced into the main chamber through a transfer rail, which has its own system of pumps to reach the base pressure needed for transfer.

To achieve the low pressures needed in the sputtering process the system employs the use of three pumping stages. Stage one is a mechanical pump which is the first to be switched on after opening the chamber to atmospheric pressures. Alone this mechanical pump can achieve a pressure on the order of 10mtorr. After a few minutes of running the pressure should stabilize, once this has happened stage two is started. Stage two consists of switching on the large turbo pump. The large turbo pump is water cooled so care should be taken to make sure that the flow of water is on and that the chiller is running at a temperature of 14 °C. Attached to the large turbo pump is a flow control valve also known as the butterfly valve. This valve is used to regulate the affect of the turbo pump on the main chamber. It is set in the open position to reduce the pressure of the main chamber and other positions are used to maintain constant pressure during sputtering.

After a time of approximately 30 minutes the turbo pump should be able to reduce the base pressure to an order of $10^{-(6,7)}$torr if the pressure does not drop below 10^{-5}torr there is potentially a large leak in the system. At this point the pressure is sufficiently low enough to turn on the low pressure gauge. Sometimes it is necessary to heat the inside of the chamber, for

an hour or two, to further reduce the pressure by vaporizing some of the metals which can then be sucked out by the vacuum. The sputtering chamber was designed with an internal heating element for this task it can also be used to heat substrates during sample growth. Leaving the turbo pump to run for a period of several hours is sufficient time to stabilize a low pressure region on low orders of 10^{-8} torr, or even to order 10^{-9} torr. This is a sufficient pressure to start stage three which is the ion pump. The ion pump acts as a getter to remove impurities from the vacuum system.

Before the substrates are introduced to the sputtering chamber, they are cleaned by the method outlined above. Once the substrate is cleaned and dried the sputtering system is started. This setup procedure is done by turning on all relevant control and monitoring systems. First the computer which controls the opening and closing of the gun shutters is turned on and the controller program loaded a thickness monitor is also switched on. The ion pump controller is switched off and the butterfly control valve is switched to a preset 30% open position. The sputtering guns are water cooled and therefore we must switch on a valve which circulates chilled water throughout all the target guns. To finish the Ar gas is pumped into the chamber and once the base pressure has stabilized we are then able to turn on the guns power supplies. Failure to turn on the water or the gas will result in indicator light flashing stating that the water is not on or that the plasma is not being created because of insufficient gas pressure. With the power supplies now on a check is made of the power regulator settings with the most recent previous settings of power, current, and voltage. Once the monitor and control system is initialized the substrate is loaded onto the transport arm. The transport compartment is closed

and evacuated in stages. Stage one consists of a small mechanical pump which reduces the pressure onto the order of 10mtorr. Once this pressure is reached a second small turbo pump is switched on which will further reduce the pressure nearer to the 3mtorr of the larger chamber. When the base pressure is achieved the gate valve can be opened and the transport arm fed into the main chamber and the sample substrate situated on the rack for deposition. The transport arm is removed from the main chamber the gate valve is closed and the butterfly valve is now set to maintain a constant pressure of 3mtorr. From previous depositions of new target materials we calculate the deposition rates based off of the gun regulators. This information is input into the computer to control the switching of the gun shutters at the start of deposition and once the deposition is complete. The control for the gun shutters can be done manually by pressing the relief valves on the back of each individual sputter gun or by computer control. The computer control is a LabView program titled sputcont.vi immediately accessible once the computer has started. In this program there is a GUI interface in which information such as desired thickness, sputtering rate, and which gun to fire can be set. Co-sputtering can be achieved by selecting more than one gun at a time; one would need to do the necessary calculations to determine the rate to achieve desired proportions. Clicking the corresponding gun button and inputting the desired thickness and calculated rate gives the program the necessary inputs to start the sputtering. Pressing start will run the program, opening the shutter(s) of the corresponding gun(s) the program will continue to run until: the input thickness is reached or the stop button is pressed. Although the computer will close the gun shutter when the desired thickness is reached one

should still periodically watch the computer as the sputtering rate can change during deposition causing the shutters to close prematurely or an overdue time.

When the sputtering is complete the computer is switched off followed by the deposition thickness monitor. The butterfly valve is reset to the fixed partially open position and the gun power supplies are switched off. The sample transfer gate valve is opened and the completed sample is retrieved from the main chamber. Once the sample is back in the transport portion of the chamber the gate valve is closed and the smaller turbo pump is switched off, at this point the water and the Ar gas flow can be shut off. When the pressure in the transport stage has reached a level sufficiently close to atmospheric Nitrogen gas is pumped into the transport stage to force it open, the sample is removed. Pending whether or not the sample will be measured immediately or sometime later the sample will be placed in a vacuum sealed bag or in a desicator for future measurement.

The deposition rates as well as the thickness of the samples are measured by a thickness monitor. The thickness monitor consists of a piece of crystal quartz that vibrates at a set frequency. The information such as the density of the material being sputtered is saved into the monitor's memory in a film number. When a film number is selected and sputtering begins the deposited material is dispersed throughout the chamber and covers both the substrate and the deposition crystal. As material is deposited the frequency of oscillation of the quartz changes this change is frequency is calculated as the material thickness. The computer controlling the shutters also calculates a thickness however this thickness is simply a calculation based off of the

input sputtering rate and the elapsed time; the thickness monitor is a far more accurate means of determining the amount of sputtered material. After many depositions the crystal needs to be changed, the thickness monitor does have a setting in which to determine the lifetime of the crystal. On the main screen simply press "1" which will give a percentage. This percentage is the amount of remaining life of the crystal i.e. a higher percentage the shorter the amount of time of available use. As the use of the crystal is prolonged the observed, sputtering rate and thickness become less and less reliable.

CHAPTER 3

MEASURING DEVICES METHODS AND SAMPLE CHARACTERIZATION

There are many ways in which the magnetic properties of a sample can be measured. The preventive factors of these measurements are usually limited to; cost, accuracy, availability and overall requirements on the measured values. For our measurements we have access to some of the methods described below but a small overview of multiple methods will be given in case more options are available.

Vibrating Sample Magnetometer (VSM)

The VSM is one of many methods used in determining the magnetic moment (magnetization) of a sample [88]. This is primarily due to the fact that the VSM is very accurate and very inexpensive to make or purchase. The VSM is actually derived from a simpler measuring device known as a vibrating coil magnetometer [53]. The VSM is very similar to the vibrating coil magnetometer except for in a VSM the sample is vibrating not the coil. The sample material to be measured vibrates by way of piezoelectric material. In the inception of the VSM audio speakers were used as the means for sample vibration however this method was abandoned due to the interference caused by the audio speaker coil. The sample is placed in between the coils of the VSM electromagnet (Fig. 3.1).
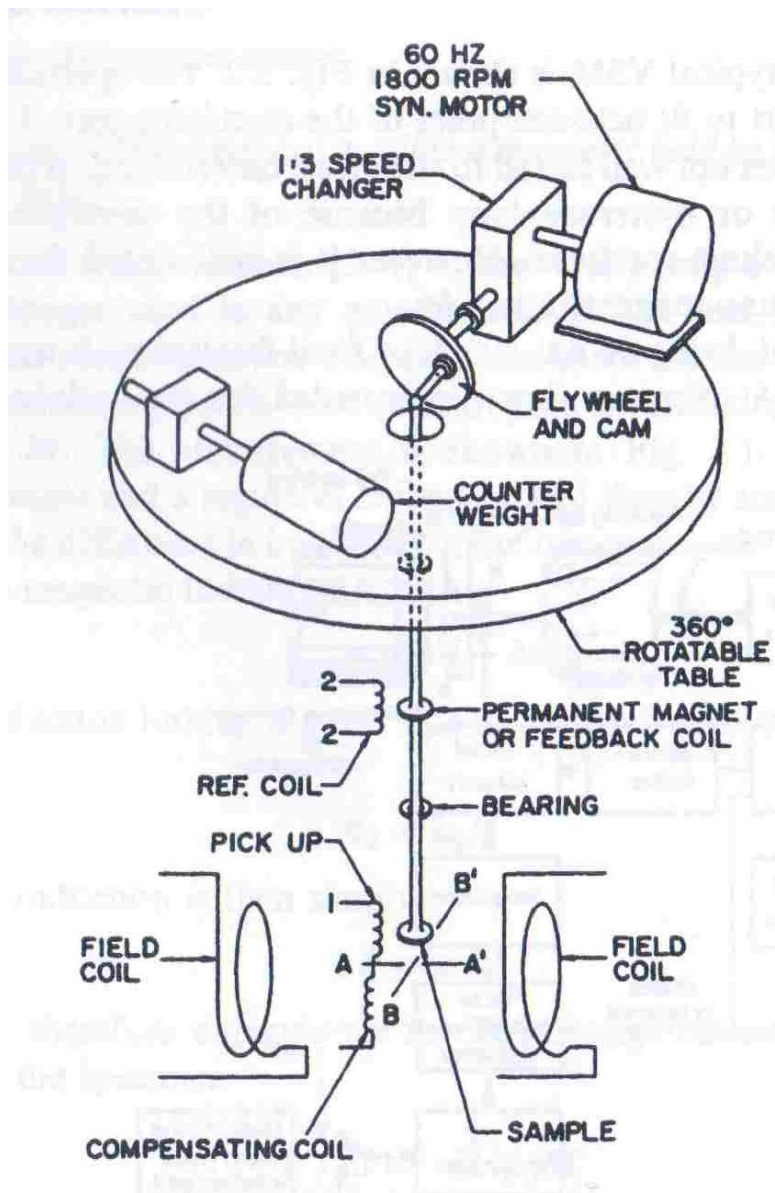
Fig. 3.1 Schematic of the Vibrating Sample Magnetometer (VSM) [53]

The strength of the electromagnet magnetizes the sample material. As the sample vibrates in the presence of the magnetic field a sinusoidal voltage is produced in the VSM pickup coils. This voltage signal is directly proportional to the magnetic moment of the sample.

SQUID Magnetometer
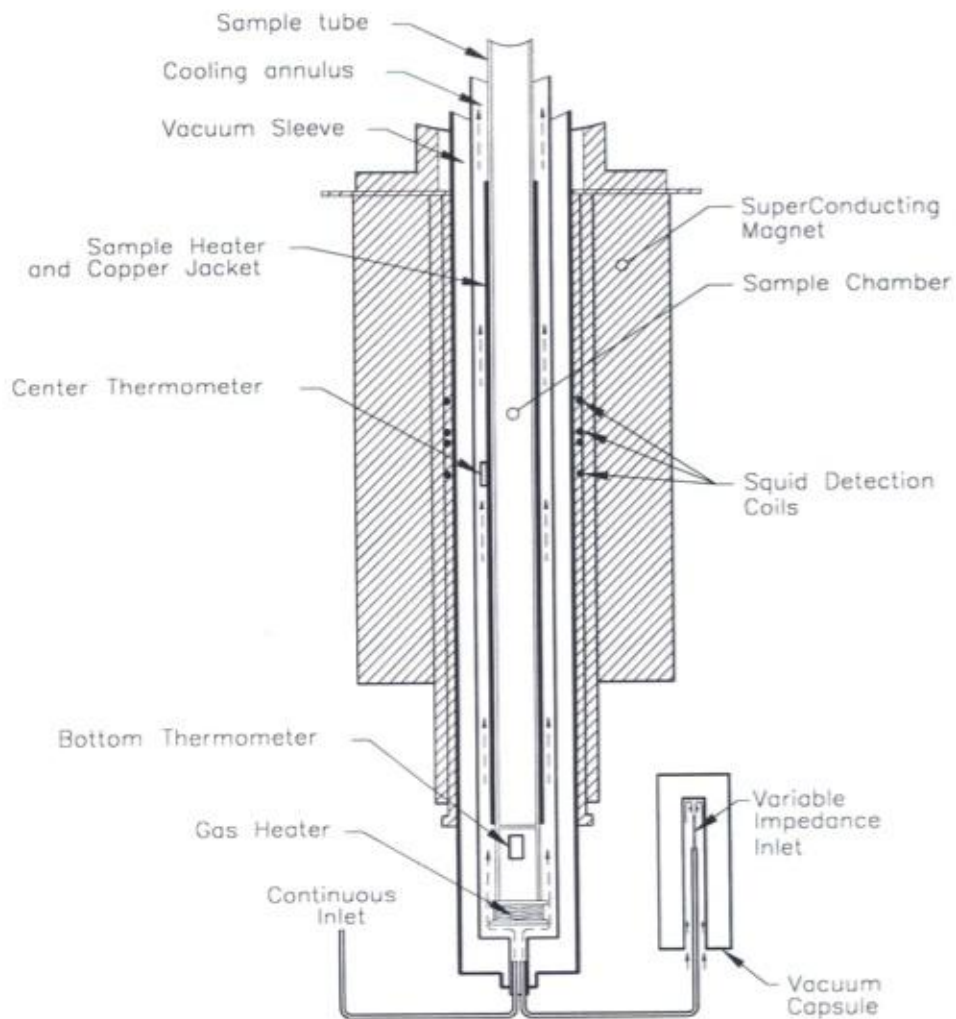
Fig. 3.2 Cross sectional view of the SQUID magnetometer [SQUID Manual]

To measure the field and temperature dependent properties of our thin film samples we need high accuracy measurement tools, use of the Superconducting Quantum Interference Device (SQUID) is necessary. The SQUID magnetometer used for these experiments is highly precise in settings for temperature and field strength. The available temperature ranges of the instrument are from liquid helium (4.22K) up to 400K. This temperature range can be made in steps as small as 0.01K. The system can also record highly accurate temperature readings on the order of .001K [SQUID manual].

The external field strength generated by the SQUID can range from -+$7x10^4$Oe to -$7x10^4$Oe (signs indicate field direction). Like the temperature control the field strength can be varied in small intervals with a resolution as small as $2x10^{-5}$Oe. It can accurately measure the magnetic moment of our samples on the order of 10^{-6}emu in cgs or Am^2 in SI units; 10^{-8} if signals are averaged over a long period of time [SQUID manual]. The entire operation of the SQUID magnetometer is based on the principles of superconductivity and Josephson tunneling also known as the Josephson Effect.

The SQUID magnetometer measures the tunneling of superconducting electron pairs (current) from one superconductor across an insulator into another superconductor [53, 56, 62]. SQUID magnetometers are made up of superconducting loops interrupted by one or more Josephson Junctions. The tunneling effect in these junctions is a direct cause of the magnetic flux induced in the SQUID coil by a magnetized sample. This induced tunneling is therefore directly related to the magnetic moment of the sample. The insulating barrier of the SQUID is

known as a Josephson Junction and the tunneling phenomenon is known as the Josephson Effect [56]. There exist both an AC and DC Josephson Effect, in the DC Josephson effect a current flows across the junction with no external stimuli such as an EM field [86]. When a DC voltage is applied to the junction this creates oscillations in the current across the junction this is the AC Josephson Effect [56].

Josephson Junction

A Josephson Junction consist of two weakly coupled superconducting electrodes. In one of many cases these superconducting electrodes are separated by a weak link or insulator between two superconductors. In these Superconductor Insulator Superconductor (SIS) junctions the effect of current transport (across the insulating barrier) occurs via tunneling of Cooper pairs. If the effect of the coupling between the cooper pairs is weak the current across the junction will be related to the phase difference δ of the currents on the opposite sides of the junction [56]. The relationship for the "supercurrent" that can pass across the junction with zero voltage is given below.

$$I_s = I_0 Sin\delta$$

In the DC SQUID the current only depends on the phase difference between the wave functions of the Cooper pairs in the two paths (Fig. 3.3).
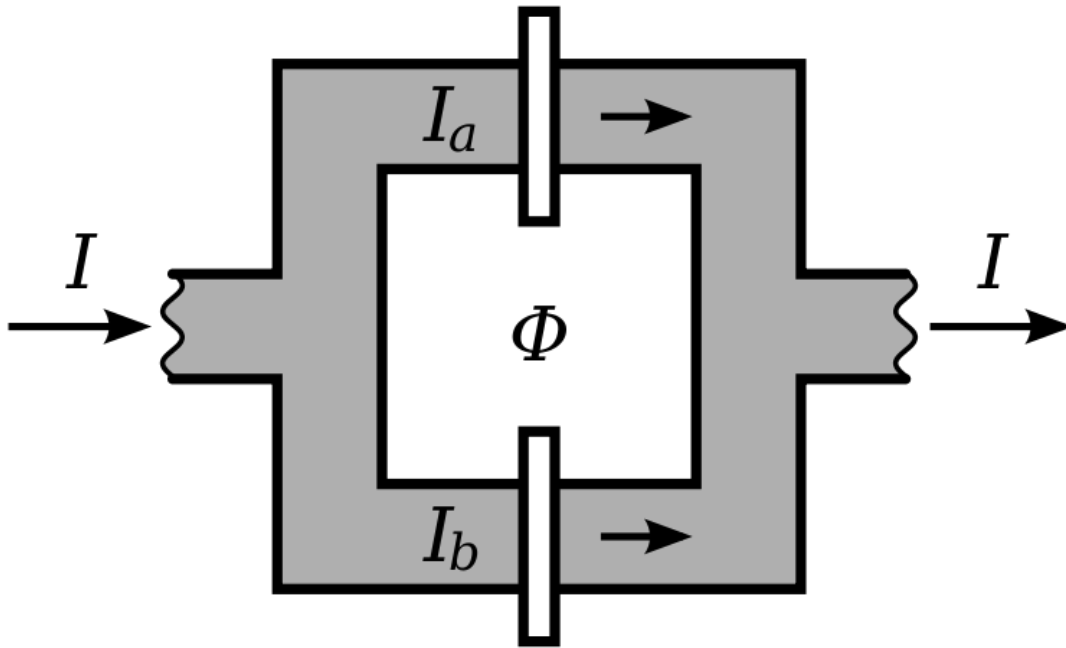
Fig. 3.3 Josephson junction consisting of two weak links separating the two semiconducting paths. This is the DC Josephson junction configuration.

In each of the two paths the value of the current is I/2. The current in either of the upper or lower branches will be modulated by the flux ϕ. If the value of the magnetic flux is high enough the current in one of the branches will reach a critical value. If the critical value of the current is exceeded a voltage is induced across the junctions and the phase difference is no longer the constant relationship as described above but becomes time varying with a frequency given below(AC Josephson effect) [56].

$$\frac{d\delta}{dt} = \left. 2eU \middle/ \hbar \right. = \left. 2\pi U \middle/ \phi_0 \right.$$

$$\phi_0 = 2.067834 \times 10^{-15} Wb$$

Where U is the voltage developed across the junction and ϕ_0 is the magnetic flux quantum.

X –Ray Diffraction (XRD)

A very informative and non destructive technique used in determining sample orientation is the method of XRD. It can be used to determine characteristics of a sample such as crystalline phases and preferred orientation. There are separate categories of XRD they are divided into types based off of the angular range over which the measurement is taken; Grazing Incidence XRD, low angle ($2\theta < 15°$) and high angle ($2\theta > 15°$).

Crystalline materials are made up of a regular array of atoms spaced in integral amounts in three dimensions these spacing amounts are known as the lattice constants. Atoms on the periodic table have different sizes due to their respective electronic configurations. The size of these atoms and there electronic properties determines the type of crystal structures these atoms will form. Some of these crystalline structures are in the form of; Simple Cubic (SC), Face Centered Cubic (FCC), Body Centered Cubic (BCC), Hexagonal Closed Packed (HCP) (Fig. 3.4).
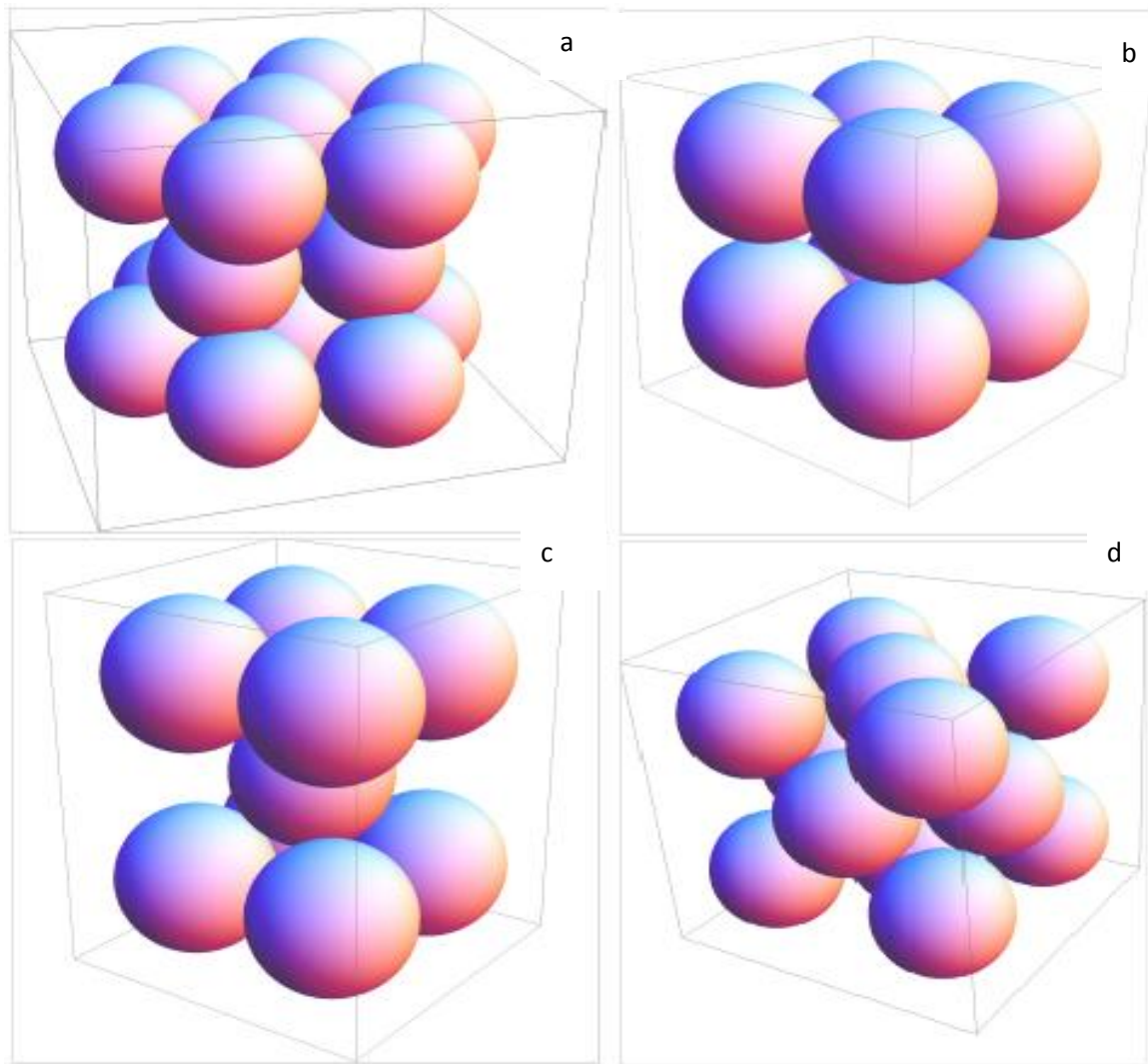
Fig. 3.4 Arrangement of atoms in a.) HCP b.) SC c.) BCC d.) FCC

The arrangements of these unit cells in a solid can be determined by observing the output peak

information from the XRD measurements. X-Rays are incident on the surface of a material to be

studied. From the X-Ray source the rays emerge in phase, once incident on the material the rays

are scattered elastically from the electrons, in multiple layers, bound to the atoms in the lattice (Fig. 3.5).
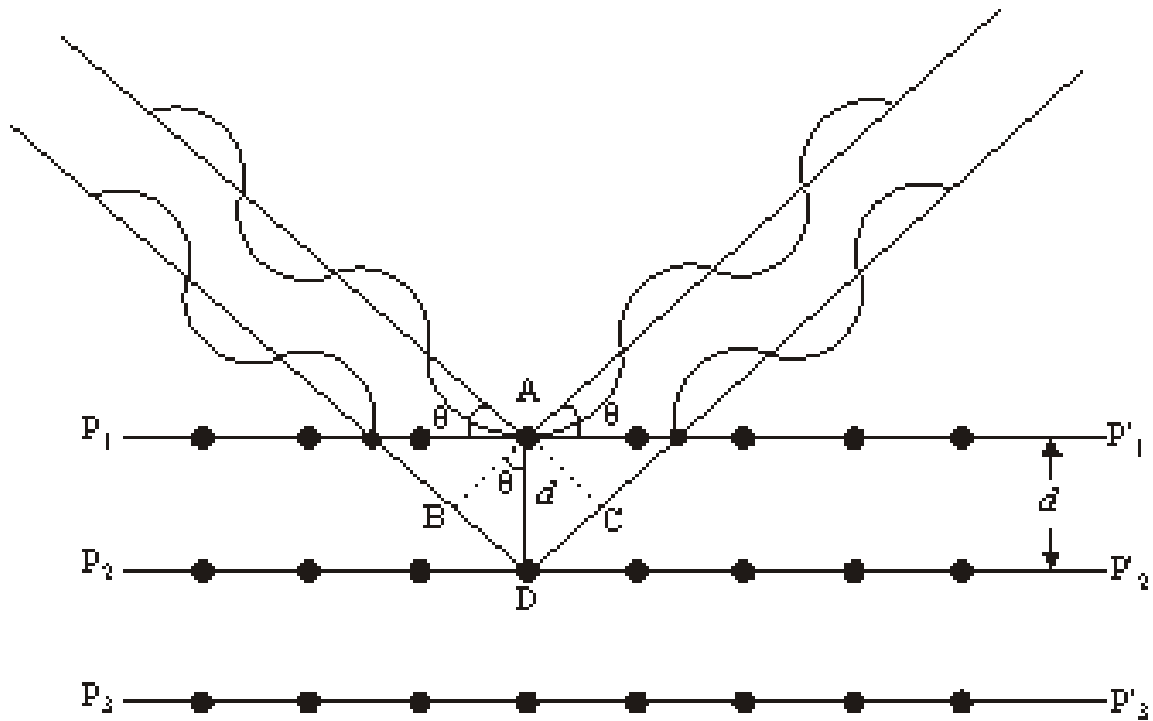
Fig. 3.5 Diagram of X-Ray diffraction measurement indicating the Bragg relationship.

The scattered rays can emerge completely in phase (constructive interference) or out of phase (destructive interference). As the angle of the incident X-Rays are varied the scattered rays go through regions of constructive and destructive interference. These regions are directly related to the spacing between the layers and the wavelength of the X-Rays. The relationship which correlates to complete constructive interference is given by Bragg's Law.

$$2dSin\theta = n\lambda$$

The intensity of the peaks (relative height) is determined by how many of the equivalent planes the X-Rays scatter [52, 59, 79].

CHAPTER 4

MEASUREMENTS OF DY THIN FILMS

Magnetic Thermal Hysteresis M(T) and Field Hysteresis M(H) measurements

Magnetic thermal hysteresis (MTH) was observed in Dy films for the first time at low values of constant external magnetic field strengths in which the temperature was swept from low temperature to approximately room temperature then back to low temperature. In many cases magnetic thermal hysteresis has been shown to exist in multi-material systems in agreement with theoretical calculations. This is the first experimental results showing MTH in single element thin films. In temperature sweeps of pure Dy films, differences in magnetic moment were observed near the low end of the temperature range (20K). We present experimental results that verify this in agreement with theoretical stimulations [9]. Also, due to the presence of top and bottom Ag layers, the Dy films never made the first order ferromagnetic transition at the Curie temperature. A clamping effect is also a potential cause and is attributed stress induced by the Ag cap layers and substrate crystal mismatch. This clamping effect is attributable to the fact that the M(T) measurements show no region of a Ferromagnetic transition but the system stays in the Antiferromagnetic or Helical state on both the cooling and heating branches of these measurements [12, 13].

Magnetic Thermal Hysteresis and Magnetic Field Hysteresis are observed when the temperature and field dependent magnetic properties of a material are reliant on the starting point of the measurement in question. Magnetic properties of materials are dependent on the properties of individual atoms and their response to the presence of an external magnetic field (H). The observed behavior of various materials can be classified as either: Paramagnetic, Diamagnetic, Ferromagnetic, Anti-ferromagnetic, or Ferrimagnetic. In certain Transition Metal / Rare Earth (TM/RE) layered materials, which are labeled as artificial Ferrimagnets due to the Antiferromagnetic coupling between RE and TM layers, an interesting phenomena known as magnetic thermal hysteresis has been observed [1–4]. Experimental results such as these have been approximated using some theoretical models [5, 6]. In Ferromagnets, at the Curie temperature the magnetic ordering of the material shifts from ferromagnetic to paramagnetic phase; and this is the only magnetic transition. However, in some materials, such as Dysprosium, an intermediate phase known as the Antiferromagnetic phase or Helical phase, also exists [7, 8]. We present here measurements indicating that this intermediate phase is the cause of the magnetic thermal hysteresis for thin film samples, where Dy is the only constituent.

The thin film samples used in these experiments were all grown using the method of DC magnetron sputtering system with a base pressure in the Ultra High Vacuum range. The glass used is high quality quartz which was cleaned before sputtering. All samples were grown in a 3mtorr high purity Argon (Ar) gas environment. The settings for the metal control guns, for each respective metal, were all kept at consistent values to assure reproducible results. The metals

used are experimental grade with purities ranging from 99.95% to 99.99%. The Dy films used in this study are protected by 100 Angstrom Ag layers on top and bottom.

Magnetic thermal hysteresis has been observed in many multi component Transition Metal/Rare Earth systems. We observed magnetic thermal hysteresis in multilayer thin film Dy samples measured at constant external magnetic field strength while varying the temperature using a Superconducting Quantum Interference Device (SQUID magnetometer). In these temperature sweeps noticeable differences in magnetic moment were observed near the low end of the temperature range up to 150K. However, when starting at the high end of the temperature scale and making the same measurement this separation is not observed. The large difference in moment at low temperature can also be controlled by the magnitude of the external field strength. As the field strength is increased the spacing decreases as it is decreased the spacing increases.

In this work 50 layer and 120 layer Dy films were investigated. X Ray measurements conducted at room temperature were done in order to show that the sample are pure Dy films (Fig 4.1). In Dy the easy magnetization axis is in the basal plane and therefore perpendicular to the c axis. The XRD pattern shown in figure 4.1 has four diffraction peaks. All of these peaks are due to the Dy. However the presence of the small (100) and even smaller (201) diffraction peaks indicate that the c-axis of the Dy films are not exactly perpendicular to the film surface. However, these extra peaks are small and the effect on the magnetic thermal hysteresis should

not be a large contributing factor. After all this is the first experimental proof that magnetic

thermal hysteresis exists in single component systems.
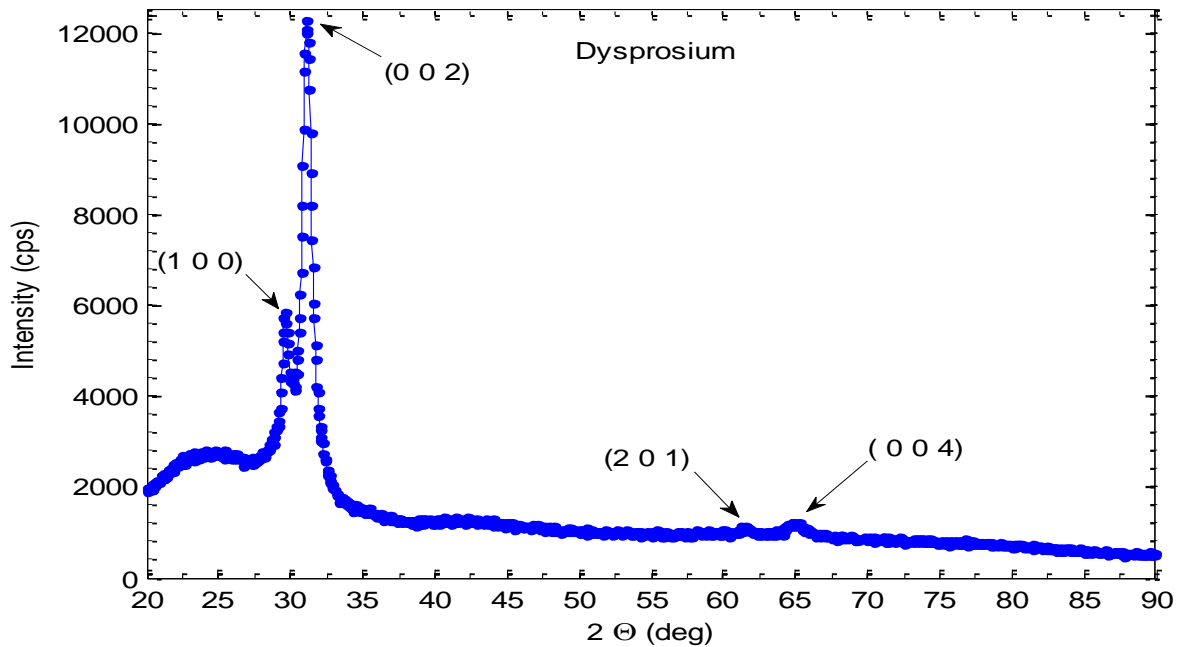
Fig 4.1 X Ray Diffraction measurement conducted on a 120 layer thick Dysprosium sample to indicate the composition of the samples used in this study. Measurements were done using a Copper (Cu) source with wavelength of 1.54184 Å.

The existence of the Alternate Helicity (AH) state, Helical (H) state and the shifting of

the anisotropy axis are the prime candidates for the existence of the magnetic thermal hysteresis

in the Dy films. Theoretically this has been shown to be due to the presence of an Alternate

Helical (AH) state during the heating branch and the presence of a Helical state in the cooling

branch [9]. Calculations have been done to model the effect of the existence of AH and H states

in Dy thin films, which are believed to be the cause of the observed thermal hysteresis. The experimental results in conjunction with the theoretical calculations seek to verify the existence of these states.

After successful completion of the sample growing process the finished sample is quickly removed from the sample chamber. The sample is cut to new dimensions approximately .5 x .25 x 1cm^3. This is done to ensure that the sample will fit inside the sample holder for the SQUID magnetometer. Prior to completion of the sample growth the SQUID is warmed to room temperature under zero field. With the sample placed in the sample holder and attached to the transfer rod the SQUID it is lowered into position to be centered and subsequent measurements made. The centering process starts with saturating the sample under predetermined external field strength; for these measurements the sample was saturated at 50,000 Oe to ensure complete saturation. Next the field is reduced to a lower value, 1,000 Oe, to ensure proper positioning of the largest moment reading. Dy is paramagnetic near room temperature; therefore reducing the field can cause issues with getting strong signals. It is often necessary to reduce the temperature of the SQUID to a lower value, preferably near the Curie point, before commencing the centering procedure.

With centering complete the measuring sequence can be executed. For the field hysteresis curves the field is first reduced to zero then the SQUID is cooled to the desired temperature values. In the case of this experiment we look at three temperature values [10]:

20K – below the Curie point of Dy 85K

90K – approximately near the Curie point of Dy

180K – far from the Curie point of Dy

Once the SQUID has reached the desired temperature value the sample is saturated at 50,000 Oe then a measurement of the moment is taken. The field is reduced in steps of 10,000 Oe taking a measurement at each step until the field strength reaches 10,000 Oe. At this point the next field value is 5,000 Oe and the step size changes to 1,000 Oe for each successive measurement until the field strength reaches -5,000 Oe. At which point the next measurement is taken at -10,000 Oe and the step size is again 10,000 Oe until the field value reaches -50,000 Oe. This is the turning point at which the sequence continues to run only now going from -50,000 Oe back to 50,000 Oe with the same steps as the first path. The results of these measurements are presented below (Figs 4.2 – 4.4). The seemingly rotated graphs are an effect due to the silver cap layers which are diamagnetic.

Dy50 M(H) 20K Inplane
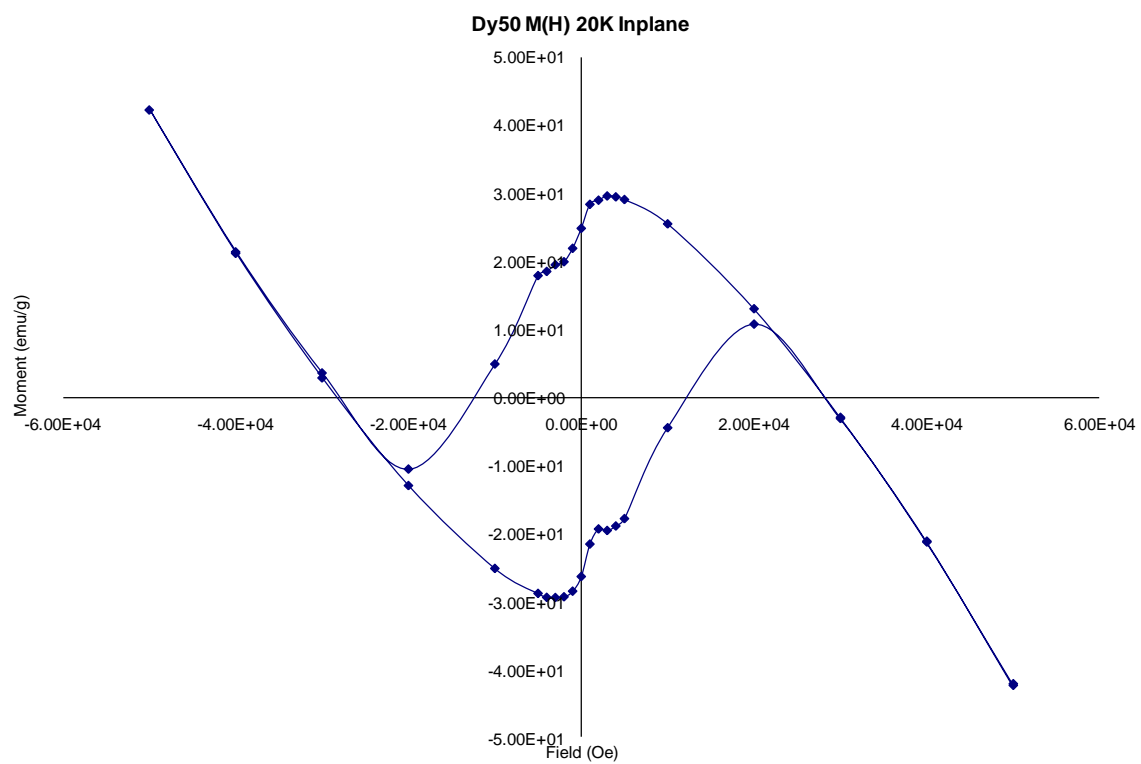
Fig. 4.2 M(H) for 50 layer Dy film at 20K with field direction parallel to the easy axis

Dy50 M(H) 90K Inplane
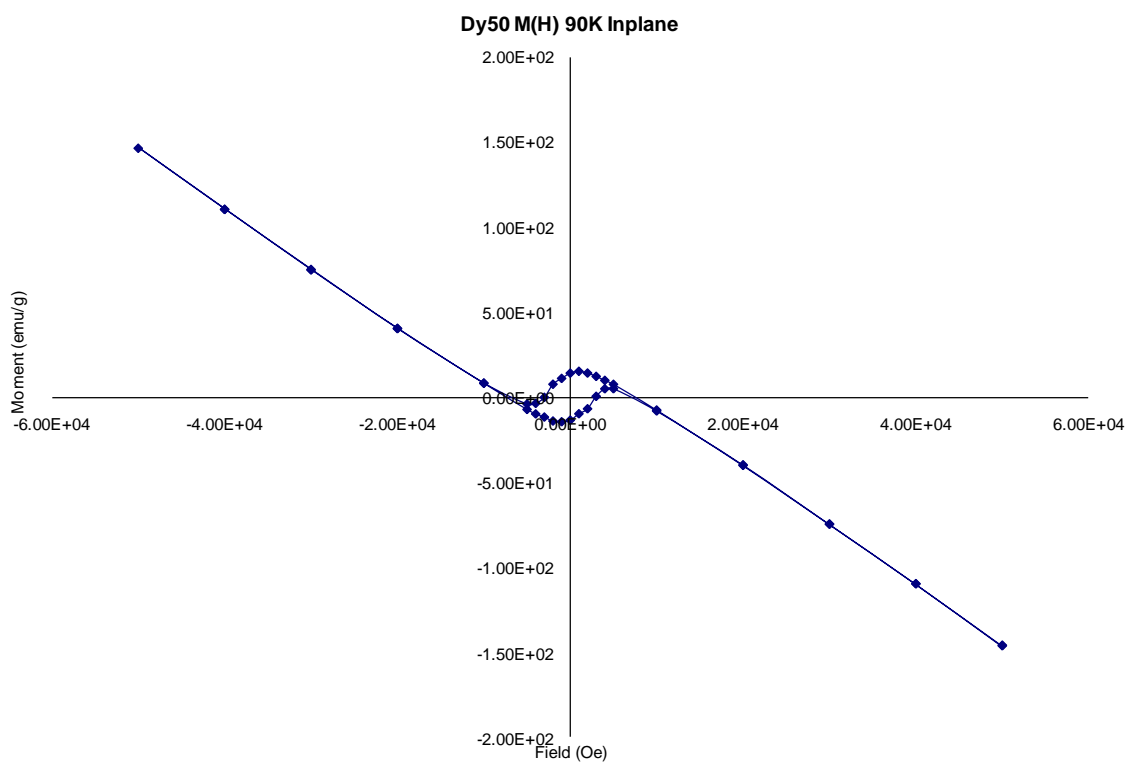
Fig. 4.3 M(H) for 50 layer Dy film at 90K with field direction parallel to
the easy axis
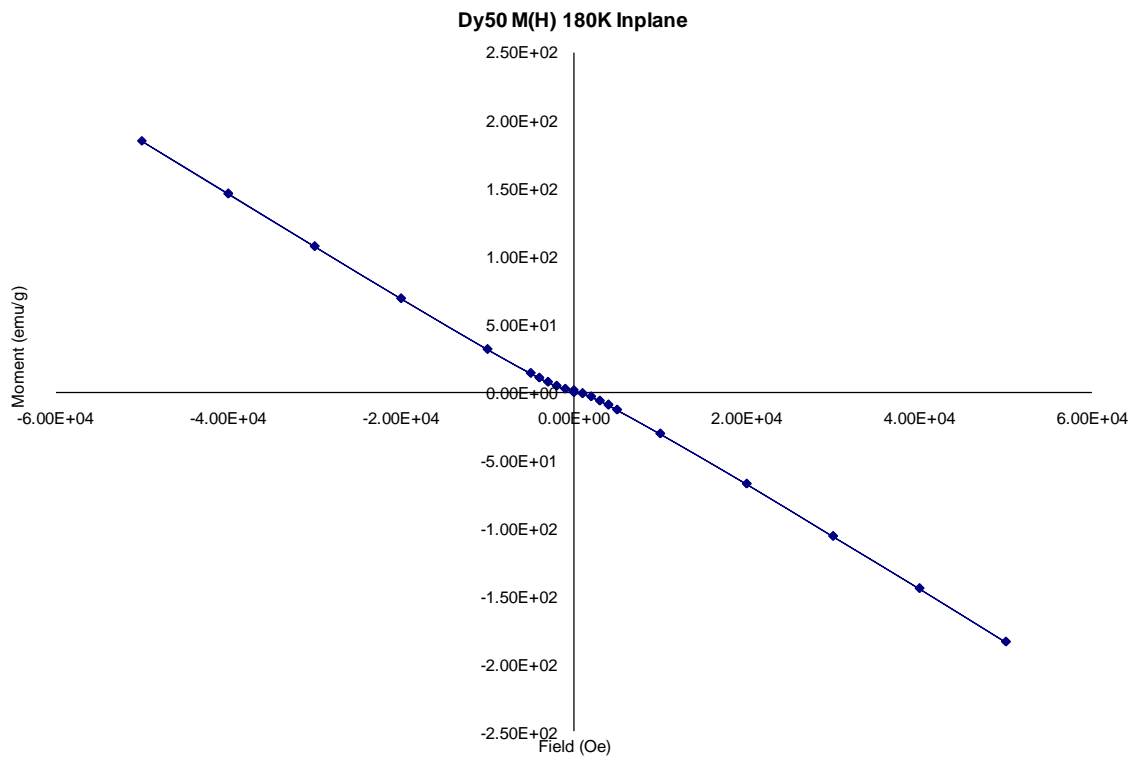
Fig. 4.4 M(H) for 50 layer Dy at 180K with field direction parallel to easy
axis

The effects of the silver layers can be reduced by a couple of different methods. One of these methods is to do a background subtraction of the signal due to the silver layers. The other method involves simply making a measurement of similar samples with no silver layers (Fig. 4.5).
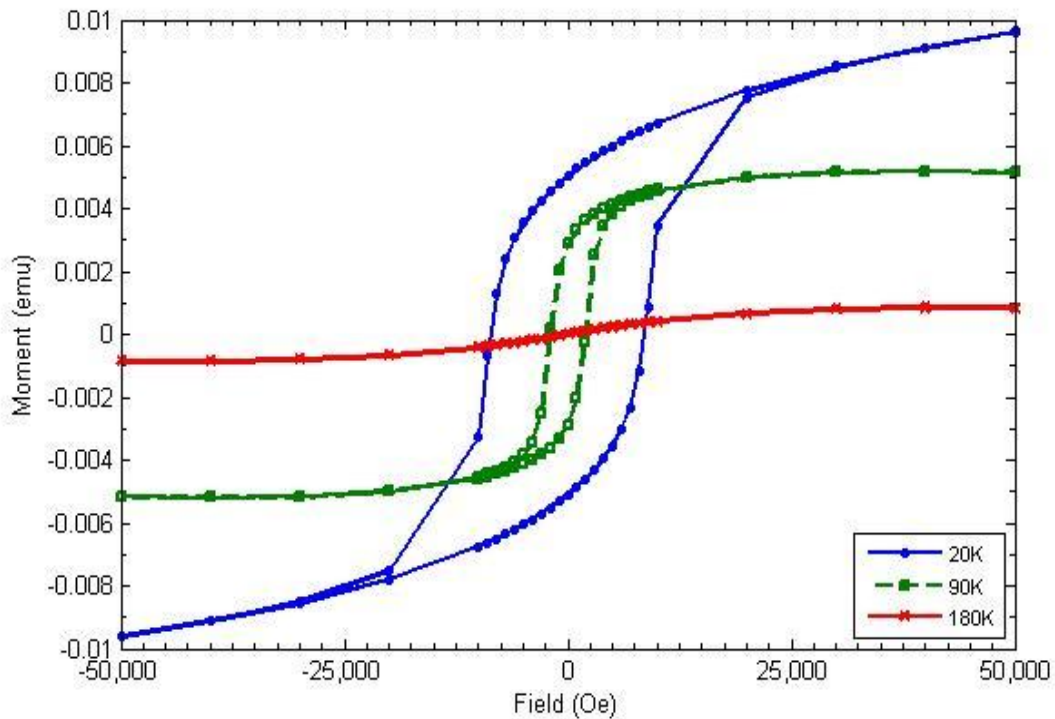
Fig. 4.5 M(H) for a 120 layer Dy film with no Silver (Ag) layers to show how pure Dy behaves as a function of field at various temperatures.

Magnetic Thermal Hysteresis (MTH) Experiment

For the magnetic thermal hysteresis curves the magnetic field is first reduced to zero then the SQUID is cooled to the initial temperature value of 20K. In the case of this experiment we look at three field values for the 50 layer Dy film (450 Oe, 250 Oe, 100 Oe) and four field values for the 120 layer Dy film (1.5K Oe, 450 Oe, 250 Oe, 100 Oe). The range of external field strengths and variations in thickness allow us to observe the field and thickness dependence of the magnetic thermal hysteresis. Once the SQUID has reached 20K the sample is saturated at an external field of 50,000 Oe then reduced to the measuring field, 1.5K Oe, 450 Oe etc. A measurement is taken at this starting point then the temperature is raised in steps of 10K all the way up to 300K taking a measurement at each temperature step. When 300K is reached the sequence continues only this time reducing the temperature in steps of 10K until returning to the low temperature value of 20K.

Magnetic thermal hysteresis measurements show the observable effects of the thickness and measuring field dependencies. For the thinner (50 layer) sample we can see what effect varying the external magnetic field has on the hysteresis (Figs. 4.10a-c). From these figures the temperature at which the separation of the heating and cooling branches occurs is easily observed. The difference in this temperature and the low temperature value is the width of the thermal hysteresis. However, starting this measurement from high temperature shows no difference in the heating or cooling paths (Fig 4.10d).
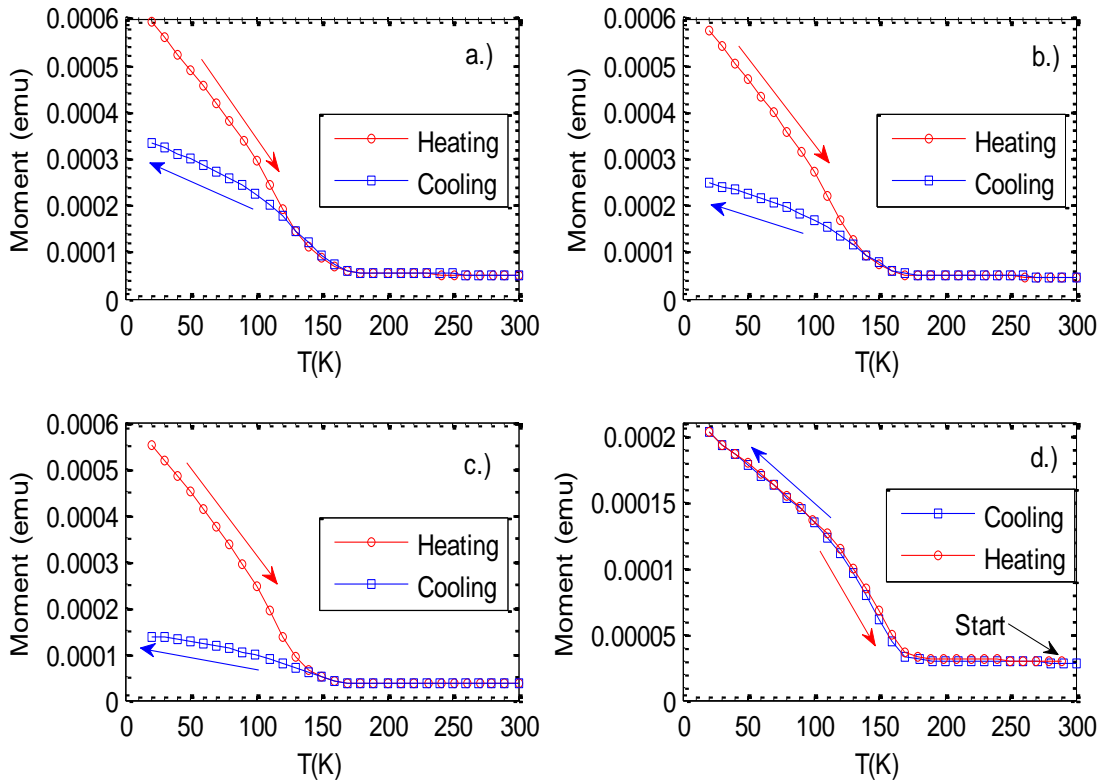
Fig. 4.6 Magnetic thermal hysteresis measurements of a 50 layer Dy thin film. Starting at low temperature (zero field cooling) using a constant measuring field. The effect of raising the measuring field is seen in the multiple figures. a.) 450 Oe, b.) 250 Oe, c.) 100 Oe, in d.) Measurement of the Dy 50 layer thin film starting at room temperature (250 Oe); here there is no observable hysteresis.

The width is tunable by variation of the external magnetic measuring field as well as the sample thickness which is noticed when the thickness of the sample is approximately doubled. With a thicker sample the external field can be set to higher values than previously before the separation disappears. In the 50 layer sample it was evident that as the external field was

increased higher and higher the observable magnetic thermal hysteresis was diminished. In a

thicker sample we can see this effect over a larger external magnetic field range (Fig 4.11 a-d).
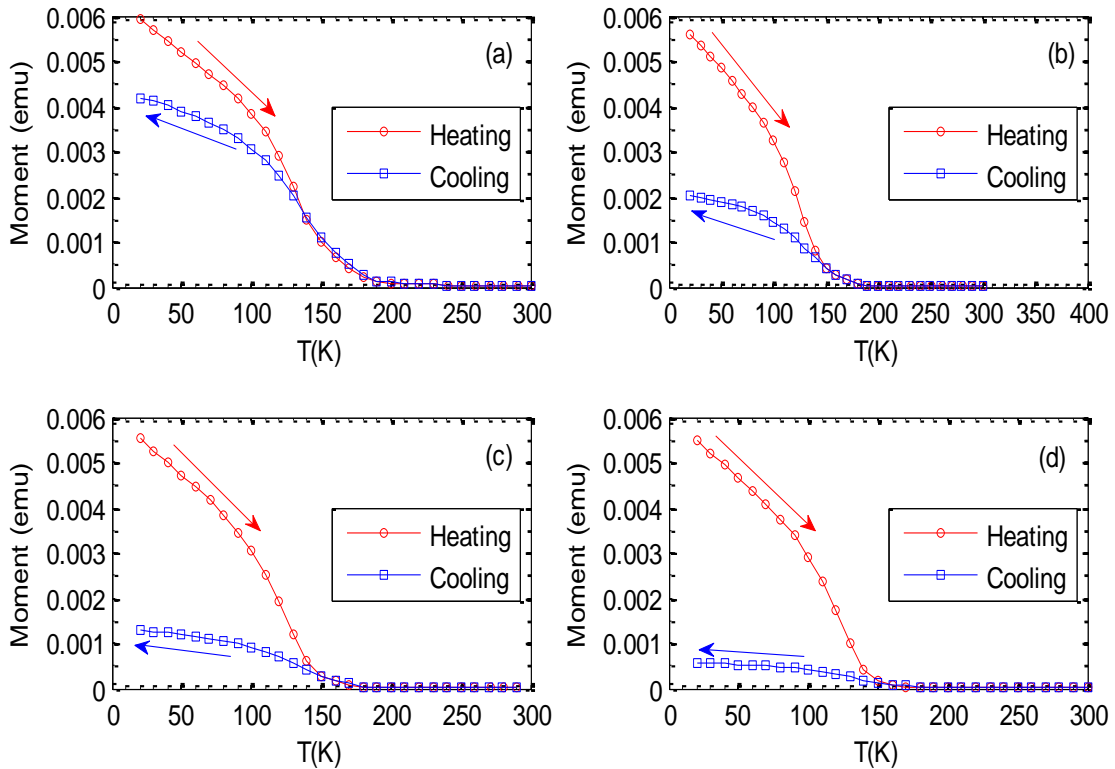
Fig. 4.7 Magnetic thermal hysteresis measurements of a 120 layer Dy thin film. Starting at low temperature (zero field cooling) using a constant measuring field. The effect of raising the measuring field is seen in the multiple figures. a.) 1.5k Oe b.) 450 Oe c.) 250 Oe d.) 100 Oe

In the magnetic thermal hysteresis (MTH) data shown in figures 3 and 4, the

disappearance of the MTH depends on the thickness of the Dy films and the magnitude of the

applied external magnetic field [9]. In general though, the AH and H states merge into one state

in the M(T) curves in a temperature region of 130K -160K [7]. This points to the fact that at some temperature on the heating cycle the AH state is not energetically more favorable than the H state and the domain walls in the AH state disappear and the Dy films transform into the H state. The physical reasons for this are not exactly clear at this point but one can speculate that the external magnetic field at high temperatures is able to make the Dy films single domain. The main effect of these measurements is the decreasing size in the separation of the forward and return paths of the M(T) measurements and the shifting of the temperature for which this happens. As the measuring field increases the separation decreases. Monitoring this gives an indication as to the value of the measuring field that will cause the hysteresis to disappear for the 50 and 120 layer samples (Fig. 4.12). As stated previously the Dy films being measured are protected by 100 Angstrom Ag layers on top and bottom. This creates a clamping effect on the Dy films, which has been observed in Dy/Y multilayers [12, 13] and prevents the first order transition from the Antiferromagnetic Helical State to the Ferromagnetic state at Tc ≈85K as a result of this the saturation nature in the Ferromagnetic region is not seen in these films.
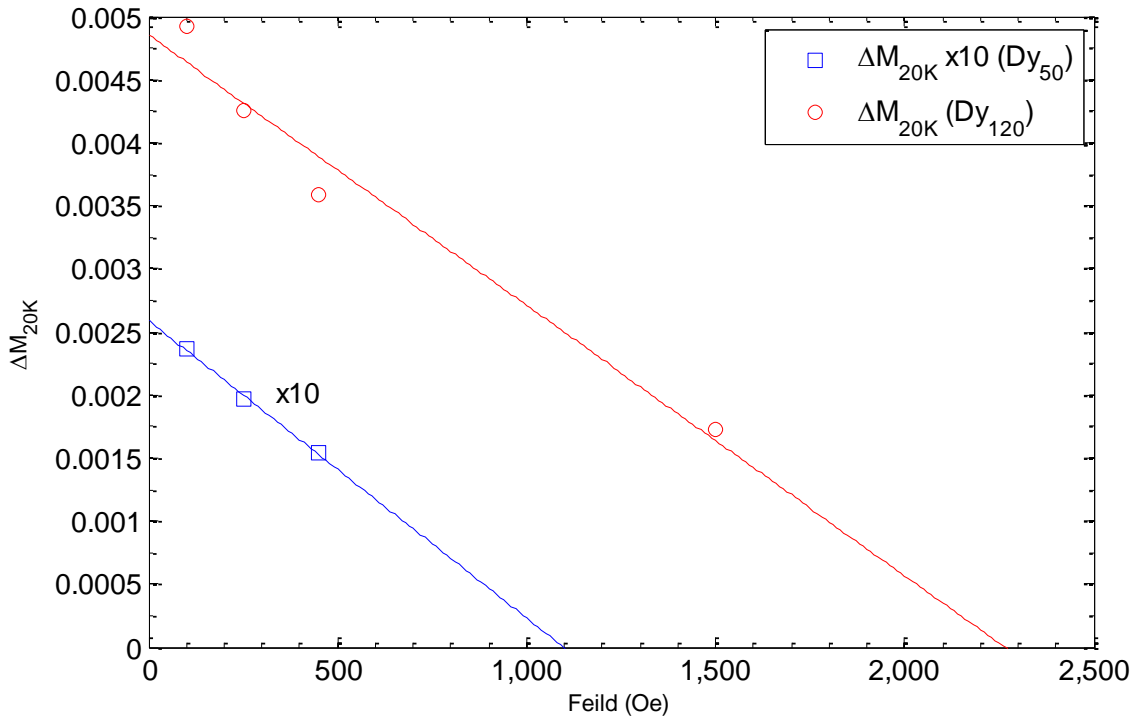
Fig. 4.8 Difference in moment between the heating and cooling branches at 20K for the two Dy films measured as a function of the applied external magnetic field. The lines shown are a linear fit to the data x-axis crossing indicates the approximate external magnetic field value at which magnetic thermal hysteresis will disappear.

Results

In most cases magnetic thermal hysteresis is seen in multi-material films or alloys. In this series of experiments we observed magnetic thermal hysteresis for the first time in thin film samples consisting only of Dysprosium metal. The coexistence of separate Antiferromagnetic states of Dy is believed to be the cause of the thermal hysteresis seen in the Dy thin films; the more energetically favorable state along the separate branch accounts for the difference in moment as seen in the figures [35]. In the AH state the projection of the Dy magnetic moment in

the external magnetic field direction is calculated to be larger than the H state [9].   Changing

the sample thickness as well as the measuring field allows for larger variations in the separation

of the heating and cooling branches at low temperatures. The shape of the MTH curves observed

for the Dy films is vastly different than those observed for artificial Ferrimagnets where there is

Antiferromagnetic coupling is present [1-4]. The experimental results indicate that the observed

MTH is due primarily to the Dy metal and not due to magnetic interaction with other materials.

As mentioned before, magnetic thermal hysteresis has been theoretically calculated for thin Dy

films. However, the theoretical calculations only extend to approximately the Curie temperature

of the Dy films [1-2]. The observed clamping effect due to the presence of the Ag layers

prevents the Ferromagnetic transition in the Dy films and extends the presence of the thermal

hysteresis to very low temperatures. This clamping is due to the strain between the different

lattice constants and crystal structures of the Dy film and Ag cap layers [12, 13]. As a result the

magnetic thermal hysteresis is observed down to 20K. Hence the Dy films stay in the AH state

on the heating cycle and the H state on the cooling cycle allowing the observation of a large

magnetic thermal hysteresis at reasonable external magnetic fields applied in the basal plane of

the Dy films. This point was not taken into account in the calculations and hence the

experimental results differ from the theory in this sense.

CHAPTER 5

MEASUREMENTS OF GD THIN FILMS

M(T) Measurements of Gd Thin Films

Magnetic Thermal Hysteresis (MTH) of Dysprosium (Dy) thin films can be attributed to two key factors, magnetic anisotropy [12, 13] and the existence of two Antiferromagnetic helical states [9] that exist over a wide temperature range. However, in the case of Gadolinium (Gd) there is no hard evidence of any such states in Gd that can be the cause of the MTH seen in the thin film samples presented here though some measurements do indicate within a narrow temperature range that Gd has some spiral spin structure [76]. We investigated Gd thin films of three different thicknesses and observed changes in the magnetic moment at low temperature. In these measurements 33, 100 and 200 layer Gd films were investigated. X Ray measurements conducted at room temperature were done in order to show that the samples are pure Gd films (Fig. 5.1). In Gd the easy magnetization axis is roughly perpendicular to the basal plane (parallel to the c axis) [43, 72]. The XRD pattern shown in (Fig. 5.2) has main peaks related to Gd and one from the top Ag layer. However the presence of the small (100) diffraction peak indicate that the c-axis of the Gd films are not exactly

perpendicular to the film plane. However, these extra peaks are small and the effect on the magnetic thermal hysteresis should not be a large contributing factor. This is the first experimental proof that magnetic thermal hysteresis exists in single Gd film systems. The temperature dependent change in the magnetic anisotropy axis is the prime candidate for the existence of the MTH seen in these Gd films [21, 77].
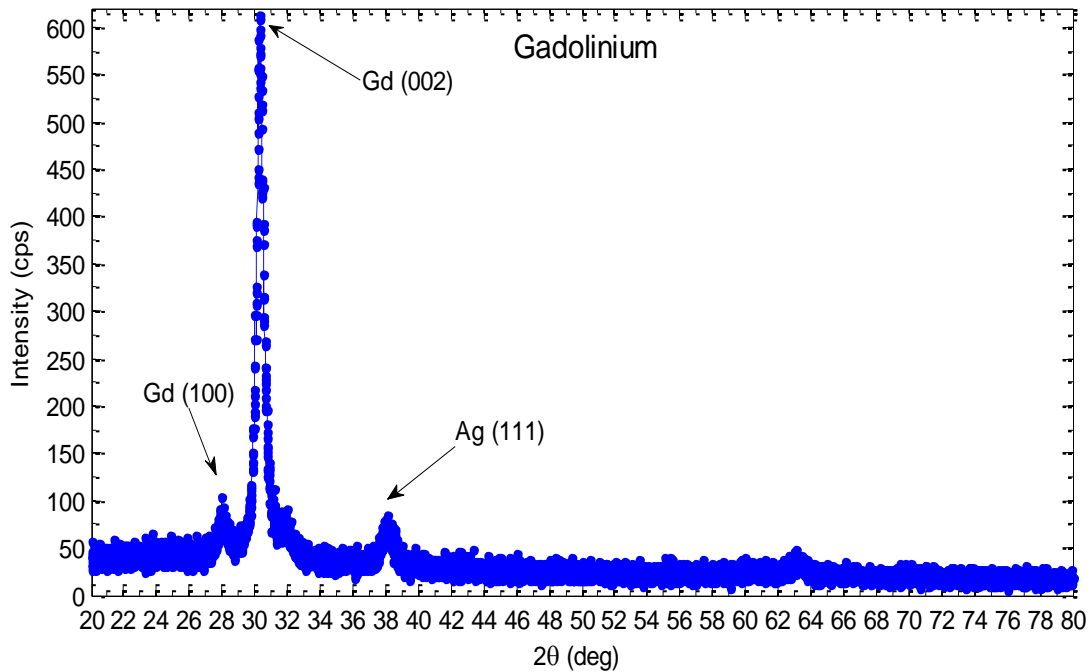
Fig. 5.1 X-Ray diffraction measurement conducted on a 200 layer Gd sample to indicate the composition of the samples used in this study. Measurements were done using a Copper (Cu) source with a wavelength of 1.54184Å

Magnetic thermal hysteresis of the Dy thin films is due to two key factors, magnetic anisotropy and the existence of two helicity states that exist over a wide temperature range.

However, in the case of Gd there is no evidence to the existence of the same helicity states that exist in Dy.

Results for Gd Thin Films

Magnetic thermal hysteresis measurements show the observable effects of the thickness and measuring field dependencies. For the thinner (33 layer) sample we can see what effect varying the external magnetic field has on the hysteresis (Figs. 5.2 a-c). From these figures the temperature at which the separation of the heating and cooling branches occurs is easily observed. The difference in this temperature and the low temperature value is the width of the thermal hysteresis. The width is tunable by variation of the external magnetic measuring field as well as the sample thickness which is noticed when the thickness of the sample is increased.
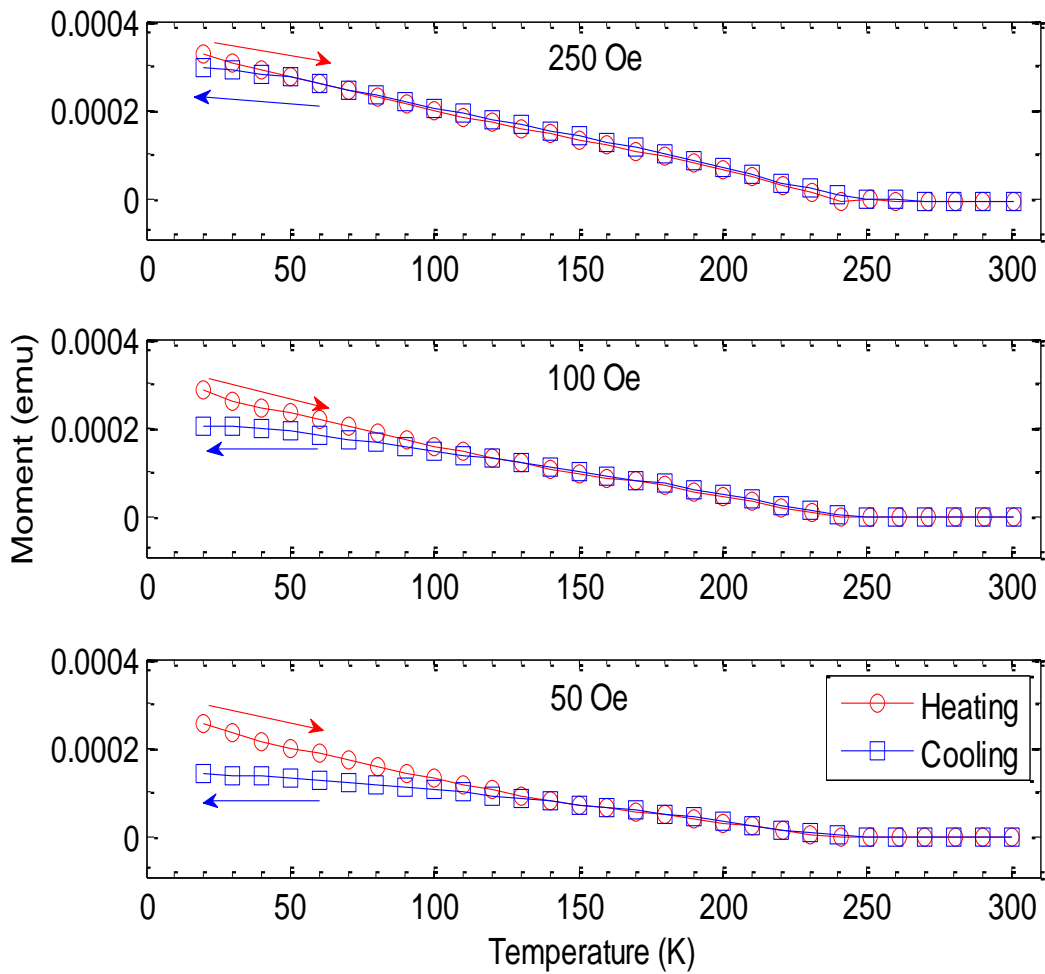
Fig. 5.2 MTH measurements of a 33 layer Gd thin film. Starting at low temperature using constant measuring field. top) 250 Oe; middle) 100 Oe; bottom) 50 Oe
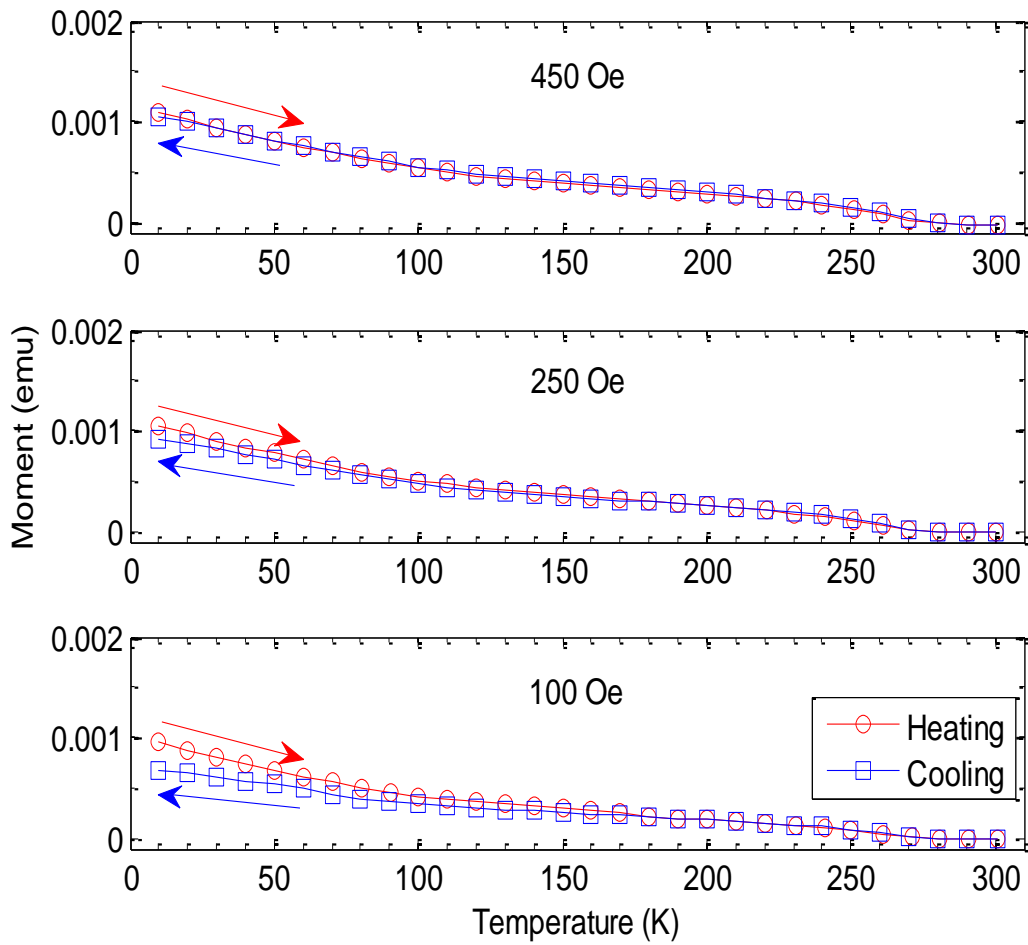
Fig. 5.3 MTH measurements of a 100 layer Gd thin film. Starting at low temperature using constant measuring field. top) 450 Oe; middle) 250 Oe; bottom) 100 Oe
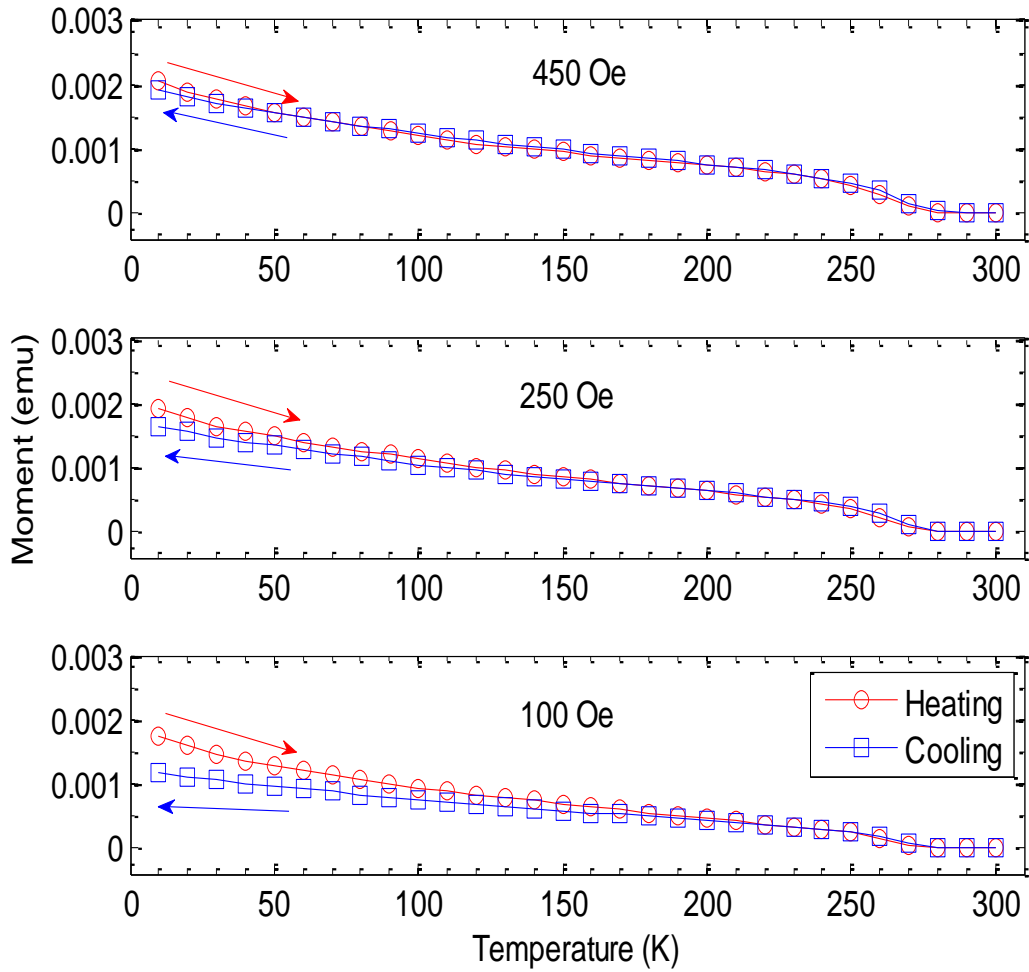
Fig. 5.4 MTH measurements of a 200 layer Gd thin film. Starting at low temperature using constant measuring field. top) 450 Oe; middle) 250 Oe; bottom) 100 Oe
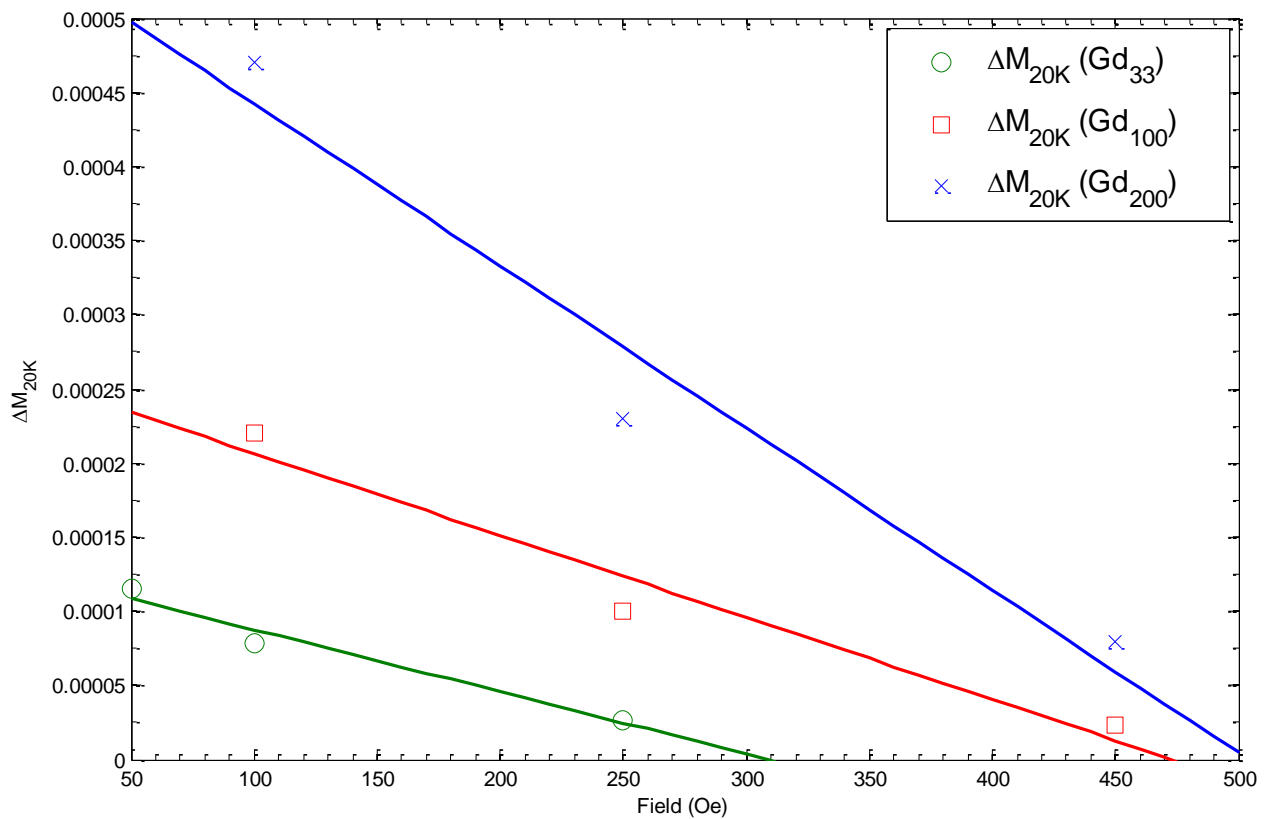
Fig. 5.5 Difference in moment between the heating and cooling branches at 20K for the three Gd films measured as a function of the applied external magnetic field. The lines shown are a linear fit to the data x-axis crossing indicates the approximate external magnetic field value at which magnetic thermal hysteresis will disappear.

Conclusions

In the Gd films it is obvious that there exist MTH. In these films the MTH effect is to much lower extent than seen in the Dy films but is tunable in the same manner i.e. external field strength and sample thickness [3]. Dysprosium, unlike Gd, has a very large temperature dependent anisotropy as seen from the large values of the coercive field in the Dy M(H) curves whereas Gd tends to follow a more reversible path but is still an anisotropy material [68-70] giving it smaller coercive field. Gadolinium is known to have a shifting of its magnetization axis [21, 43, 77] as the temperature is increased. This axis shift repositions the axis of magnetization away from the field direction in a non-symmetric way as the temperature is swept. This has the effect of causing the turn angle of the axes to rotate through different angular amounts as the temperature is increased then decreased. Some of these findings give good physical reasoning to the thermal effects seen in Gd. However, only a small amount of work on pure Gd films is done in temperature sweeps in the forward and reverse paths. The turn angle of the magnetization axis has been calculated/measured but only as a function of increasing T. Taking into account the small amount of anisotropy seen in Gd one can conclude that the observed MTH seen in Gd can be attributed to this turning of the magnetization in a irreversible manner.

The existence of the H and AH states cannot be a contributing factor like they are in Dy. Gadolinium does not contain any known Antiferromagnetic transition region in which these states would exist. Thus currently the only valid explanation would be the temperature

dependent turning of the magnetization axis. The lack of H and AH states in Gd may also be the

reason for the smaller magnitude of MTH seen.

CHAPTER 6

TRI LAYER FILM ANALYSIS

The analysis of the individual materials confirmed that the shape of the thermal hysteresis curves seen in the initial analysis was a coupled effect. The tri layer films show information pertaining to two pronounced transitions relating to both the Dy and Gd transitions (Figs. 6.1 – 6.6). The features seen in the graphs are individual effects. A check of multiple combinations of the layer thicknesses is consistent with the results observed for the individual films. By varying the thickness of the outer or inner layers we recover the information from the remaining material. In other words by decreasing the thickness of the Gd layers we recover the Dy profile and vice versa. Doing this confirms that the MTH results for multilayer system is a cumulative effect of each of the layers. Over the temperature ranges in which these M(T) measurements are done all of the magnetic phases of each material is present. Therefore we should also expect that the magnetic moment and transition temperatures should also depend on the layer thicknesses. It can be seen by a comparison of these figures with the Gd and Dy films that the magnetic moments are additive (Ferromagnetic) and no other coupling (Antiferromagnetic or Ferrimagnetic) exist that give the magnetic thermal hysteresis as seen in other multilayer systems [1-4, 49, 50].

Fig. 6.1 MTH measurements of a $Gd_{100}/Dy_{120}/Gd_{100}$ thin film. Starting at low temperature using constant measuring field. top) 450 Oe; middle) 250 Oe; bottom) 100 Oe
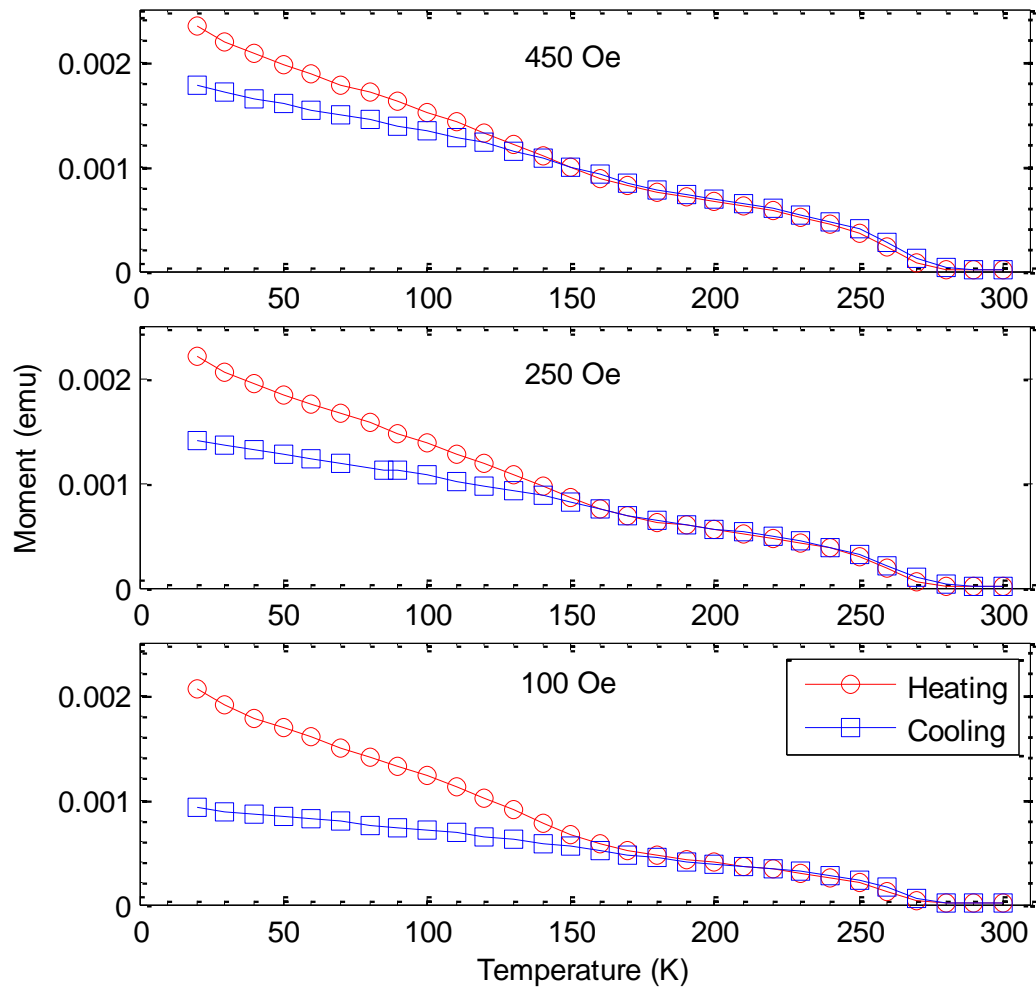
Fig. 6.2 MTH measurements of $Gd_{100}/Dy_{60}/Gd_{100}$ thin film. Starting at low temperature using constant measuring field. top) 450 Oe; middle) 250 Oe; bottom) 100 Oe
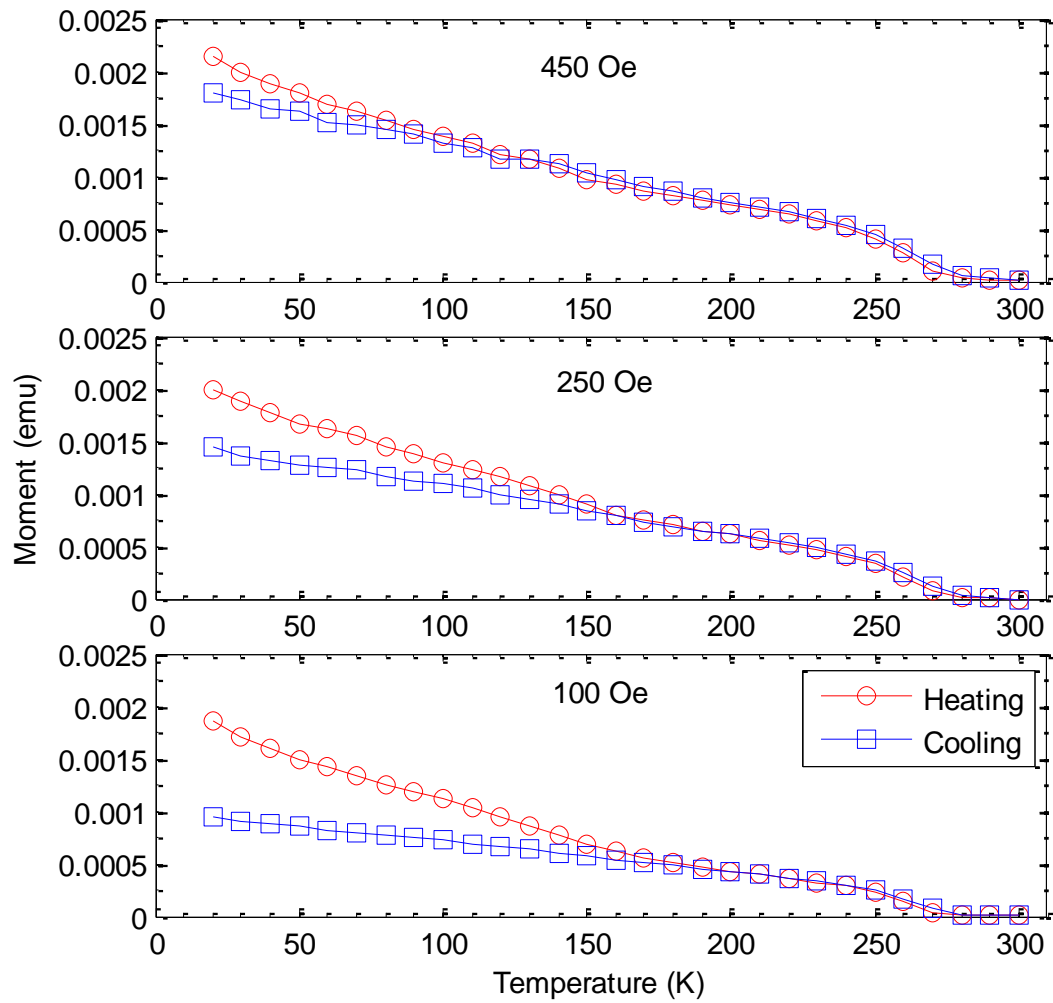
Fig. 6.3 MTH measurements of $Gd_{100}/Dy_{30}/Gd_{100}$ thin film. Starting at low temperature using constant measuring field. top) 450 Oe; middle) 250 Oe; bottom) 100 Oe
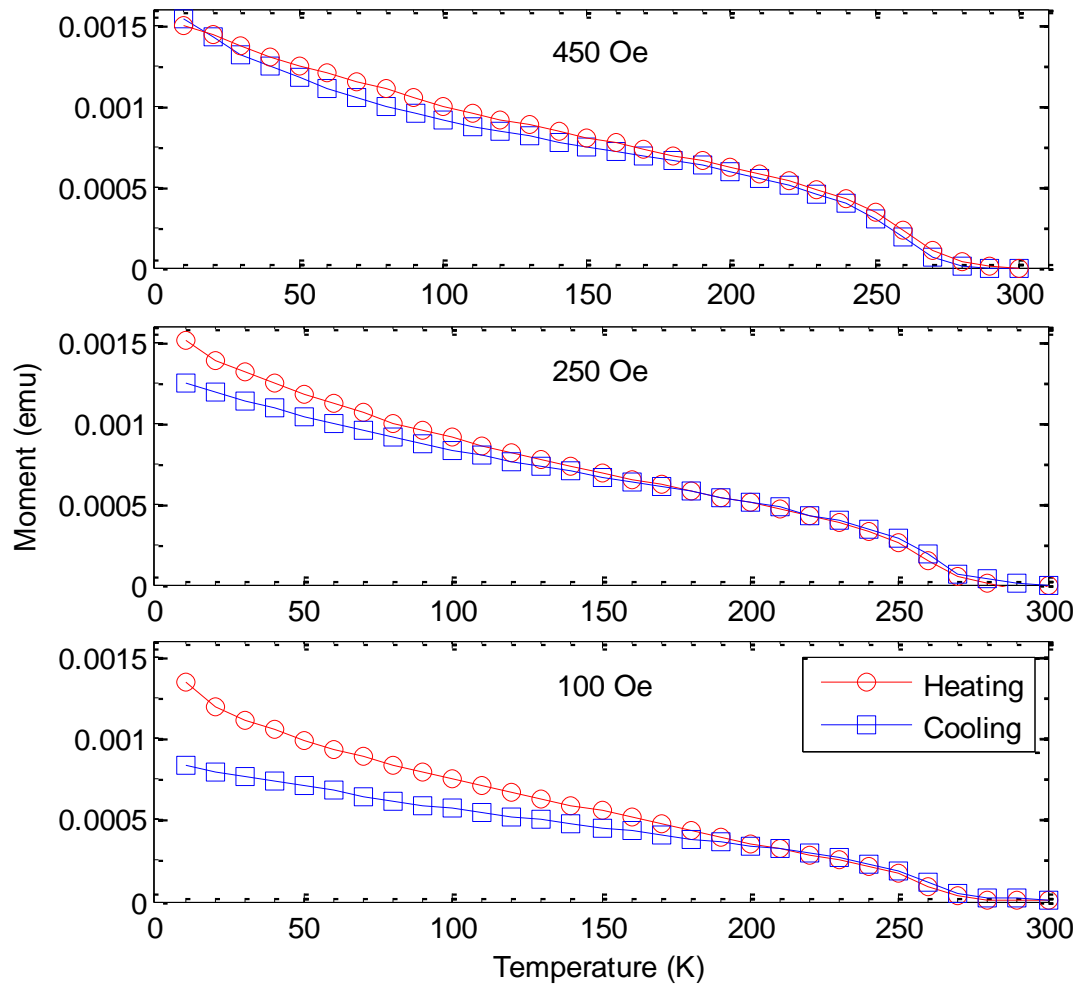
Fig. 6.4 MTH measurements of $Gd_{100}/Dy_8/Gd_{100}$ thin film. Starting at low temperature using constant measuring field. top) 450 Oe; middle) 250 Oe; bottom) 100 Oe
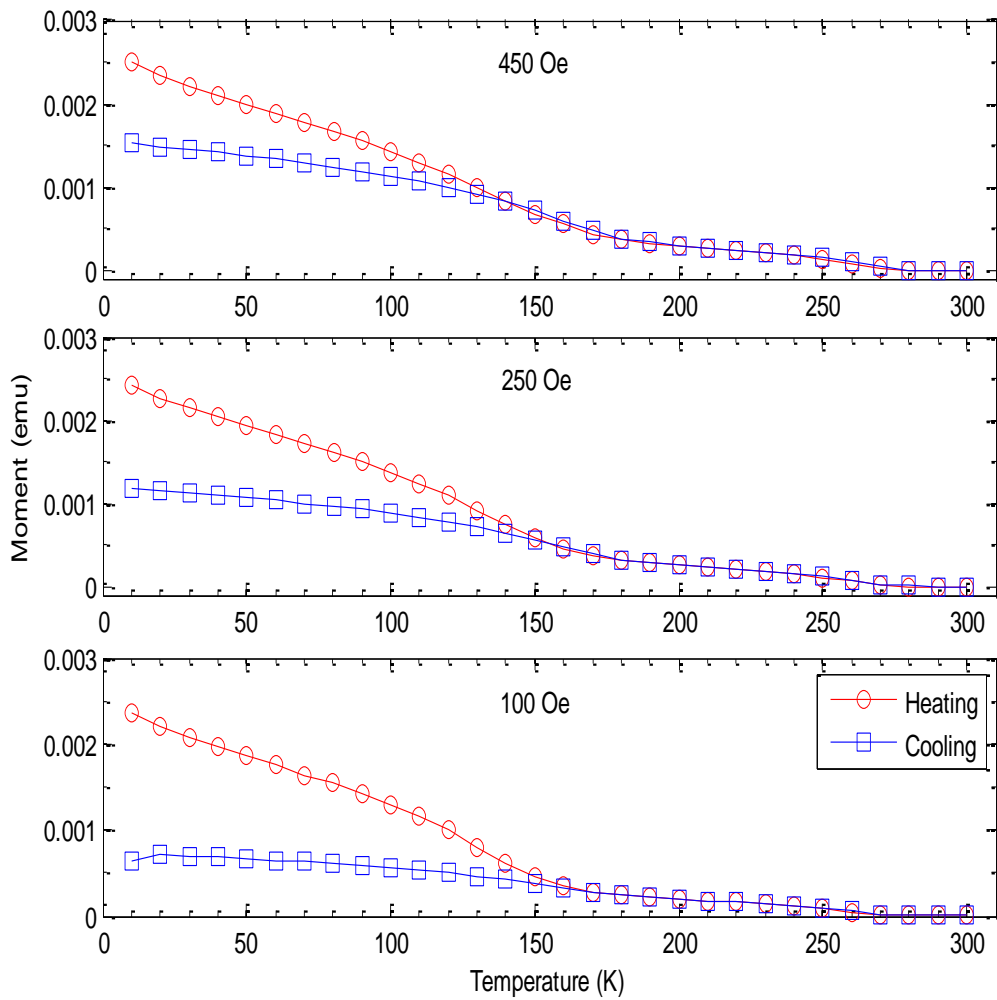
Fig. 6.5 MTH measurements of $Gd_{50}/Dy_{120}/Gd_{50}$ thin film. Starting at low temperature using constant measuring field. top) 450 Oe; middle) 250 Oe; bottom) 100 Oe
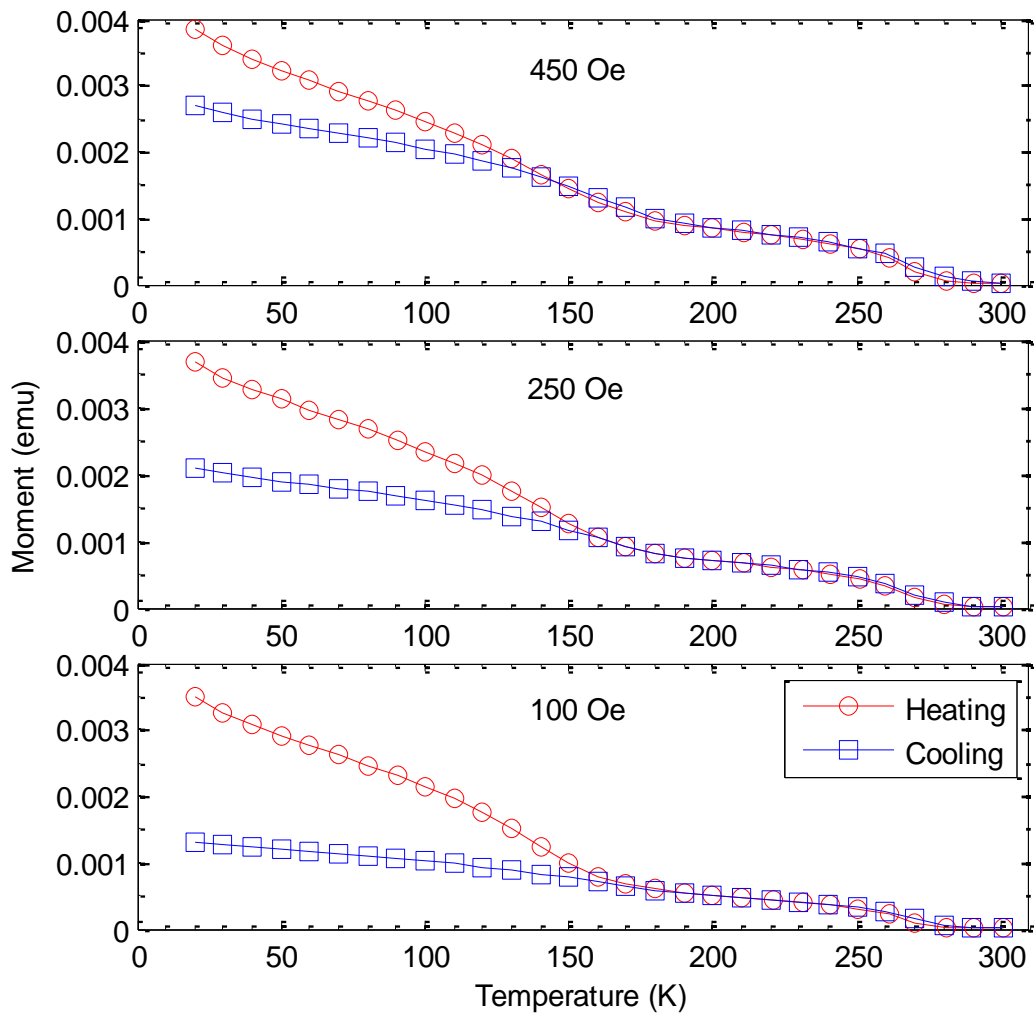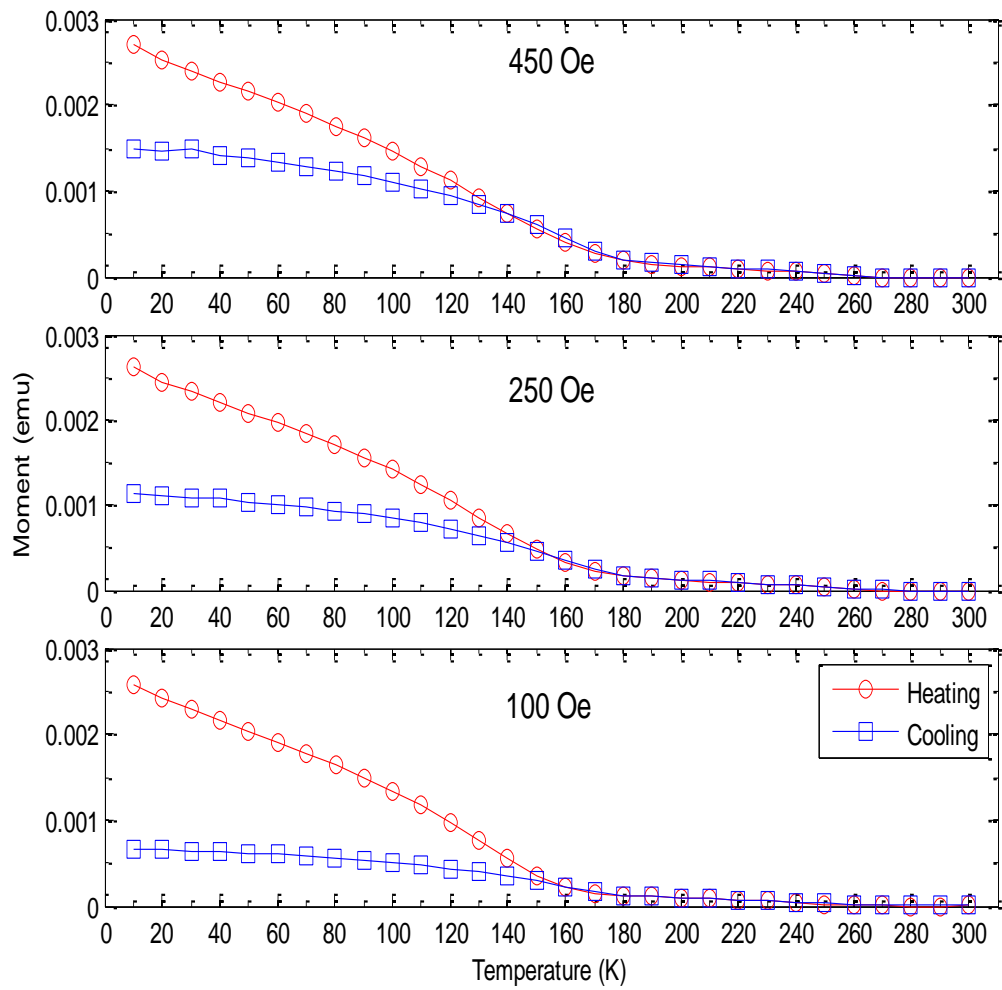
Fig. 6.6 MTH measurements of $Gd_{25}/Dy_{120}/Gd_{25}$ thin film. Starting at low temperature using constant measuring field. top) 450 Oe; middle) 250 Oe; bottom) 100 Oe

Conclusions

In the analysis for each of the thin film samples (Gd and Dy) we have measured the temperature effects on the magnetic moment and saw obvious MTH. The combination of the materials in itself also shows MTH from each of the constituents. Measurements done on a combination of different thicknesses of either Gd or Dy show a correlating effect on the M(T) curves (figures 6.1 – 6.6). Comparing the large sample $Gd_{100}Dy_{120}Gd_{100}$ we see pronounced transitions from Gd and Dy. If the size of the sample layers are modified we should expect to see the effects only in the regions that particular film layer is responsible for. This means that if one were to reduce the inner Dy film thickness then we should recover the Gd behavior. Likewise reducing the outer Gd thickness we can recover the Dy behavior. The reason(s) for the MTH seen in these films is a result of the individual materials as outlined in the previous chapters.

CHAPTER 7

THERMODYNAMIC MEASUREMENTS OF THIN FILMS

Thermodynamic measurements of materials are often very basic measurements if sample materials are large in quantity. Measurements such as energy (heat) transfer are directly related to mass and physical quantities like heat capacity, and entropy.

$$\Delta Q = mC\Delta T$$

However, the current methods that exist for measuring the thermodynamic properties of small scale samples i.e. thin films is either very complicated employing methods of lithography or are very expensive for small labs [67, 82, 83]. Measurements of heat capacity are done easily by methods of calorimetric studies when pertaining to large samples.

Calorimetry

The study or measurement of heat exchange of a material with the surrounding environment is known as calorimetry. Calorimeters are designed to extract and measure the heat exchange of a sample with the surrounding medium. This is done primarily by submerging a sample to be measured in a medium of known mass and thermodynamic properties i.e. heat capacity. Multiple methods exist in which heat can be exchanged, chemical reactions, explosions, direct heat input and magnetic phase change. In chemical reactions exact amounts of

material will produce a calculable amount of products. There are two different types of heat exchange that can occur from these chemical reactions. Endothermic reactions are ones in which the reaction needs to absorb heat in order to go to completion. Exothermic reactions are reactions in which the process releases heat as the reaction goes to completion. In both types of these chemical reactions heat is exchanged with the surrounding environment. The location of these reactions is chosen so as to not interrupt the products of the reaction or to give a medium that accurately and easily gives pertinent information, for instance temperature. In the example reaction below sugar is combusted; the energy released from this reaction (exothermic) is expelled into the surround in medium.

$$C_{12}H_{22}O_{11}(s) + 12\ O_2(g) = 12\ CO_2(g) + 11\ H_2O(l)$$
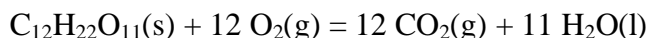
This in turn raises the temperature of the medium (for example air). If the mass and heat capacity of the medium is known the amount of temperature increase is directly related to the heat released in the reaction (see above equation). Similar experiments can be done with materials where no chemical changes take place. By monitoring the heat exchange, by observing the temperature change, between the surrounding environment and the sample material the heat capacity of the sample material can be calculated assuming no loss of heat.

$$Q_{lost} = Q_{gained}$$

For measurements of most solid sample materials, like metals, the temperature changes are not large enough to cause phase changes such as melting or boiling. Under these conditions the

specific heat is a constant quantity referred to at constant volume. Assuming, for example, that there is no phase change of the sample or the environment i.e. the sample or the surroundings do not melt or boil, then the heat transferred between the environment and the sample can be measured using the relationship.

$$m_{sample} C_{sample} (T_i - T_f) = m_{environment} C_{environment} (T_f - T_i)$$

By this method one can see how the heat capacity can be extracted; as stated before this method works well with large size samples and measurable temperature differences. However, if one tries to use similar methods for small scale samples such as the Dy and Gd films this method does not work well. In the magnetic samples; the transition from one magnetic state to another acts as an equivalent method of energy exchange observed in the previous examples. The magnetic samples extract energy (endothermic reaction) from the surrounding environment (magnetic field). Calorimeters in the form of thin films (lithographic masks) or methods like Differential Scanning Calorimetry (DSC) used on thin film samples to determine such properties like heat capacity, entropy change and temperature change [66, 67, 82, 83]. In the method outlined below we seek to determine the relationship between the energy extracted from the magnetic field, combined with thermodynamic results, to find information that is otherwise not easily attainable.

Free Energy

The difficulty and expense of lithography made it a necessity to find an alternative method to measure quantities such as temperature change, entropy change and heat capacity. Using well known results from thermodynamics and statistical mechanics the physical quantities we would hope to measure become easier to obtain. Nearly all of these measurements can be related (in some form) back to the energy of the system. In the case of the magnetic materials one straightforward relationship gives us the stepping stone into our calculations.

It can be shown, for a magnetic system, that the magnetization (moment/volume) of a magnetic system is related to the Gibbs Free Energy by [57]:

$$M = -\left(\frac{\partial G}{\partial H}\right)_T$$

$$G \equiv U - TS + MH$$

Right away we see from rearranging the above equation and integrating with respect to the applied field, in an isolate system, we can extract the relationship for the free energy at some temperature T.

$$G_{T_1} = \int_{B_i}^{B_f} -M dH$$

If this is done repeatedly over a wide temperature range we can gain how the free energy varies as a function of temperature G(T). To accomplish this experimentally, a series of field hysteresis

curves are measured for various samples; 120 layer Dy film, 200 layer Gd film and the three layer film $Gd_{100}/Dy_{120}/Gd_{100}$. For each of the listed samples the temperature ranges were chosen over a range to include the obvious transitions seen in the three layer films. The SQUID was used to make the M(H) measurements. The M(H) measurements are taken from the SQUID and the calculations are done in a Mathematica program (full program in appendix). The program reads the data file which contains information of the magnetic field strength, temperature and moment measured by the SQUID.

Modified Brillouin Function

In order to evaluate the integral that gives us the Gibbs Energy we must have a function of the magnetization (moment). Looking at the Brillouin function there are obvious similarities with our M(H) curves. A slight modification of the original equation gives a much more realistic picture seen in the experiments.

$$B_J(x) = \frac{2J+1}{2J} Coth\left(\frac{2J+1}{2J}x\right) - \frac{1}{2J} Coth\left(\frac{x}{2J}\right)$$

Using the original equation plots are made to show how the function behaves for some arbitrary values (Fig. 7.1).
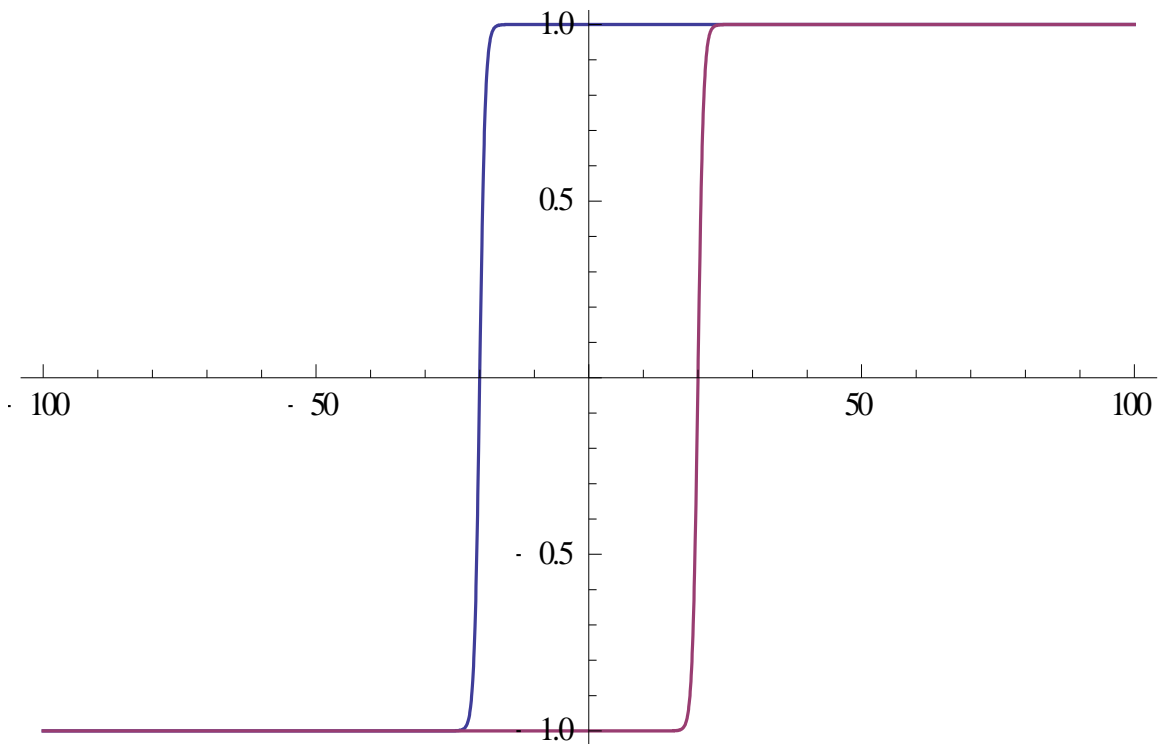
Fig. 7.1 Plot of the Brillouin function for J = 1/2

If the function is however slightly modified we can see a more accurate representation of the

experimental results (Fig. 7.2).

$$B_{mod}(x) = a\left(Coth\left(\frac{x+c}{b}\right) - \frac{b}{x+c}\right)$$

The modified function is very similar in looks to the Langevin Function. This was determined

from test runs that the values of J necessary for the function to reproduce the data, the value of J

in the Brillouin function must be very large i.e. $J \to \infty$ this limiting case results in the Langevin function (appendix A).
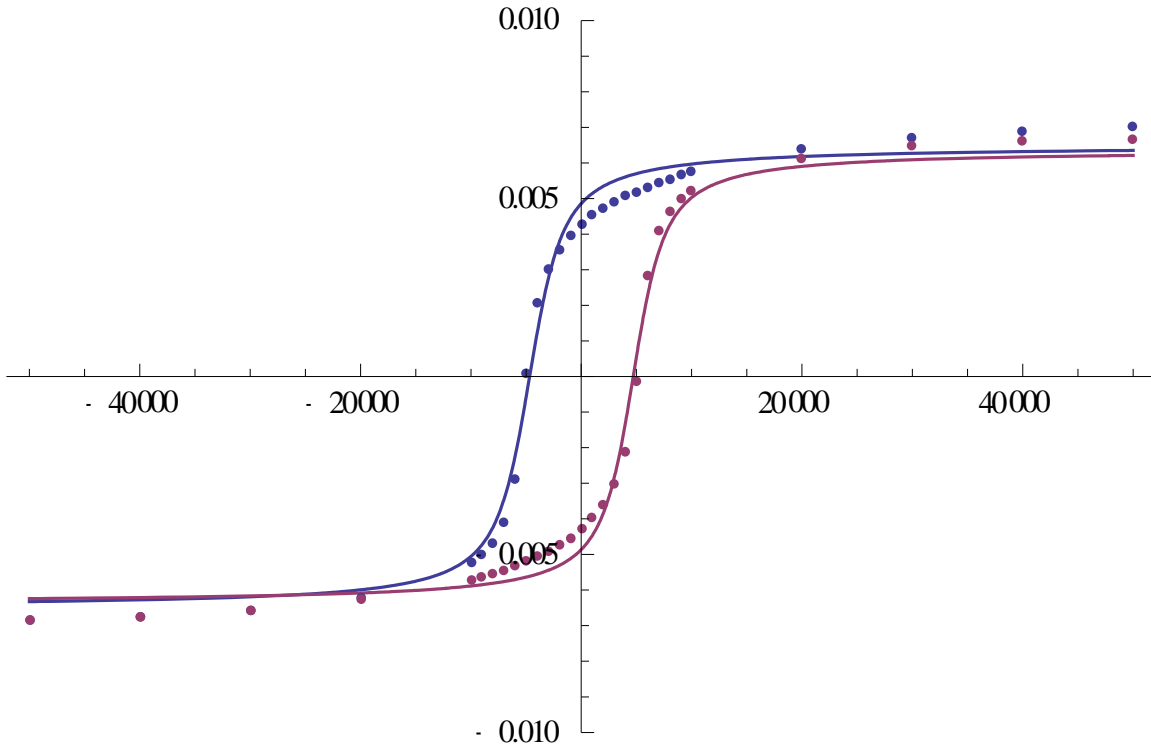
Fig. 7.2 Plot of the experimental data (Dy_{120} @30K) along with the B_{mod} function (line) to show the attempted fit of the function with the data.

Reconstructing the M(H) curves from the data set, the program cycles through each temperature reading and finds the parameters a, b and c that give the best fit of the data with the function, a few examples of the resulting curves are given below (Figs. 7.3 – 7.5).
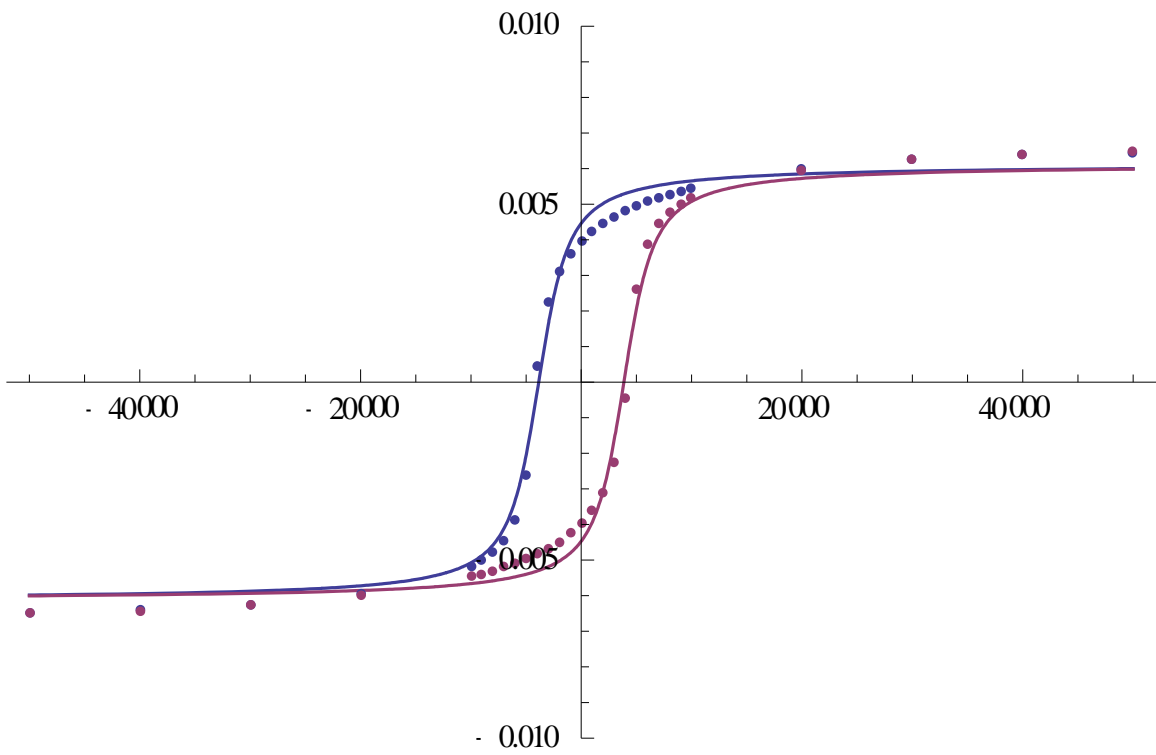
Fig. 7.3 Plot of the experimental data (Dy$_{120}$ @40K) along with the B$_{mod}$ function (line) to show the attempted fit of the function with the data.
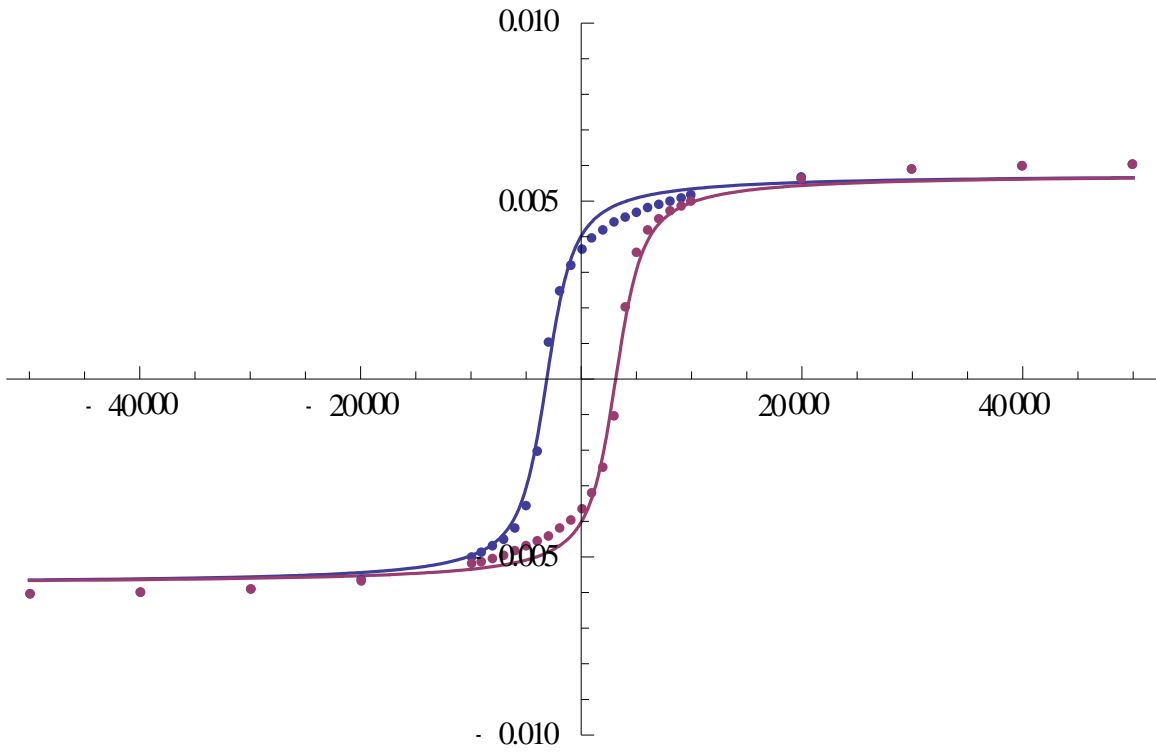
Fig. 7.4 Plot of the experimental data (Dy$_{120}$ @50K) along with the B$_{mod}$ function (line) to show the attempted fit of the function with the data.
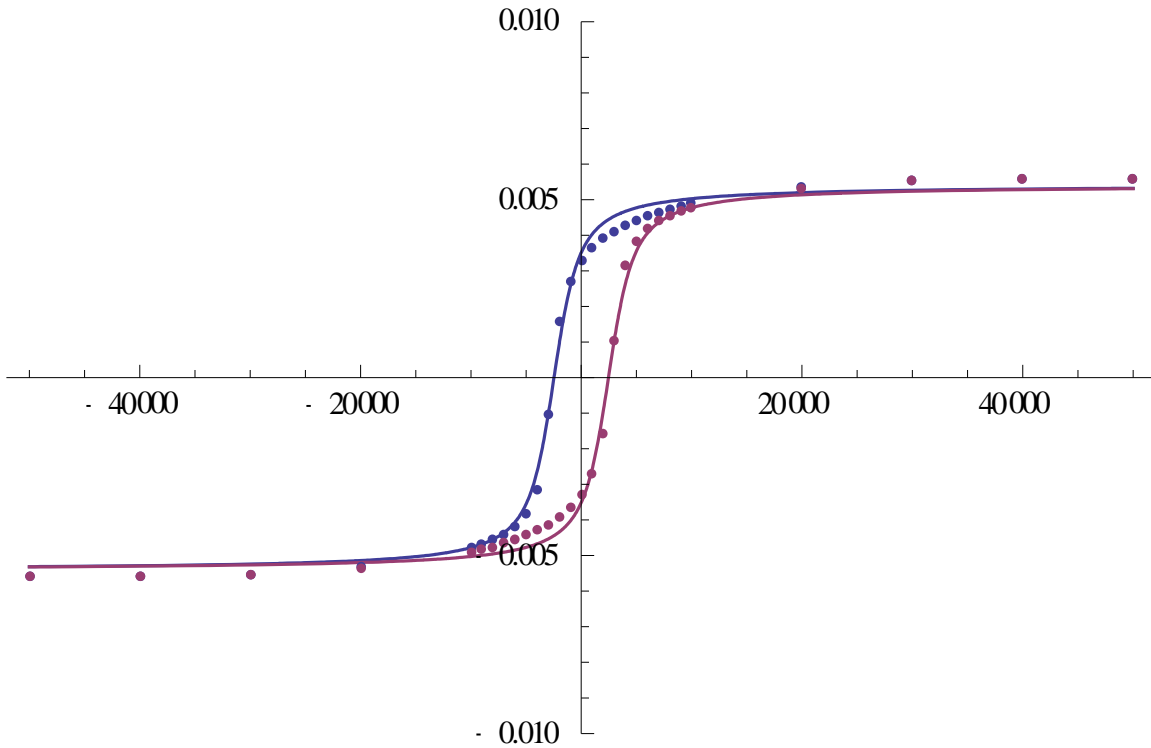
Fig. 7.5 Plot of the experimental data (Dy$_{120}$ @60K) along with the B$_{mod}$ function (line) to show the attempted fit of the function with the data.

The final steps involve calculating the area contained between the upper and lower curves. This area is the result of the Free Energy integral and gives us the points necessary to make our G(T) graph. If the width of the area is not the full area but a fraction we can also obtain how G also varies with H.

$$G(T, H_f) = G(T, H_i) - \mu_0 \int_{H_i}^{H_f} M dH$$

CHAPTER 8

FREE ENERGY, ENTROPY AND MAGNETIC HEAT CAPACITY

MEASUREMENTS OF DY, GD AND $GD_{100}DY_{120}GD_{100}$ THIN FILMS

The analysis of the field hysteresis curves leads to the temperature dependence of the free

energy. Knowing how the Free Energy of the system depends on the temperature allows one to

easily derive the other measurements of Entropy change and Magnetic Heat Capacity. From the

given relationship between the internal energy and the free energy of the system, these properties

can be extracted [57, 91].

$$U = \frac{\partial(\beta G)}{\partial \beta}$$

$$\beta = \frac{1}{kT}$$

Expanding these relationships we obtain:

$$U = G\frac{\partial \beta}{\partial \beta} + \beta\frac{\partial G}{\partial \beta}$$

$$\partial \beta = -\frac{1}{kT^2}\partial T$$

Making this substitution leads to the following result.

$$U = G - T\frac{\partial G}{\partial T}$$

Comparison of this with the known form of the Gibbs free energy function [52, 55, 63] for a system gives the form of the Entropy function. The analysis of the Gibbs free energy for a magnetic system requires a further transformation of internal energy function [57].

$$U = G + TS + MH$$

$$S = -\frac{\partial G}{\partial T}$$

From the Internal energy relationship the magnetic heat capacity can be extracted.

From the internal energy:

$$C_H = \frac{\partial U}{\partial T} = \frac{\partial G}{\partial T} - \frac{\partial T}{\partial T}\frac{\partial G}{\partial T} - T\frac{\partial^2 G}{\partial T^2} = -T\frac{\partial^2 G}{\partial T^2}$$

$$C_M = B\frac{\partial M}{\partial T}$$

$$\frac{\partial U}{\partial T} = C_H + C_M$$

Further examination into this relationship has been shown [28] that the heat capacity at constant magnetization C_M is identically zero and therefore we obtain for the magnetic heat capacity C_H:

$$C_H = -T \frac{\partial^2 G}{\partial T^2}$$

The previous equations and experimental procedures outlined above give the steps necessary to evaluate the Free Energy of the system.

Free Energy, Entropy and Magnetic Heat Capacity

1.) The data points are graphed and fitted to a function (curve fitting done using Mathematica) (Fig. 8.1 – 8.3)

2.) The fitted function and the thermodynamic relationships (Eqs) are used to calculate the remaining thermodynamic properties of Entropy and Mag. Heat Capacity (Figs. 8.4 – 8.9)
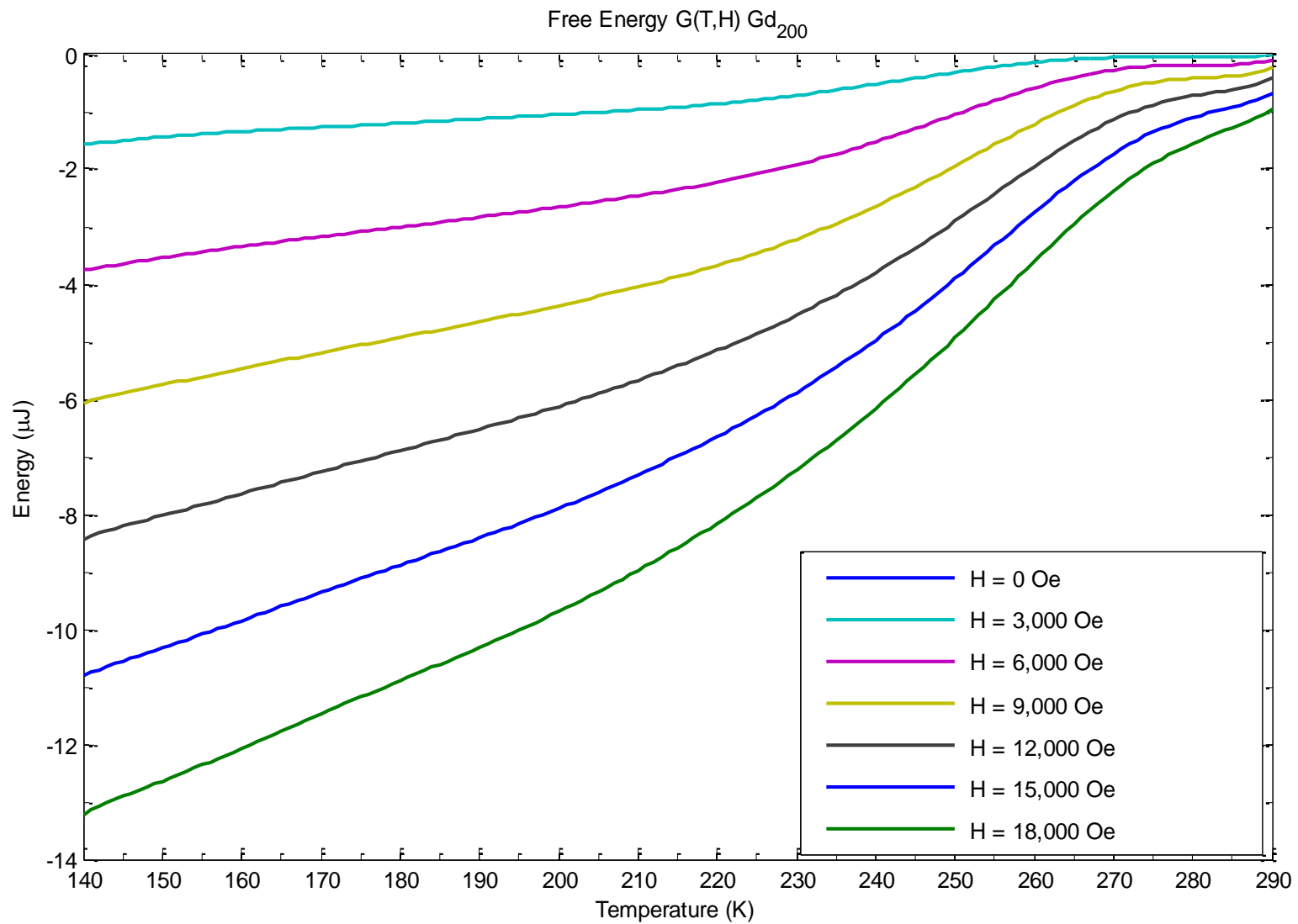
Fig. 8.1 Measurement of the Gibbs Free Energy at different field strengths vs. Temperature for a 200 layer Gd film.
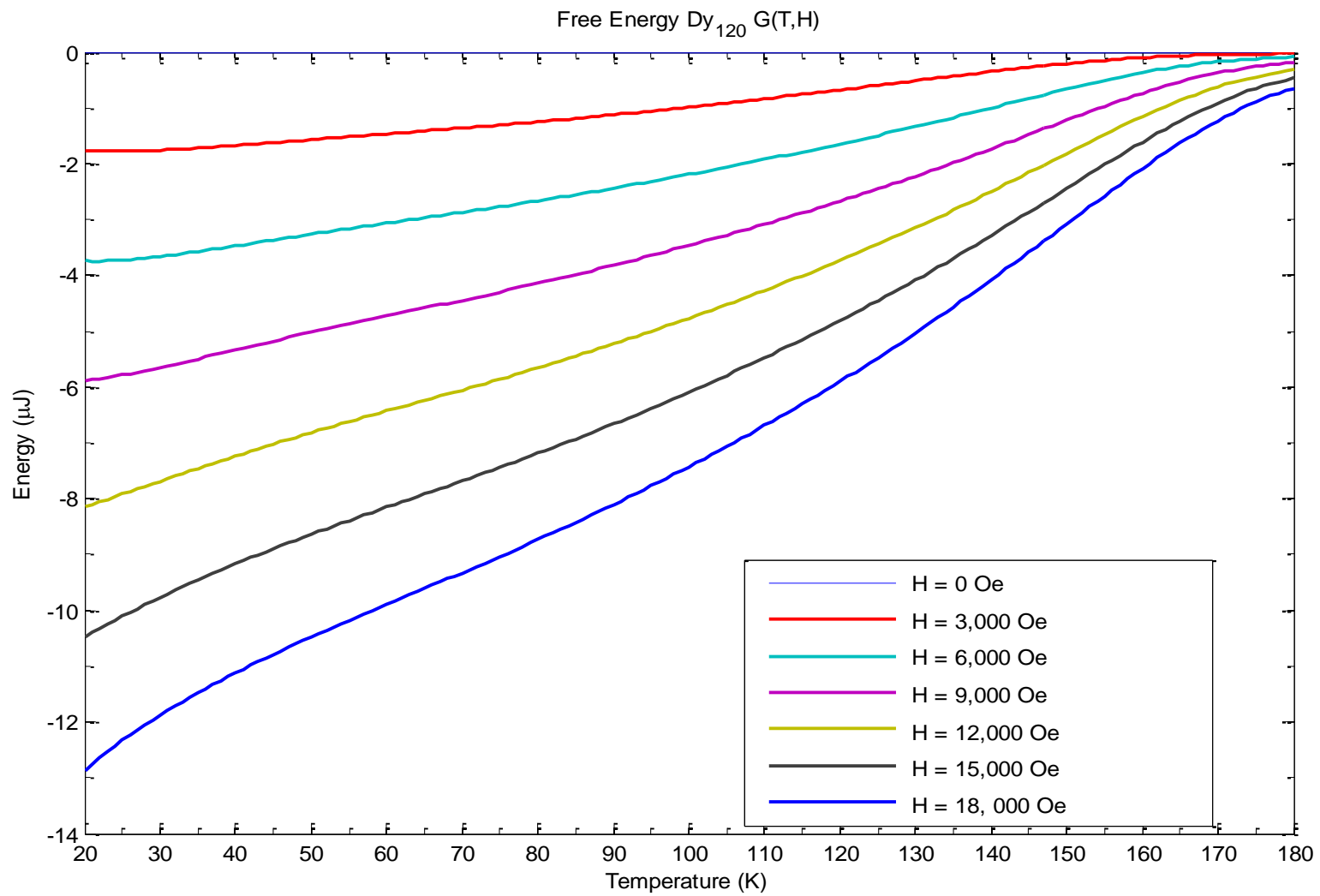
Fig. 8.2 Measurement of the Gibbs Free Energy at different field strengths vs. Temperature for a 120 layer Dy film.
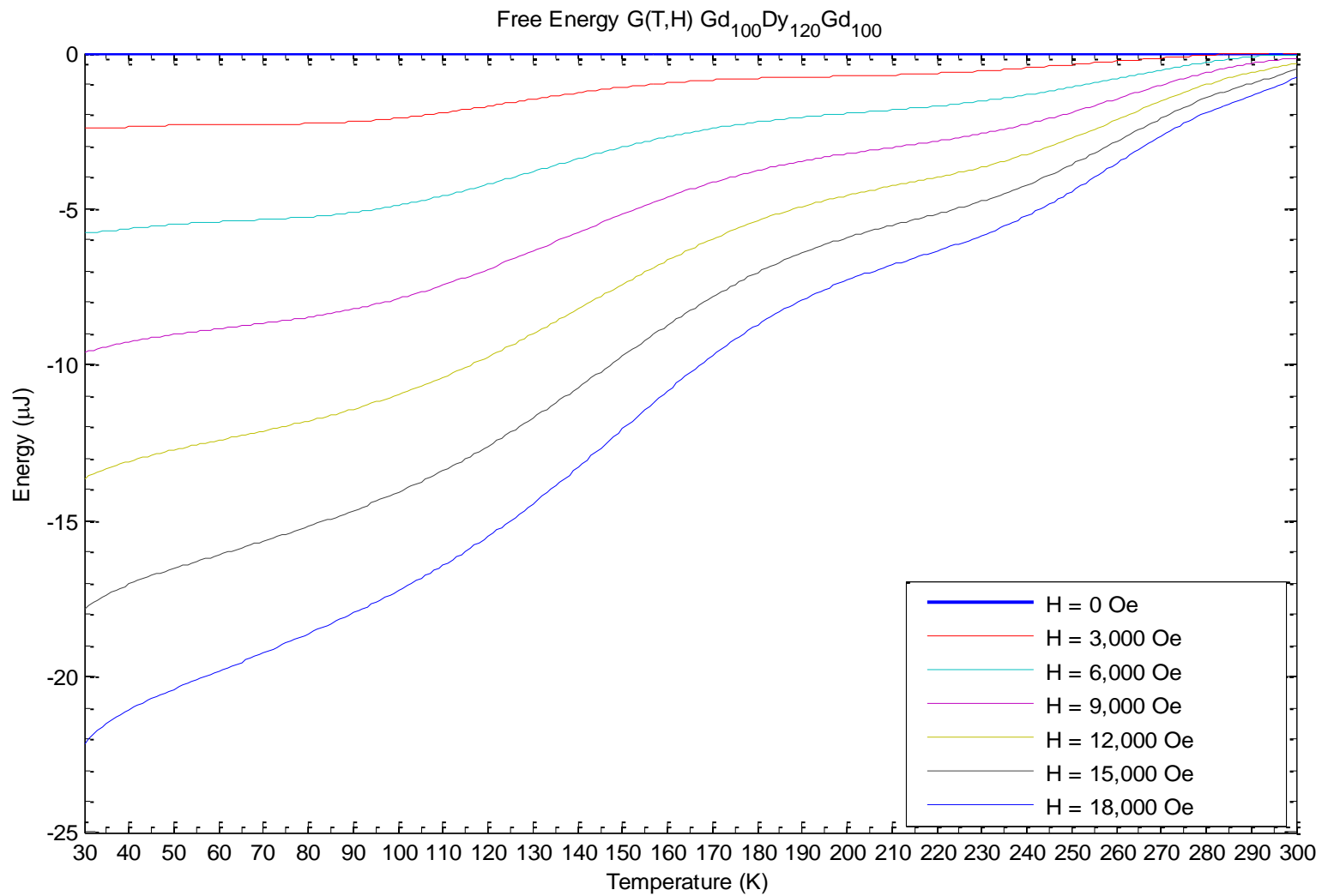
Fig. 8.3 Measurement of the Gibbs Free Energy at different field strengths vs. Temperature for the $Gd_{100}/Dy_{120}/Gd_{100}$ film.
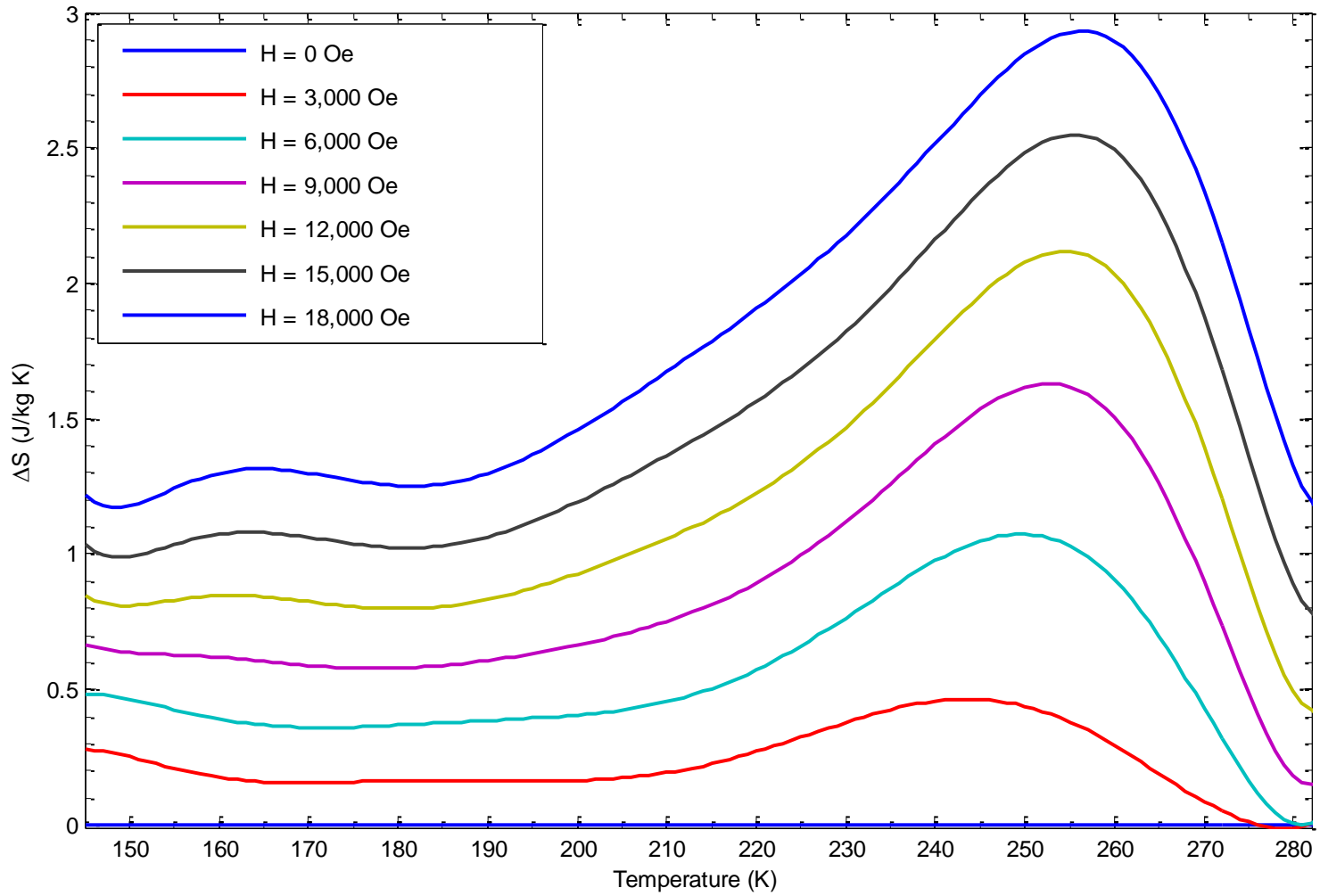
Fig. 8.4 Measurement of the Entropy change at different field strengths vs. Temperature for a 200 layer Gd film calculated from the Free Energy function.
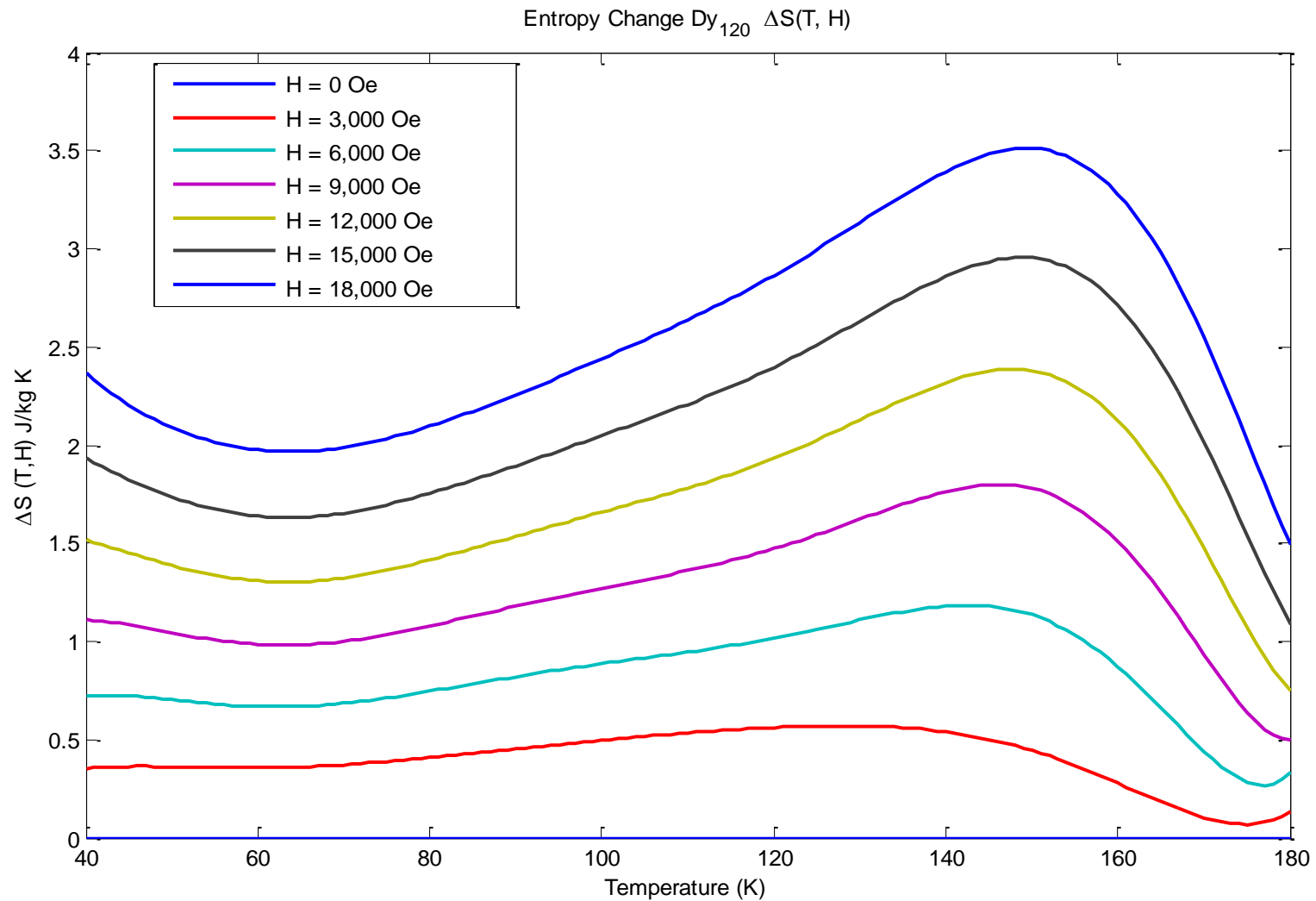
Fig. 8.5 Measurement of the Entropy change at different field strengths vs. Temperature for a 120 layer Dy film calculated from the Free Energy function.

Fig. 8.6 Measurement of the Entropy change at different field strengths vs. Temperature for the $Gd_{100}/Dy_{120}/Gd_{100}$ film calculated from the Free Energy function.

Fig. 8.7 Measurement of the Magnetic Heat Capacity (C_H) at different field strengths vs. Temperature for a 200 layer Gd film calculated from the Free Energy function.
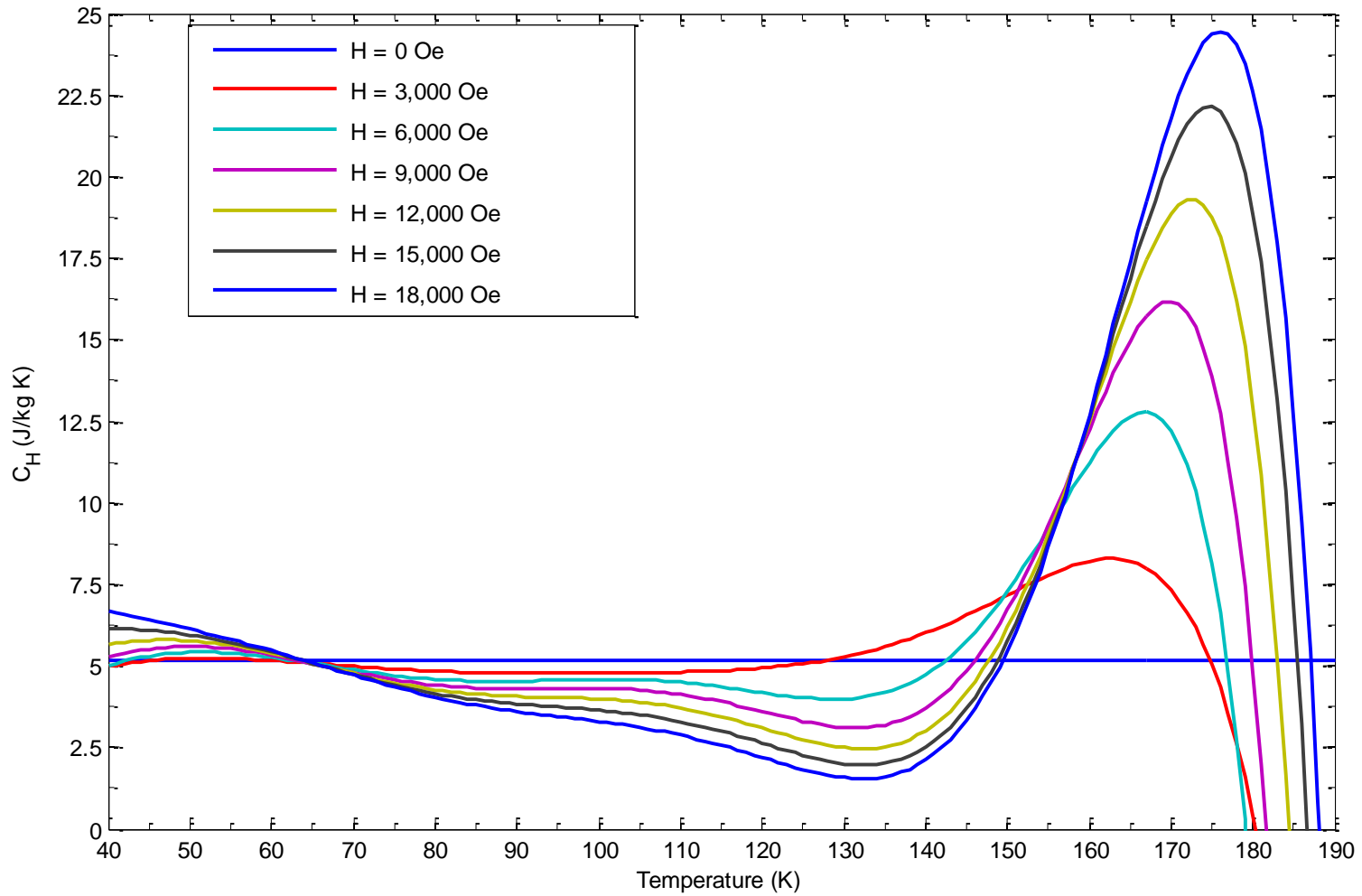
Fig. 8.8 Measurement of the Magnetic Heat Capacity (C_H) at different field strengths vs. Temperature for a 120 layer Dy film calculated from the Free Energy function.

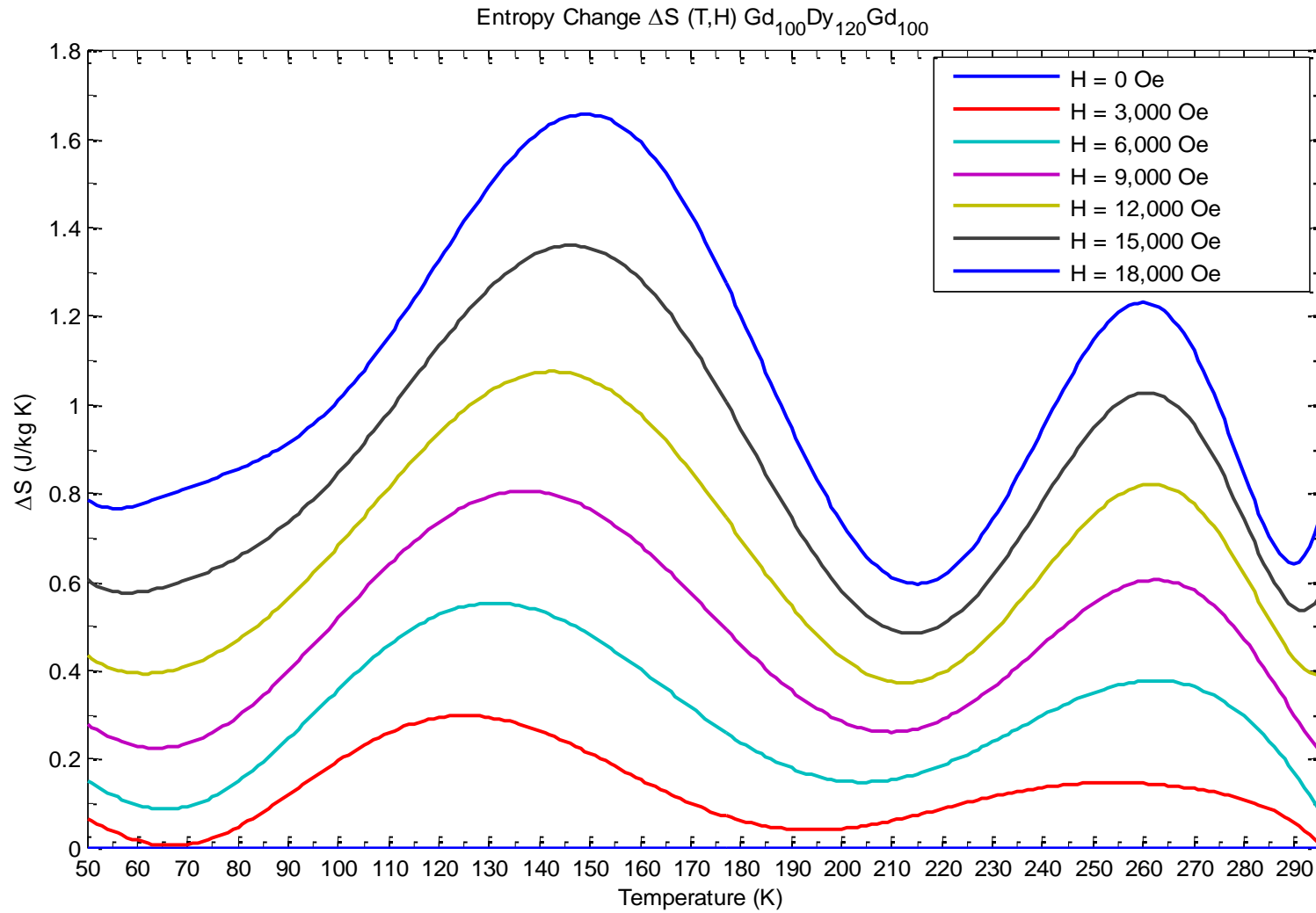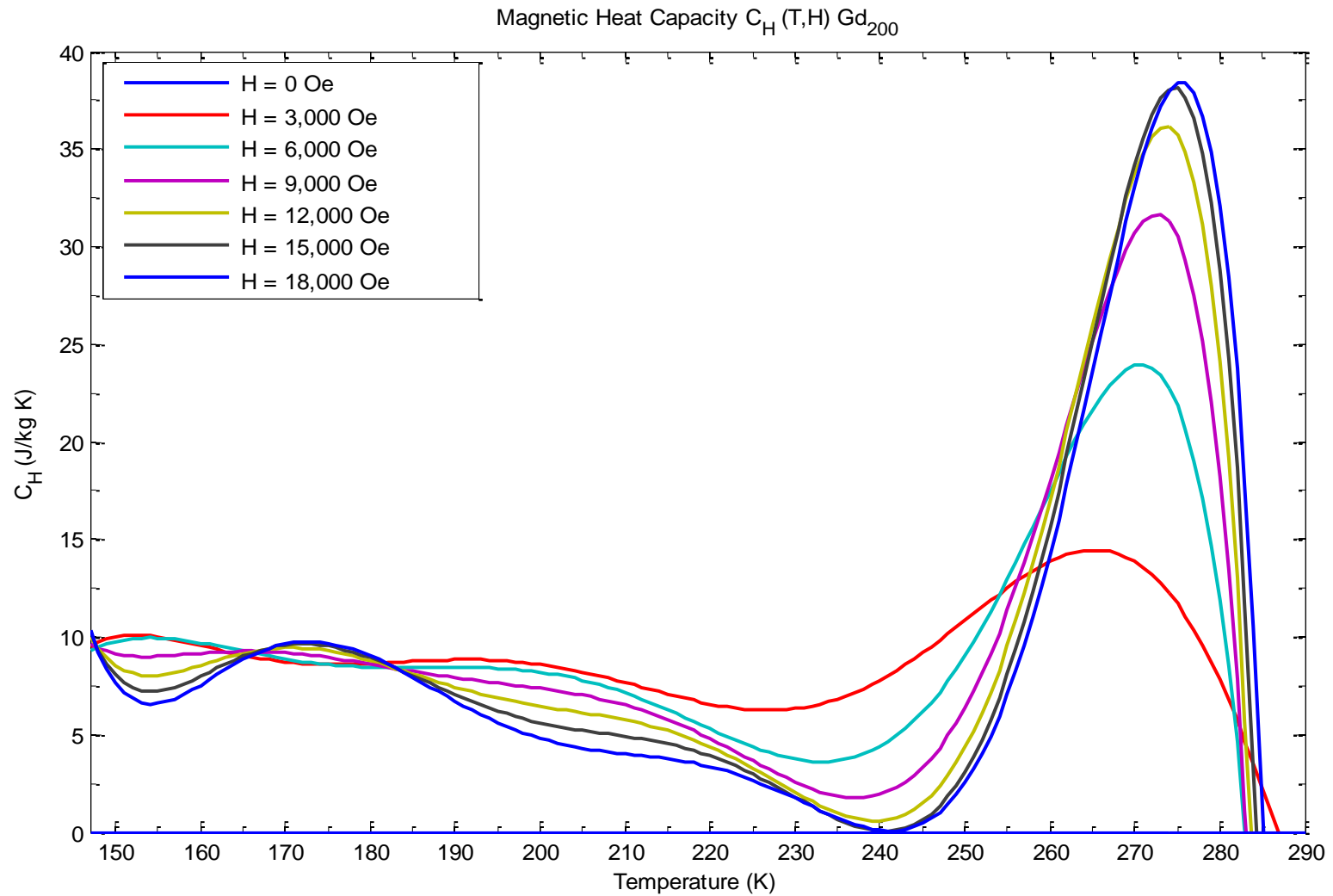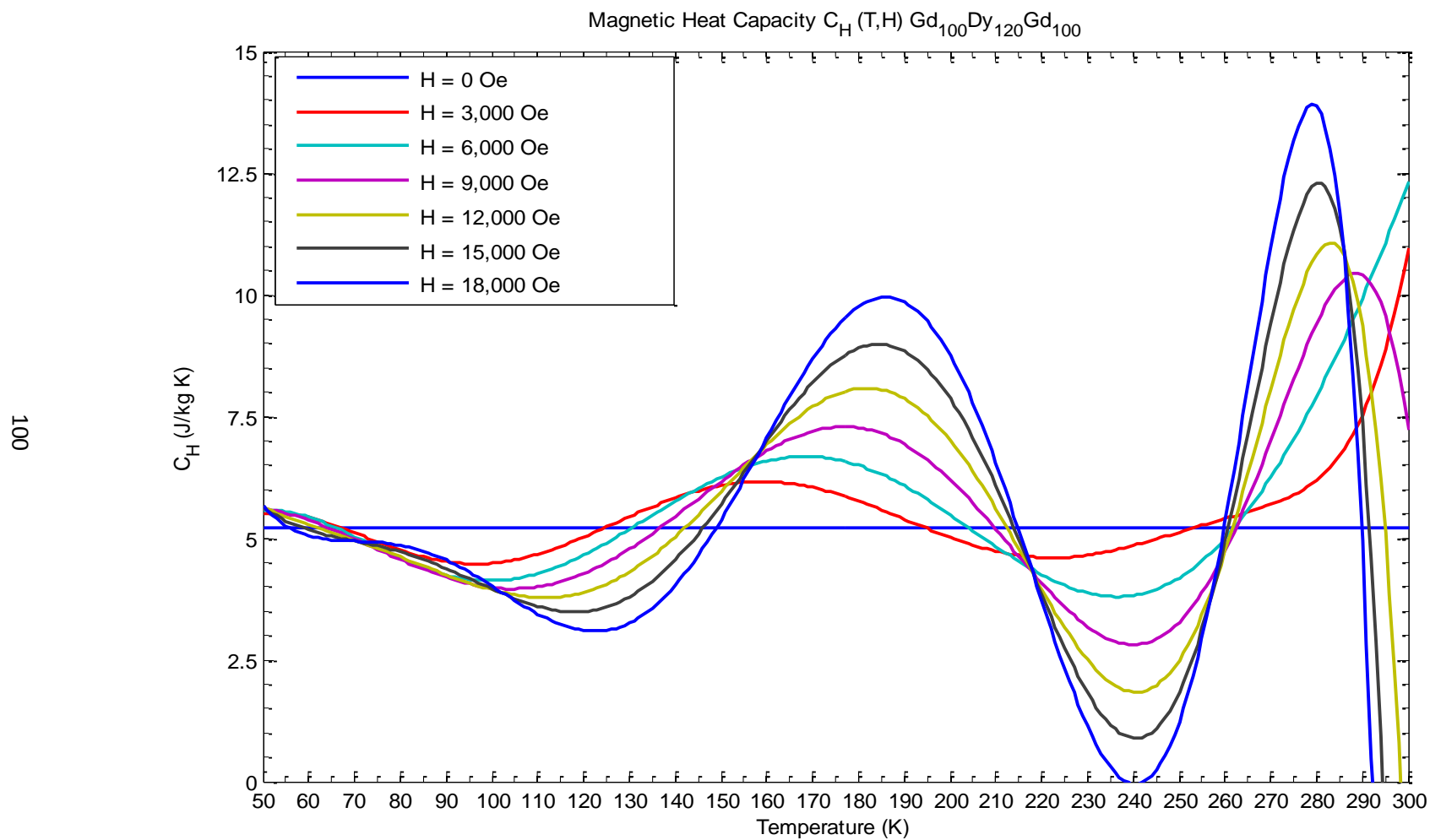Fig. 8.9 Measurement of the Magnetic Heat Capacity (C_H) at different field strengths vs. Temperature for the Gd_{100}/Dy_{120}/Gd_{100} film calculated from the Free Energy function.

Results

Thermodynamic properties of the Dy_{120}, Gd_{200} and $Gd_{100}Dy_{120}Gd_{100}$ were investigated using Maxwell's relationships for the Gibbs free energy. Other methods have been used for the Magneto Caloric Effect (MCE) measurements [2, 67, 89, 90] to determine thermodynamic properties such as Entropy change and Heat Capacity. Here by using a series of M(H) field hysteresis curves we are able to evaluate the value of the function G at various temperatures; and by the Maxwell relationships determine Entropy change (ΔS) and Heat Capacity (C_H). The analysis of the G(T) curve lead to the calculations of the entropy change and heat capacity measurements. The transition peaks seen from these curves are consistent with magnetic phase transitions such as:

1.) Antiferromagnetic to Paramagnetic transition (Dy)
2.) Ferromagnetic to Paramagnetic transition (Gd)

Further investigation into these phase transitions using other methods need to be done to verify the quantitative results seen here. However, a qualitative analysis shows that the calculations are consistent with expectation. Although there are regions in which the heat capacity leads to non ideal physical behavior. In other words analysis on the G(T) data leads to regions of the second derivative (C_H) becoming negative. There is no evidence to suggest that this is not a real effect and more analysis using this method needs to be done to verify this potentially real anomaly.

Comparable methods of calculation involve determining Entropy change and Heat Capacity from the M(T) curves.

$$\Delta S = -\int \left(\frac{\partial M}{\partial T}\right)_H dH$$

From further investigation into this function one can verify that this analysis leads to the same

results as G(T).

APPENDIX A

MATHEMATICA PROGRAM FOR THERMODYNAMIC ANALYSIS

The analysis of the thin film curves was done with the help of a curve fitting algorithm written using Mathematica. The steps of the program code are outlined as follows. Program comments are omitted to shorten the document but the lines of code referred to in this document are included in the text as a follow along reference. Example graphs and outputs of the code are included to assist the reader.

Mathematica Sequence

Line one of the notebook requests from the user to indicate the file path that contains the field hysteresis data obtained from the SQUID (Fig. A.1). The file needs to be in the following format [field, temp, moment]. Excel can be used to open the data file from the SQUID and the relevant data columns can be extracted.

The main program (Figure) sorts the data based on the temperature value the user chooses (T_{end}). This data is then sorted into two curves; an upper and lower curve. The upper curve is the field sweep from H_{max} to -H_{max} and the lower curve is from -H_{max} to H_{max}.

Select file directory

```
{FileNameSetter[Dynamic[f]], Dynamic[f]}
```

{ Browse... , f}

Fig. A.1 Beginning line of Mathematica program that allows the user to select the file path containing the field hysteresis data.

```
EnergyEntropyC[Tend_, f_] :=
  Module[{i, Et, fitpu, fitpl, curveu, curvel, Lu = {}, Ll = {}, Data, Energy, Dim},
      Data = Import[f, "Table"];
         Energy = Extract[Extract[Take[Data], {#1}], {#2}] &;
           Dim = Extract[Pick[Dimensions[Take[Data, All, -1]], {1, 0}, 1], {1}];
```

$$\text{For}\left[i = \left(\frac{\text{Tend} - \text{Round}[\text{Energy}[1, 2]]}{10} \ 57 + 1\right), i < \frac{1 + 57\left(1 + \left(\frac{\text{Tend}-\text{Round}[\text{Energy}[1,2]]}{5}\right)\right)}{2} + 1,\right.$$

```
  i++, Lu = AppendTo[Lu, {Energy[i, 1], Energy[i, 3]}]];
```

$$\text{For}\left[i = \frac{1 + 57\left(1 + \left(\frac{\text{Tend}-\text{Round}[\text{Energy}[1,2]]}{5}\right)\right)}{2}, i \leq \frac{\text{Tend} - \text{Round}[\text{Energy}[1, 2]]}{10} \ 57 + 57,\right.$$

```
  i++, Ll = AppendTo[Ll, {Energy[i, 1], Energy[i, 3]}]];
```

Fig. A.2 Subroutine of the program which separates the field hysteresis data based on the selected temperature T_{end}

Based on the fitting function:

$$a\left(Coth\left(\frac{x+c}{b}\right) - \frac{b}{x+c}\right)$$

The parameters of (a, b, c) are determined (Figure). The function used in the fitting of the M(H) curves is the Langevin function not the Brillouin function as discussed early. The use of the Langevin function comes out of doing the analysis on the data. The actual "modified" Brillouin function can be used as a fitting function but one finds that the value of J that is determined puts this function near the limit of $J \rightarrow \infty$ which is the limiting case of the Brillouin function. The choice of using the Langevin as opposed to the modified Brilluoin function is preference due to the fact that it is computationally faster.

$$\lim_{J \to \infty} B_J(x) = L(x)$$

After the program evaluates the best values of the parameters to fit the upper and lower curves,

(Fig. A.3) these values are used to describe the function and the necessary calculations are made.

This calculated value is the output of the main program along with its respective temperature.

```
fitpu = FindFit[Lu, a (Coth[(x + c)/b] - b/(x + c)), {a, b, c}, x];
curveu = a (Coth[(x + c)/b] - b/(x + c)) /. fitpu;
fitpl = FindFit[Ll, a (Coth[(x + c)/b] - b/(x + c)), {a, b, c}, x];
curvel = a (Coth[(x + c)/b] - b/(x + c)) /. fitpl;
    Et = -NIntegrate[curveu, {x, 0, 20 000}, MaxRecursion → 6];
{Tend, Et}
```

Fig. A.3 Program section which fits the experimental data to the modified function.

If this process is iterated the value of the area (G) for each temperature can be calculated.

This data set is plotted and fitted to a function, this does not need to be done but the fitted

function is in general much smoother and gives smoother curves in the derivatives. A way

around this is by making the initial M(H) at much smaller temperature steps i.e. 1K. This gives a

much larger dataset which will give a smoother curve for G(T) allowing for direct numerical

analysis. An example of the program output is given below (Fig. A.4).
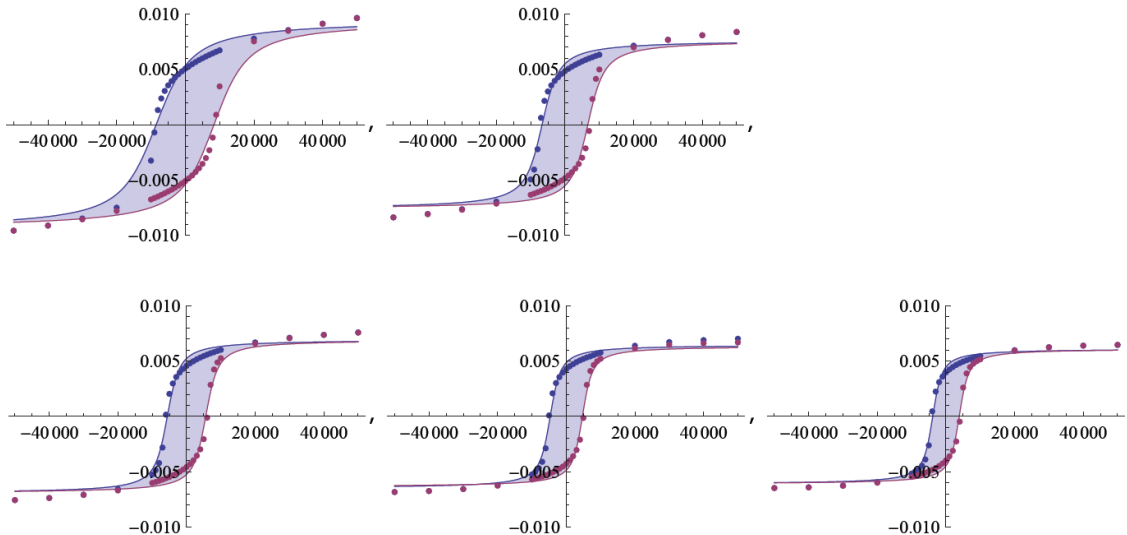
Fig. A.4 Sample dataset of the main program output. The shaded region represents the free energy value at the respective temperature.

{20, -145.023}, {21, -143.357}, {22, -141.853}, {23, -140.482}, {24, -139.217},
{25, -138.039}, {26, -136.928}, {27, -135.872}, {28, -134.86}, {29, -133.882},
{30, -132.931}, {31, -132.004}, {32, -131.096}, {33, -130.204}, {34, -129.326},
{35, -128.463}, {36, -127.613}, {37, -126.776}, {38, -125.952}, {39, -125.141},
{40, -124.344}, {41, -123.56}, {42, -122.791}, {43, -122.035}, {44, -121.294},
{45, -120.565}, {46, -119.85}, {47, -119.147}, {48, -118.456}, {49, -117.775},
{50, -117.105}, {51, -116.443}, {52, -115.789}, {53, -115.141}, {54, -114.498},
{55, -113.86}, {56, -113.225}, {57, -112.591}, {58, -111.959}, {59, -111.326},
{60, -110.693}, {61, -110.055}, {62, -109.415}, {63, -108.774}, {64, -108.132},

Fig. A.5 Calculated values of the free energy plots {T, G}

APPENDIX B

LABVIEW CONTROL PROGRAM FOR LAKESHORE 4500 VSM

VSM Lab Setup

In the analysis of thin film or bulk samples a quick and low cost method of measurement is the use of the Vibrating Sample Magnetometer (VSM). The setup of the VSM in the lab is a LakeShore cryotronics 4300 VSM with a LakeShore 487 magnet power supply. Other components include a temperature controller (LakeShore 340), cryostat and a high sensitivity voltmeter (Keithley).

A Labview program was written in order to replace the VSM controller software originally installed on the computer that shipped with the machine. After its failure (hard drive malfunction) attempts to re-install the code on a newer machine were futile. Thus an alternative solution was necessary. The VSM controller and magnet power supply are still functional but require an external circuit (Fig. B.1) to control the input voltage signals and to read the output signals (magnetic moment) from the VSM controller. Thee magnets of the VSM are rated at a strength of 10,000 Oe but collecting data from the Oersted monitor of the VSM the actual strength is only observed to max at about 9,000 Oe.
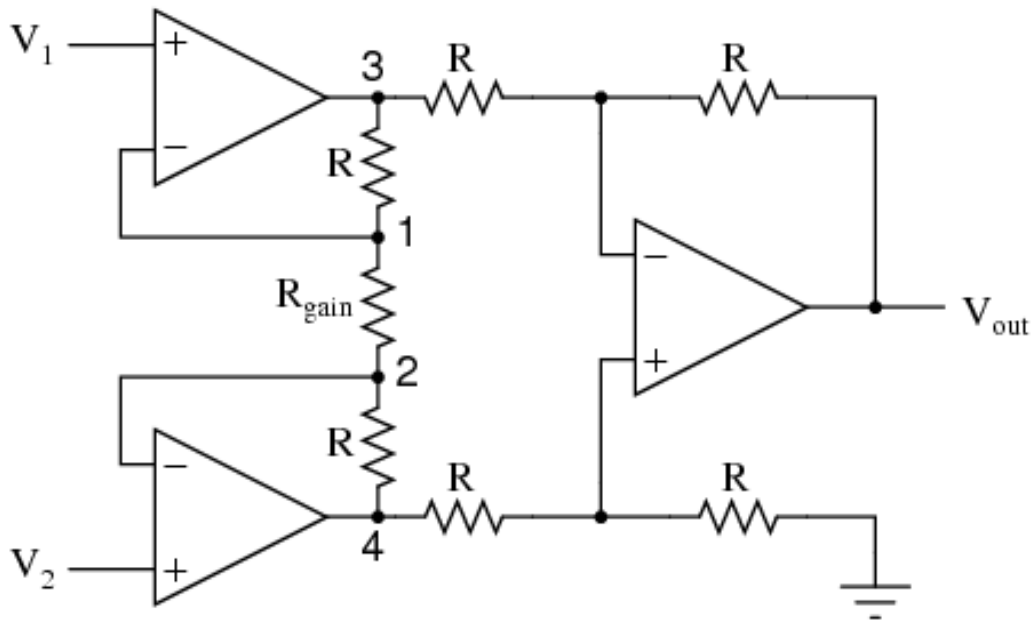
Fig. B.1 Differential amplifier circuit used as a substitute voltage signal
generator for the magnet power supply.

Start procedure of VSM

Before starting measurements using the VSM turn on the water supply to the magnets

(located in the ceiling above VSM). Load or replace the sample to be measured in the VSM,

next turn on the main power to the controller and the magnet power supply. This is the orange

switch located in the middle of the console. After the switch is turned, and the two devices are

powered on, turn the key on the 4300 controller to the "normal" position. The interface between

the computer, 4300 controller and the magnet power supply is done through a small National

Instruments data acquisition board (DAQ board). Make sure this DAQ board is connected to the

computer's USB port. Before turning on the power to the magnet power supply a "zero field"

voltage needs to be sent so that the magnets do not go to saturation when power is supplied to the

magnets; to accomplish this, run the "zero voltage.vi" when turning on the magnet power supply this should prevent the magnets from saturating when you turn on the power to the amplifier circuit. Once the initial setup has been completed the main controller program can be started. Run the "LakeShore 4300 VSM Controller (v1.5).vi" Located on the desktop of the computer.

The main program has the ability to monitor the centering of the sample, measure a single hysteresis loop (1 temperature) or multiple loops (range of temperatures). The outline for these three options is outlined here.

Centering the Sample (VSM)

The VSM controller program contains an algorithm for monitoring the position of the sample relative to the magnets (Figure). Unfortunately this is not done automatically like it is done in the SQUID magnetometer, on account that this particular model of VSM does not have motor controlled axis controls. Therefore the centering of all samples has to be done manually.
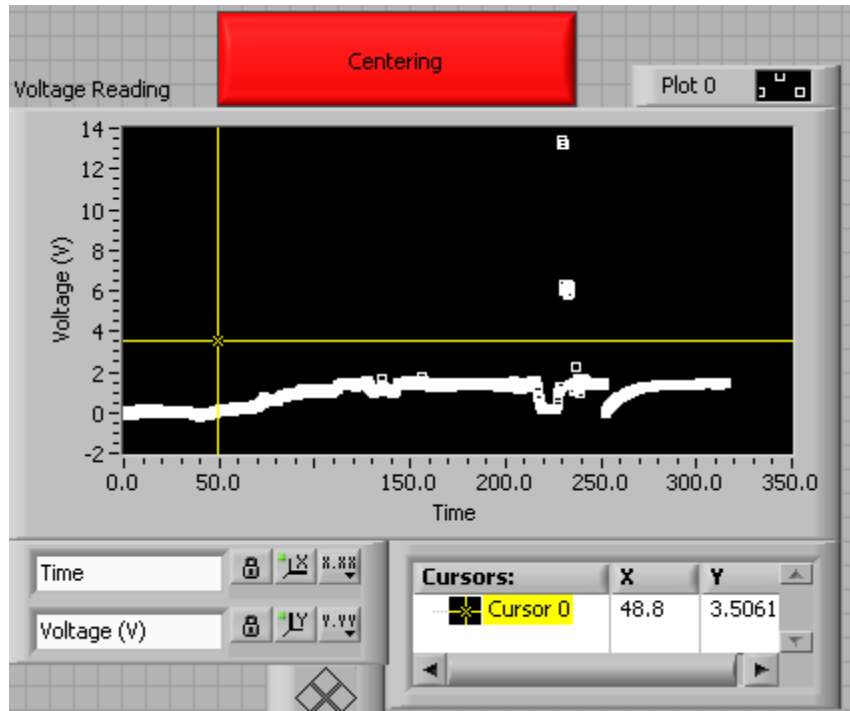
Fig. B.2 Sample centering monitor for the VSM program. The strongest voltage signal indicates that the sample is centered.

The centering window gives an updated real time view of the emu monitor of the VSM controller. By adjusting the axis knobs on the VSM one can monitor how the strength of the signal changes. Finding the maximum (or minimum depending on material type) indicates that the sample is centered after this the hysteresis curves M(H) can be measured.

Hysteresis Loop(s)

The main purpose of the Labview program is to ultimately measure the M(H) curves

required for the purpose of doing the analysis of G(T), S(T) and C_H(T). Running the program by

selecting "single hysteresis" (1 loop) or "multiple hysteresis" (many loops), gives the user the

option to collect information about the field dependent properties of the sample. The VSM is in

general not as accurate as the SQUID and therefore the user may experience problems associated

with noise for samples with moments below 10^{-3}emu. Furthermore the cryostat connected to the

VSM is not designed for temperatures below 77K (liquid Nitrogen) this also needs to be

considered when deciding on what type of sample to be analyzed. The VSM is therefore best

suited for samples with high moments at temperatures above 77K. Once the startup procedure is

complete; from the main program select the single or multi loop option.
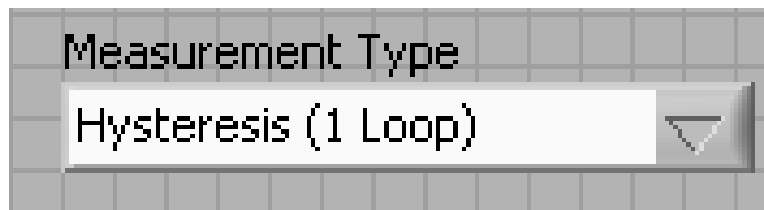
Fig. B.3 Selection control of the measurement type centering, Hysteresis (1 Loop) and Hysteresis (multi loop).

With either option chosen the maximum field value (H_{max} to $-H_{max}$) can be set as well as the

desired field step size (Fig. B.4). The accuracy in the voltage of the DAQ board limits the

precision of the field step size. From experiment, a 10 Oe step is the smallest most stable step

size that is controllable by the program (Figure).

Fig. B.4 Controls for setting the field strength and field step size.
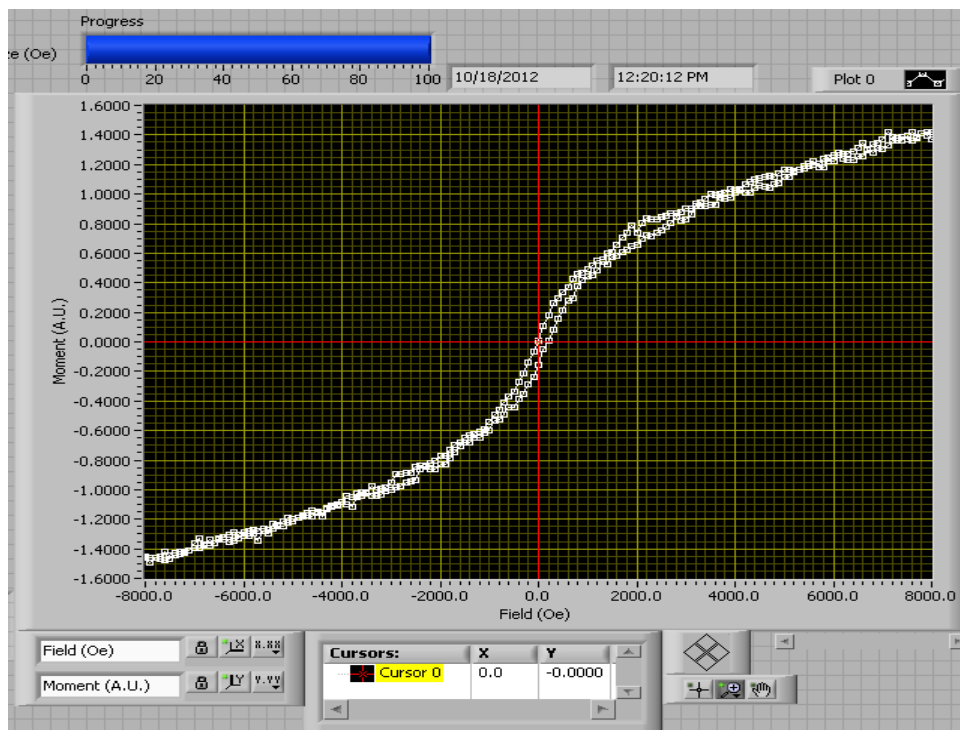
Fig. B.5 Main window for the VSM program which shows the M(H) behavior for the measured
sample updated in real time.

The temperature of the system is monitored by the program and maintained by way of the LakeShore 340 temperature controller; for a single loop the temperature can be set and maintained at a desired value (Figure). In the multiloop setup, a beginning and ending temperature value must be chosen along with the temperature step size.
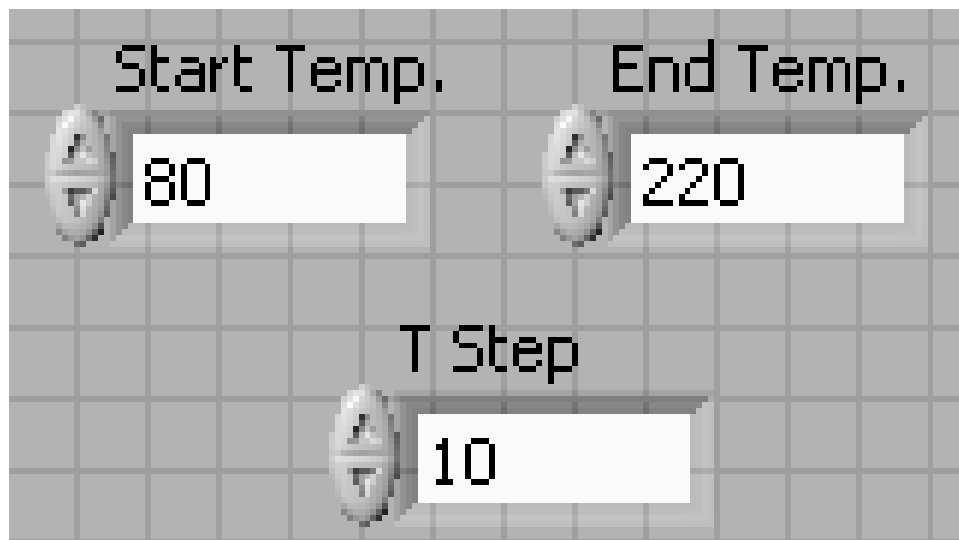
Fig. B.6 Controls for setting the starting and ending temperatures as well as the temperature step size.

The temperature controller has its own routine for stabilizing the set temperature. Some parameters need to be set on the temperature controller to ensure efficient and quick stabilization of the set temperature. The process for this is outlined in the manual for the 340 temperature controller.

APPENDIX C

DIFFERENTIAL EQUATION SOLUTIONS FOR HYSTERETIC BEHAVIOR

Theory of Ferromagnetic Hysteresis

Another potential application, and largely preferable method, of the calculation of these thermodynamic relationships is a theoretical model. A theoretical model that is in very good agreement with the experimental curves would partially eliminate the need for doing expensive tests when one could simply run a simulation first. In the "Theory of Ferromagnetic Hysteresis" Jiles and Atherton [] propose a method for determining the behavior of a ferromagnetic system. As in the cases of the modified Brilluoin function and the Langevin function neither of these functions reproduce the experimental data sets particularly well (low T regions) this is therefore one of the primary reasons for difficulty when it comes to obtain a hysteresis function for experimental data. The modified functions have no real physical basis for the "parameters" used in the function i.e. there is an arbitrary inclusion of these parameters in order for the function to better represent the data. Some other previous attempts to obtain a hysteresis function end up consisting of an extremely complicated mathematical function with almost random levels of accuracy. Lastly some simple functions, obtained from first principles with good theoretical foundations, can be used but usually fail to characterize real materials with sufficient accuracy. Other common approaches to curve fitting are done by the use of power series functions. Regardless in either of these methods the end result has to accomplish two goals:

1.) It must reproduce the experimental results

2.) There needs to be a solid fundamental basis for the function(s) used in the evaluation.

The method used here involves the solution to a differential equation that takes into account the energy supplied to the material, the loss due to hysteresis and the change in magnetostatic energy. The sum of the hysteresis loss and the change in magnetostatic energy must account for the total energy (from the magnetic field) supplied to the material [53].

$$\left(\begin{matrix} Energy\ supplied\ to \\ material \end{matrix} \right) = \left(\begin{matrix} Change\ in \\ magnetostatic \\ energy \end{matrix} \right) + \left(\begin{matrix} Hysteresis \\ loss \end{matrix} \right)$$

This results in a differential equation of the form presented below, which states that the rate of change of magnetization with respect to the external field H is proportional to the displacement of the magnetization from the anhysteretic (no hysteresis) magnetization curve. This means that the form of the solution for the hysteretic curve is related to how large the solution of the differential equation M deviates from the anhysteretic (no hysteresis) curve.

$$M_{an}(H) = M(H) + k \left(\frac{dM}{dH} \right)$$

$$\frac{dM}{dH} = \frac{M_{an}(H) - M(H)}{k}$$

Numerical solutions for Differential Equations

As will become readily apparent that the solutions to the equations needed to model various magnetic behavior are by no means trivial and therefore numerical solutions are derived using a computer program. Several numerical equation solver routines were written in Mathematica specifically to find the solutions to these equations. The goal ultimately would be

to find the precise combinations of a, α, c, and k to accurately reproduce the experimental curves for our experimental results, example lines of code are presented here as well as some of the graphical solutions to their respective differential equation.

In order to solve the equation for M(H) in the Anhysteretic solution a choice for the function that will represent the Anhysteretic magnetization curve will be required. Previous observations have concluded that a modified Langevin function, much like the one used in the curve fitting of the previous samples, leads to an expression of the Anhysteretic curve.

$$M_{an}(H_e) = M_s \left(Coth\left(\frac{H_e}{a}\right) - \left(\frac{a}{H_e}\right) \right)$$

$$H_e = H + \alpha M$$

Solving the above differential equation gives the form of the Anhysteretic curve as a function of applied field (Figs. C.1 & C.2).

```
AnHysteresis1[α_, a_, H_, step_] :=
  Module[{i, l = {}, m, Ms = 1.6 × 10⁶},
    For[i = -1, i < (2 H)/step, i++; m = M /. Quiet[FindRoot[M - Ms (Coth[((H - i step) + α M)/a] - a/((H - i step) + α M)) ⩵ 0, {M, 1000}]];
    l = AppendTo[l, {H - i step, m / Ms}]];
    l
  ]
```
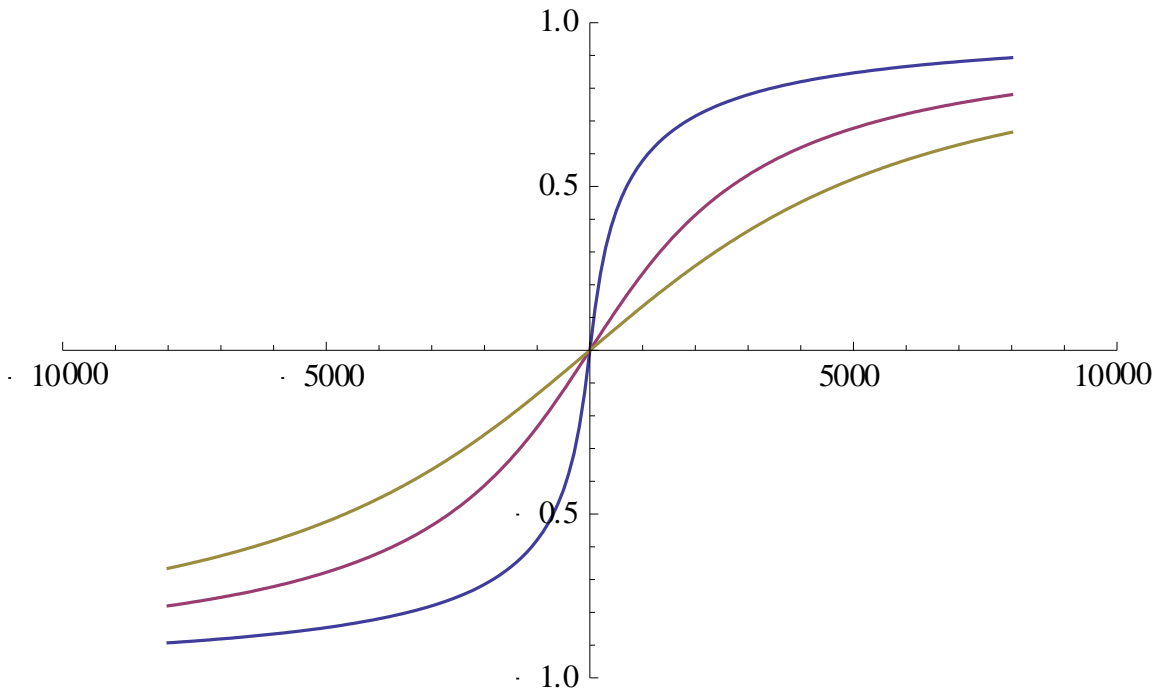

Fig. C.1 Sample code used to solve the differential equation for the Anhysteretic solution of the magnetization for various values of k.
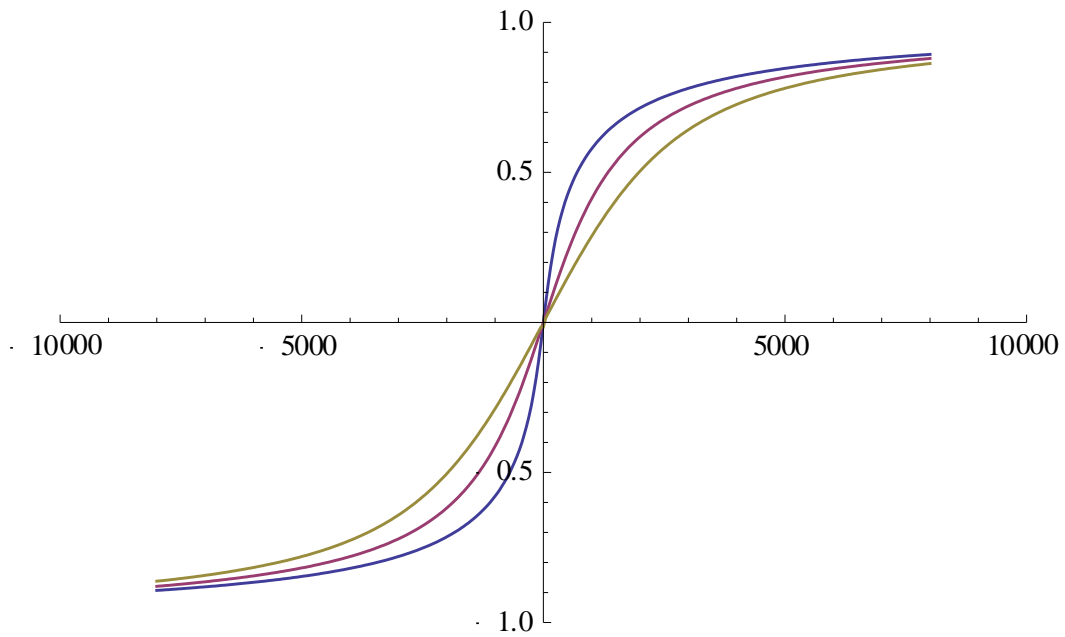
Fig. C.2 Solutions of the differential equation for determining the Anhysteretic solution of the magnetization for various values of the parameter α

The parameter α is related to the demagnetizing factor found in similar studies in which similar functions are used as a valid comparison. If α is made sufficiently large enough the solution to the differential equation produces two solutions in some regions of the graph and produces a sigmoid shaped curve like that of the known hysteretic behavior (Fig. C.3)

```
AnHysteresis2[α_, a_, H_, step_] :=
  Module[{i, Au = {}, Al = {}, mu, ml, Ms = 1.6 × 10⁶, l},

    For[i = -1, i < (2 H)/step, i++;

      l = Quiet[Length[Solve[M - Ms (Coth[((H - i step) + α M)/a] - a/((H - i step) + α M)) == 0, M, Reals]]];

      mu = M /. Quiet[Solve[M - Ms (Coth[((H - i step) + α M)/a] - a/((H - i step) + α M)) == 0, M, Reals]][[l]];

      ml = M /. Quiet[Solve[M - Ms (Coth[((H - i step) + α M)/a] - a/((H - i step) + α M)) == 0, M, Reals]][[l]];

      Au = AppendTo[Au, {H - i step, mu / Ms}];
      Al = AppendTo[Al, {H - i step, ml / Ms}];
    ];
    {Au, Al}
  ]
```
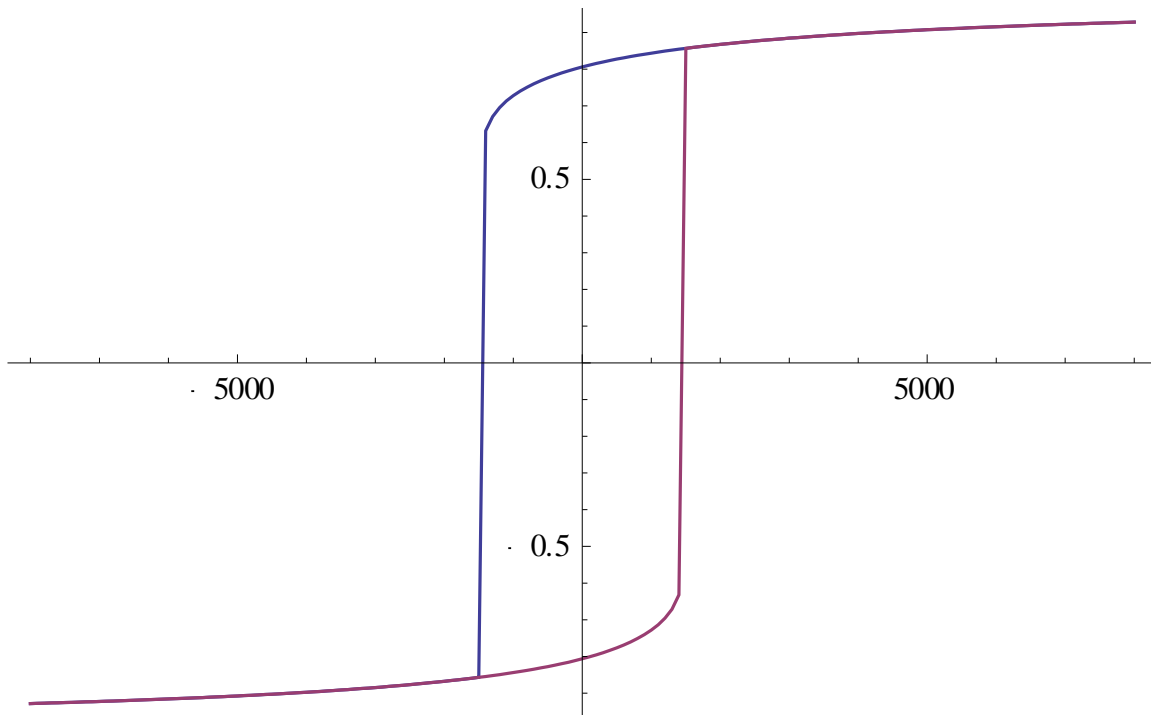

Fig. C.3 Sample code and the output of the solution to the Hysteretic nature of the magnetization.

Although this solution reproduces a familiar curve it does accurately reproduce the proper features seen in most of the hysteresis curves seen in experiments. If other factors such as the pinning of domain walls, the reversible and the irreversible components of the magnetization are included in the analysis of the initial differential equation, a more general form can be derived to give a curve that is in much better agreement with the experimental results. Doing so leads to the following result(s) the method for which is outlined in [53].

$$\frac{dM_{irr}}{dH} = \frac{1}{\frac{\delta k}{\mu} - \alpha(M_{an} - M_{irr})}(M_{an} - M_{irr})$$

$$\frac{dM_{rev}}{dH} = c\left(\frac{dM_{an}}{dH} - \frac{dM}{dH}\right)$$

The sum of these two relationships gives the differential equation whose solution should reproduce a proper from of the hysteresis curves.

$$\frac{dM}{dH} = \frac{1}{1+c}\frac{(M_{an} - M)}{\frac{\delta k}{\mu} - \alpha(M_{an} - M)} + \frac{c}{1+c}\frac{dM_{an}}{dH}$$

Solutions to this equation for specific choices of the parameters can also be used to reproduce the initial magnetization curves (Fig. C.4).
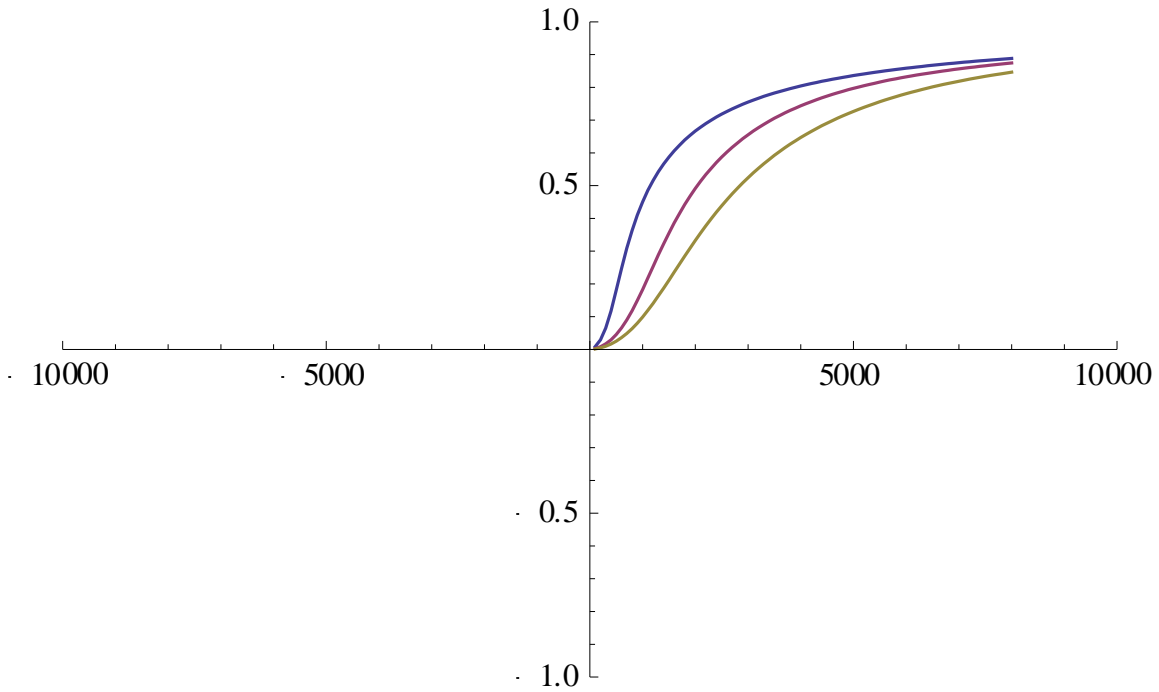
```
InitMag[α_, a_, k_, H_, c_, step_] :=
 Module[{i, l = {}, Ms = 1.6 * 10^6, μ = 1, m = 1.6 * 10^6},

  For[i = -1, i < Abs[(2 H)/step], i++;

   m = M /. Quiet[FindRoot[1/(1+c) ((Ms (Coth[((H - i*step) + α*M)/a] - a/((H - i*step) + α*M)) - M)/

       ((-k)/μ - α*(Ms (Coth[((H - i*step) + α*M)/a] - a/((H - i*step) + α*M)) - M)))*step +

     m + c/(1+c) (Ms (Coth[((H - (i+1)*step) + α*M)/a] - a/((H - (i+1)*step) + α*M)) -

       Ms (Coth[((H - i*step) + α*M)/a] - a/((H - i*step) + α*M))) == M, {M, Ms}];

   l = AppendTo[l, {(H - i*step), m/Ms}]];
  l
 ]
```

Fig. C.4 Sample code and plots of the solution for the initial magnetization curve for various values of α

124

APPENDIX D

MAGNETIC SUSCEPTIBILITY MEASUREMENTS

The magnetic susceptibility in Paramagnetic or Diamagnetic materials is determined simply from the linear relationship

$$M = \chi_m H$$

$$\chi_m = \frac{M}{H}$$

In the case of Ferromagnetic materials the magnetic moment (magnetization M) is not independent of the applied field H and therefore the relationship becomes.

$$\chi_m = \left(\frac{dM}{dH}\right)_{H=H_0}$$

Applying this relationship to a series of field hysteresis curves M(H) leads to the following dataset for the susceptibility of some of the Ferromagnetic materials used in previous measurements (Figs D.1 – D.3).

Magnetic Susceptibility Gd$_{200}$
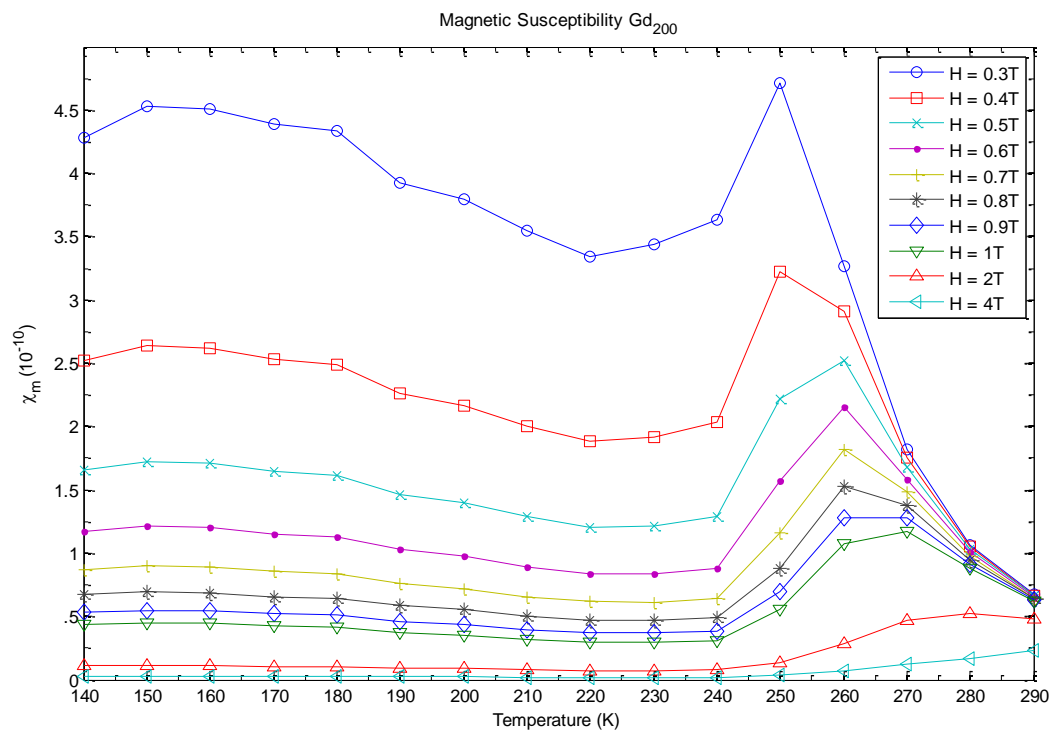
D.1 Magnetic Susceptibility at various external field strengths Gd$_{200}$
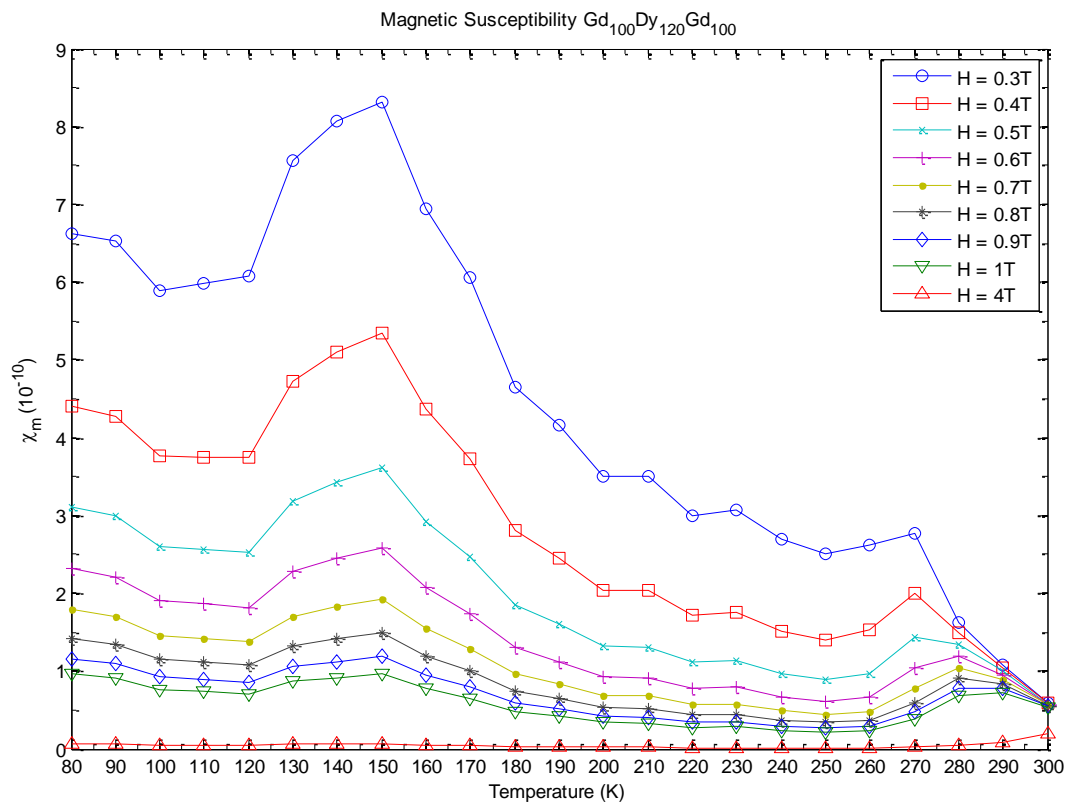
D.2 Magnetic Susceptibility at various external field strengths $Gd_{100}Dy_{120}Gd_{100}$
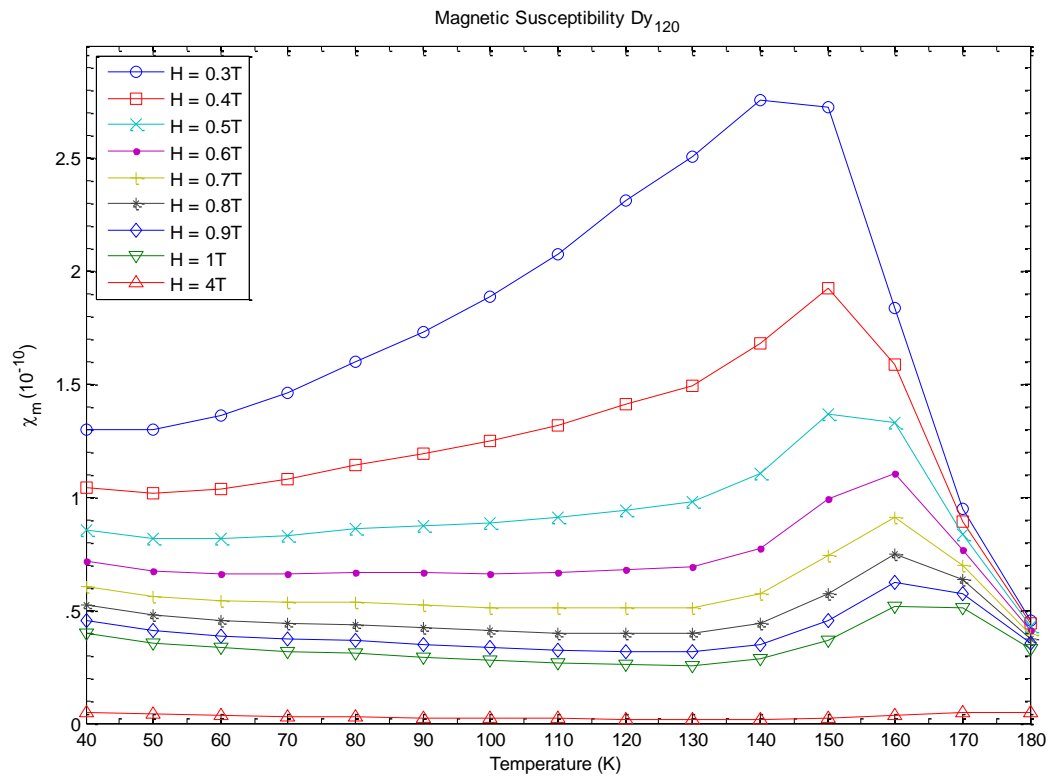
D.3 Magnetic Susceptibility at various external field strengths Dy_{120}

REFERENCES

1. S. Demirtas, M. R. Hossu, R. E. Camley, H. C. Mireles, and A. R. Koymen., Phys. Rev. B 72, 184433 (2005)

2. M. R. Hossu, Y. Hao, and A. R. Koymen, J. Phys. Condens. Mater. 20, 215224 (2008)

3. S. Demirtas, R. E. Camley, and A. R. Koymen, Appl. Phys. Lett. 87, 202111 (2005)

4. M. R. Hossu, A. R. Koymen, Appl. Phys. Lett. 99 08C704 (2006)

5. R.E. Camley, W. Lohstroh, G.P. Felcher, N. Hosoito, and H. Hashizume, J. Magn. Magn. Mater. 286, 65 (2005)

6. A. L. Dantas, A. T. Silva, G. G. Rebouças, A. S. Carriço and R. E. Camley, J. Appl. Phys. 102, 123907 (2007)

7. S. Kobayashi, Phys. Rev. Lett. 106, 057207 (2011)

8. H. Ott, C. Schüßler-Langeheine, E. Schierle, E. Weschke, and G. Kaindl.: Phys. Rev. B 82, 214408 (2010)

9. A. L Dantas, R.E. Camley, and A.S. Carrico, IEEE Trans. Magn. 42, 2942 (2006)

10. W. C. Koehler, J. Appl. Phys. 36, 1078 (1965)

11. P. H. Bly, W. D. Corner, and K. N. R. Taylor, J. Appl. Phys. 40, 4787 (1969)

12. J. J. Rhyne, R. W. Erwin, J. Borchers, S. Sinha, M. B. Salamon, R. Du and C. P. Flynn, J. Appl. Phys. 61, 4043 (1987)

13. J. Borchers, S. Sinha, M. B. Salamon, R. Du, C. P. Flynn, J. J. Rhyne and R. W. Erwin, J. Appl. Phys. 61 4049 (1987)

14. V. D. Mello, Ana L. Dantas, A. S. Carriço, Sol. Stat. Comm. 140, 447 (2006)

15. R. E. Camley, J. Magn. Magn. Mater., 200, 583 (1999)

16. A. S. Chernysho, A. O. Tsokol, A. M. Tishin, K. A. Gschneider, Jr., V. D. Pecharsky, Phys. Rev. B, 71, 184410 (2005)

17. R. E. Camley, R. L. Stamps, J. Phys.: Condens. Mat., 5, 3727 (1993)

18. F. Tsui, C. P. Flynn, Phys. Rev. Let., 71, 1462 (1993)

19. P. H. Bly, J. Appl. Phys., 40, 4787 (1969)

20. R. E. Camley, W. Lohstroh, G. P. Felcher, N. Hosoito, H. Hashizume, J. Magn. Magn. Mater., 286, 65 (2005)

21. M. Colarieti-Tosti, S. I. Simak, R. Ahuja, L. Nordström, O. Eriksson, M. S. S. Brooks, 201, 272 (2004)

22. R. E. Camley, D. R. Tilley, Phys. Rev. B., 37, 3413 (1987)

23. E. Schreier, M. Ekström, O. Hartmann, R. Wäppling, G. M. Kalvius, F. J. Burghart, S. Henneberger, A. Marelius, A. Kratzer, Phys. B, 240, 289 (2000)

24. D. C. Jiles, D. L. Atherton, J. Magn. Magn. Mater., 61, 48 (1986)

25. S. Das, J. S. Amaral, V. S. Amaral, J. Appl. Phys., 107, 09A912-1 (2010)

26. J. A. Hofmann, A. Paskin, K. J. Tauer, R. J. Weiss, J. Phys. Chem. Sol., 1, 45 (1956)

27. L. D. Jennings, R. M. Stanton, F. H. Spedding, J. Chem. Phys., 27, 909 (1957)

28. G. Castellano, J. Magn. Magn. Mater. 260, 146 (2002)

29. E. R. Callen, Phys. Rev. 124, 1373 (1961)

30. K. Dumesnil, C. Dufour, M. Vergnat, G. Marchal, Ph. Mangin, M. Hennion, W. T. Lee, H. Kaiser, J. J. Rhyne, Phys. Rev. B, 49, 12274 (1994)

31. T. Egami, C. D. Graham Jr., J. Appl. Phys., 42, 1299 (1971)

32. K. N. Döbrich, A. Bostwick, J. L. McChensey, K. Rossnagel, E. Rotenberg, G. Kaindl, Phys. Rev. Lett., 104, 246401 (2010)

33. S. N. Kaul, S. Srinath, Phys. Rev. B, 62, 1114 (2000)

34. S. H. Liu, D. R. Behrendt, S. Legvold, R. H. Good Jr., Phys. Rev., 116, 1464 (1959)

35. S. Chaudhary, P. Garg, S. Rajput, S. S. Comm. 132, 293 (2004)

36. M. T. Alkhafaji, N. Ali, J. All. Comp. 250, 659 (1997)

37   D. R. Behrendt, S. Legvold, F. H. Spedding, Phys. Rev., 109, 1544 (1958)

38.   H. U. Åström, G. Benediktsson, J. Phys. F: Met. Phys., 18, 2113 (1988)

39.   J. R. Banister, S. Legvold, F. H. Spedding, Phys. Rev., 94, 1952 (1954)

40.   A. Macdonald, Am. J. Phys. 67, 613 (1999)

41.   J. F. Elliott, S. Legvold, F. H. Spedding, Phs. Rev., 94, 1143 (1954)

42.   K. Niira, Phys. Rev., 117, 129 (1959)

43.   W. D. Corner, B. K. Tanner, J. Phys. C: Sol. St. Phys., 9, 627 (1976)

44.   R. G. Jordan, E. W. Lee, Proc. Phys. Soc., 92, 1074 (1967)

45.   T. Morishita, Y. Togami, K. Tsushima, J. Phys. Soc. Jpn. 54, 37 (1985)

46.   C. D. Stanciu, A. V. Kimel, F. Hansteen, A. Kiriluk, A. Itoh, Th. Rasing, Phys. Rev. Let. 99, 217204 (2007)

47.   K. Cherifi, C. Dufour, Ph. Bauer, G. Marchal, Ph. Mangin, Phys. Rev. B, 44, 7733 (1991)

48.   J. P. Andres, L. Chico, J. Colino, J. M. Riveiro, Phys. Rev. B, 66, 094424 (2002)

49.   S. Demirtas, A. R. Koymen, H. Zeng, J. Phys.: Cond. Mater. 21, L213 (2004)

50.   O. S. Anilturk, A. R. Koymen, Phys. Rev. B 68, 024430 (2003)

51.   H. Nagura, K. Takanasi, S. Mitani, K. Saito, T. Shima, J. Magn. Magn. Mater. 240, 183 (2002)

52.   C. Kittel, Introduction to Solid State Physics (Wiley, New York, 1976)

53.   D. Jiles, Introduction to Magnetism and Magnetic Materials (Chapman and Hall, London, 1998)

54.   M. Mansuripur, The Physical Principles of Magneto-Optical Recording (Cambridge Univ. Press, New York, 1995)

55.   S. Blundell, Magnetism in Condensed Matter (Oxford Univ. Press, New York, 2001)

56.   J. Clarke, A. Braginski, The SQUID Handbook (Wiley, Weinheim, 2004)

57.   D. C. Mattis, The Theory of Magnetism Made Simple (World Scientific Publishing, Singapore, 2006)

58.　B. D. Cullity, Introduction to Magnetic Materials (Addison-Wesley, Philippines, 1972)

59.　M. P. Marder, Condensed Matter Physics (Wiley, New York, 2000)

60.　K. H. J. Buschow and F. R. De Boer, Physics of Magnetism and Magnetic Materials (Kluwer and Plenum, New York, 2003)

61.　J. Mahan, Physical Vapor Deposition of Thin Films (Wiley, New York, 2000)

62.　N. Spaldin, Magnetic Materials (Cambridge Univ. Press, New York, 2011)

63.　H. B. Callen, Thermodynamics and an Introduction to Thermostatistics (Wiley, New York, 1985)

64.　V. Basso, M. Küpferling, C. P. Sasso, L. Giudici, Rev. Sci. Inst., 79, 063907 (2008)

65.　C. W. Miller, D. V. Williams, N. S. Bingham, H. Srikanth, J. Appl. Phys., 107, 09A903 (2010)

66.　F. Hellman, E. N. Abarra, A. L. Shapiro, R. B. van Dover, Phys. Rev. B, 58, 5672 (1998)

67.　S. Yu Dan'kov, A. M. Tishin, V. K. Pecharsky, K. A. Gschneider Jr., Phys. Rev. B, 57, 3478 (1998)

68.　D. J. W. Geldart, P. Hargraves, N. M. Fujiki, R. A. Dunlap, Phys. Rev. Lett., 62, 2728 (1989)

69.　M. Farle, A. Berghaus, K. Barberschke, Phys. Rev. B, 39, 4838 (1989)

70.　G. André, A. Aspelmeier, B. Schulz, M. Farle, K. Barberschke, Surf. Sci., 326, 275 (1995)

71.　K. P. Belov, A. K. Zvezdin, A. M. Kadomtseva, R. Z. Levitin, Sov. Phys. Usp., 19, 574 (1976)

72.　C. D. Graham Jr., J. Appl. Phys., 36, 1135 (1965)

73.　O. Nakamura, K. Baba, H. Ishii, T. Takeda, J. Appl. Phys., 64, 3614 (1988)

74.　J. M. Valentine, C. L. Chien, J. Appl. Phys., 99, 08P902 (2006)

75.　A. VI. Andrianov, O. A. Savel'eva, E. Bauer, J. B. Staunton, Phys. Rev. B, 84, 132401 (2011)

76.　C. D. Graham Jr., J. Appl. Phys., 34, 1341 (1963)

77. S. Hémon, R. A. Cowley, R. C. C. Ward, M. R. Wells, L. Douysset, H. Ronnow, J. Phys.: Condens. Matter, 12, 5011 (2000)

78. E. Vescovo, C. Carbone, O. Rader, Phys. Rev. B, 48, 7731 (1993)

79. M. A. Omar, Elementary Solid State Physics (Addison-Wesley, New York, 1993)

80. A. H. Morrish, The Physical Principles of Magnetism (IEEE Press, New York, 2001)

81. H. E. Duckworth, Electricity and Magnetism (Holt, New York, 1960)

82. R. J. Highmore, J. E. Evetts, A. L. Greer, R. E. Somekh, Appl. Phys. Lett., 50, 566 (1987)

83. D. T. Nguyen, M. Evangelisti, A. Di Bona, M. Affronte, Jor. Phys: Conf. Ser., 187, 012034 (2009)

84. A. Shadowitz, The Electromagnetic Field (Dover, New York, 1975)

85. R. M. Bozorth, Ferromagnetism (IEEE, New York, 1978)

86. D. J. Griffiths, Introduction to Electrodynamics (Prentice Hall, New Jersey, 1999)

87. *Encyclopædia Britannica Online*, s. v. "hysteresis," accessed October 26, 2012

88. S. Foner, Rev. Sci. Instr., 30, 548 (1959)

89. V. Basso, M. Küpferling, C. P. Sasso, L. Giudici, Rev. Sci. Instr., 79, 063907 (2008)

90. C. W. Miller, D. V. Williams, N. S. Bingham, H. Srikanth, Jor. Appl. Phys., 107, 09A903 (2010)

91. D. C. Mattis, R. H. Swendsen, Statistical Mechanics Made Simple (World Scientific Publishing, Singapore, 2008)

BIOGRAPHICAL INFORMATION

Ajani L. Ross earned a Bachelor of Science in Physics at Wright State University in Dayton, Ohio in 2007

In the fall of 2007 he became a graduate student at the University of Texas at Arlington, where he received a Master of Science in Physics in December 2010.